THE GROWTH OF AN EXTENDED {100}-ORIENTED GRAIN-BOUNDARY FREE SILICON FILM ON INSULATORS BY CONTINUOUS WAVE LASER CRYSTALLIZATION

連続発振レーザー結晶化による絶縁体上の無粒界｛100｝配向シリコン薄膜の持続成長

MUHAMMAD ARIF BIN RAZALI

SEPTEMBER 2021

DIVISION OF MATERIALS SCIENCE
GRADUATE SCHOOL OF SCIENCE AND TECHNOLOGY
NARA INSTITUTE OF SCIENCE AND TECHNOLOGY

To my parents, wife and son

A Dissertation Submitted

to the Graduate School of Science and Technology

in Fulfilment of the Requirements for the Degree of

Doctor of Philosophy (Engineering)

Thesis Committee

Professor Yukiharu URAOKA	(Supervisor)
Professor Jun OHTA	(Co-supervisor)
Professor Hisao YANAGI	(Co-supervisor)
Associate Professor Mutsunori UENUMA	(Co-supervisor)
Dr. Nobuo SASAKI	(Co-supervisor)

Abstract

In display technology, the two main focus to seek for improvement lean towards the lighting elements and the switching elements. Today, lots of researches focus on improving the display devices by improving the performance of the thin film transistors TFTs to replace amorphous silicon (a-Si) as the switching material due to its drawbacks; which lead to introduction of new materials including organic materials. On another extent, the well-developed a-Si technologies such as its standardized deposition parameters and well-established equipment lead towards the seek for improvements on the existing material, namely the crystallization of a-Si into polycrystalline silicon (poly-Si). Many techniques have been developed for the crystallization process including the strip heating, furnace heating, rapid thermal annealing and laser annealing. Fast and high throughput process with low thermal budget from laser annealing which resulted in decent poly-Si film has made the process a preferred one.

In this experiment, a-Si crystallization by means of continuous wave laser lateral crystallization (CLC) was carried out by a single scan of continuous wave (CW) green laser (532 nm) with rectangular beam (460 μm × 35 μm) having a flat-top profile in the long axis and a Gaussian profile in the short axis. Lateral growth of silicon film is seen when the a-Si is covered by a single layer of SiO_2 as a capping layer (C/L). A resulting long silicon grain with the absence of grain boundary was grown in the process with the preferred (100) silicon plane dominating the main 3-directions namely normal direction (ND) parallel to the surface plane, scan direction (SD) which is the direction of the laser scan and transverse direction (TD). The trace of laser crystallized poly-Si were observed by electron back scatter electron (EBSD) analysis to study the crystal orientations and grain boundary (GB) formation by inverse pole figure (IPF) mapping and grain misorientation angle (GMA) mapping respectively.

As a preliminary study, the crystal growth at different CLC laser power was analyzed and the mechanism of GB formation was elucidated by using a line beam spot. With the rectangular beam CLC, the process leaves behind columnar structures on the surface due to the instability of the solid/liquid frontal interface with formation of protrusions following the Mullins-Sekerka interface instability. The columnar structure possesses an average peak-to-valley height of 7 nm with the peaks alternate every 2 μm to 5 μm depending on the CLC parameters when analyzed by the atomic force microscopy (AFM).

The well oriented growth of silicon in laser scan direction following the columnar structure was confirmed by TEM observation where crystal lattice structure analyzed on a cross-section plane parallel to the laser scan direction shows a characteristic (100) orientation. This was deduced by lattice spacings characteristics from fast Fourier transform (FFT) image as well as from the selected area electron diffraction (SAED) pattern analysis. The observed (100) SD plane from TEM and highly oriented (100) plane from EBSD confirmed that the growth direction of the columnar structure shows the <100> silicon growth direction. Consequently, an extended GB-free silicon domain was successfully grown with the same approach with the help of the columnar structure that ease the optimization process.

TFT characteristics fabricated on the grain boundary (GB) free silicon film were compared between TFTs with channel direction parallel and perpendicular to the silicon domain growth direction. Negligible difference between the TFT mobilities on parallel and perpendicular channel direction justified that the grown silicon film having a characteristic of single crystalline silicon. A modification in laser system to transform the laser beam into rectangular shape successfully altered the crystallization mechanism with better film properties all around. This allows the grown quasi-single crystal silicon to be normalized in the TFT panels fabrication for display devices.

Table of Contents

Abstract i

Table of Contents iii

CHAPTER 1: Introduction 1

1.1 Historical overview 1

1.2 TFT technologies and the potential of poly-Si 4

1.3 Poly-Si film preparation techniques 6

1.4 State-of-the-art laser crystallization..8

1.5 Purpose and outline of this thesis 13

1.6 References 16

CHAPTER 2: Growth Evolution of Silicon Film Crystallized by CW Green Laser 19

2.1 Laser crystallization conditions and sophisticated film characterization techniques ...19

2.1.1 Laser system and optical components set up 20

2.1.2 Sample preparation 21

2.1.3 Film characterization techniques 23

2.2 Effect of capping layer on laser crystallized Silicon film 27

2.2.1 Heat storing 27

2.2.2 Anti-reflection 28

2.2.3 Experimental results...29

2.3 Crystal quality of grown poly-Si by CLC 33

2.3.1 Raman spectroscopy 33

2.3.2 Scanning transmission electron microscopy (STEM) 37

2.4 Evolution of crystal growth with varying laser power 41

2.5 Summary 47

2.6 References 49

CHAPTER 3: Extension of {100}-Oriented Grain Boundary-Free Silicon Film by CLC 51

3.1 Effect of silicon interface energy on domain growth 51

3.2 Achieving stable temperature profile with laser beam tuning 54

3.3 Characterization of well-oriented silicon film 57

3.3.1 Stable growth of {100} oriented grains 57

3.3.2 Surface morphology 61

3.3.2 In-plane orientation 64

3.4 Extended growth of {100}-oriented GB free grains 69

3.4.1 Growth of 12 mm elongated grain 69

3.4.1 Formation of low angle GBs and twin boundaries 72

3.5 Summary 76

3.6 References 78

CHAPTER 4: TFT Characteristics Fabricated on GB-free Silicon Film 81

4.1 Grain boundary effects on TFT carriers 81

4.2 TFT fabrication process 84

4.3 Channel geometrical effect on TFT performance..89

4.3.1 TFTs on typical CLC poly-Si 89

4.3.2 TFTs on GB-free quasi-single crystal silicon film 93

4.4 Summary..96

4.5 References 97

CHAPTER 5: Conclusions and Future Plans 99

5.1 Conclusions 99

5.2 Challenges and future plans..101

5.3 References 102

Acknowledgements...104

List of Publications 106

CHAPTER 1: Introduction

1.1 Historical overview

Over the years, breakthrough in semiconductor technologies bring the miniaturized electronics into mass production, specifically the high density monocrystalline 5 nm integrated circuits (ICs) which predicted to break into the market as semiconductor giants entered volume production of the chips. The high demand and fast advancement in silicon semiconductor industry has been pushing the fabrication of dense ICs so as to make the Moore's law ever relevant. Other semiconductor materials also no exception in expanding over the range of electrical components. Taking the thin film transistors (TFTs) for example, the advancement has led to the introduction of numerous high-resolution short-staring-distance devices. Going back in time, the concept of TFTs was first proposed by Lilienfeld as early as 1930 even though its first debut as a fully working device was introduced in 1961 by P.K. Weimer in IRE Transactions on Electron Devices [1]. More than ten years later, the TFT was then introduced in active-matrix liquid crystal display (AMLCD) or active-matrix flat panel display (AMFPD) in general as switching element which was reported by Brody et. al in 1973 [2]. Various semiconductor materials were then investigated including CdSe, InSb, and Ge and some of

them are successfully demonstrated but the progress of industrial applications remained slow. In 1979, Spear and LeComber fabricated the first amorphous silicon (a-Si) TFTs taking advantage of the possibilities for doping the a-Si by glow discharge technique [3]. The hydrogenated amorphous silicon (a-Si:H) deposition technique developed by Spear had many superior features, including large area uniformity, stability and reproducibility of the process as well as good fine-scale fabrication conformity, all of which were compatible with the semiconductor fabrication process. In addition, low temperature (<300 °C) deposition of a-Si:H enable the use of low-cost glass substrates with low thermal durability. Since then, development activities on a-Si TFTs stimulated owing to their findings which then lead to mass production of large area a-Si TFT-LCDs where the majority of AMLCDs utilized the novel a-Si TFTs.

Nowadays, there is ever-growing demand for TFT-LCDs for FPDs in the production of various devices and appliances – such as mobile phones, digital cameras, camcorders, personal digital assistants (PDAs), game machines, PC monitors, TVs, automobile panels, health monitoring systems, office automation equipment, and military systems. The demands have pushed the ability of conventional a-Si to its limit as device circuitry and design lean towards much simpler system on glass (SOG) where the peripheral drivers are integrated onto the same panel as the LCD arrays. Superior poly-Si TFTs over a-Si TFTs made poly-Si TFTs as a good candidate as switching element for SOG circuitry as a replacement for the notable silicon-on-insulator (SOI) TFTs which also referred as monocrystalline silicon (c-Si) TFTs. While it is possible to transfer the fabricated c-Si TFT drivers onto the glass substrate for SOG, the production cost is high and panel size is limited by the silicon wafer size [4]. Subsequently, the development in poly-Si TFT technology has broaden the use into non-LCD applications where the transistors are used to enhance specific functions or to stabilize the operation of the peripheral circuits. Figure 1.1 shows a schematic diagram of a TFT-LCD panel integrated with

controller, power supply and driver circuits. It will be feasible to integrate the complete system on glass if the performance of poly-Si TFTs is further improved and approaches that of SOI TFTs even fabricated at low temperature (< 350 °C). High performing poly-Si TFTs are even expected to be applied in three-dimensional (3D) integrated circuits (ICs) alongside with other high functional circuits such as dynamic random-access memory (DRAM), electrically erasable programmable read only memory (EEPROMS), TFT contact imagers and fingerprint sensors [5].

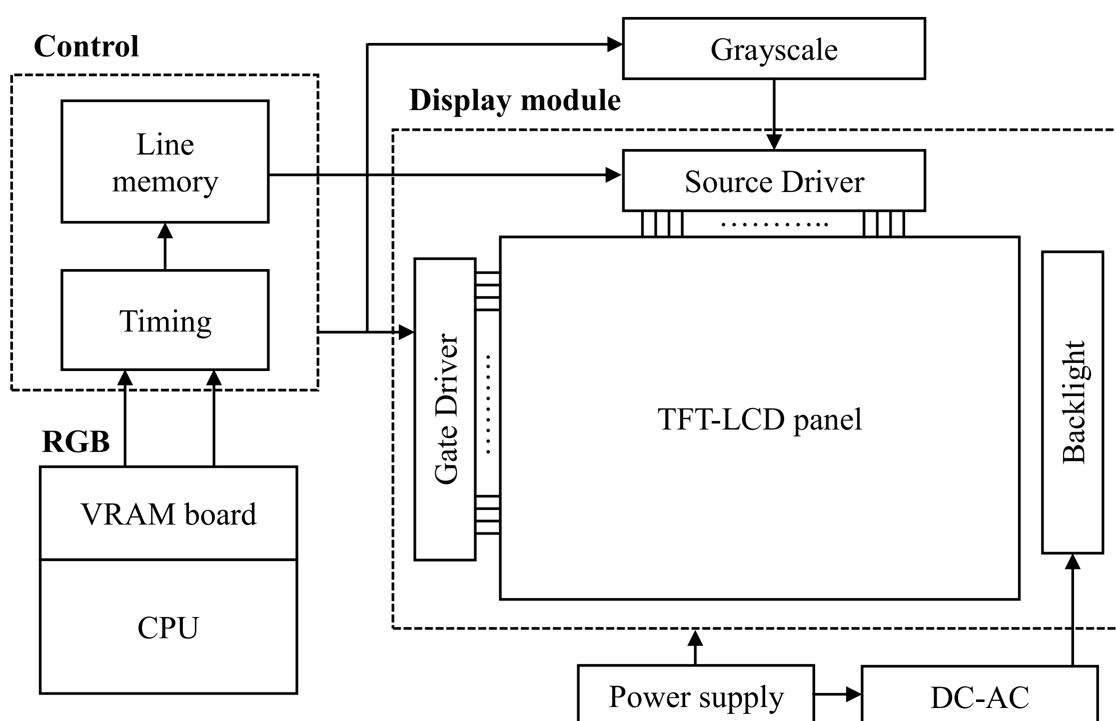

Figure 1.1: Schematic diagram of poly-Si TFT display module.

1.2 TFT technologies and the potential of poly-Si

Owing to the unique fabrication characteristics that allow a-Si TFTs to be fabricated on large-area substrate at low process temperature, a-Si TFTs has been the stem for the success in the display technology. The use of a-Si TFTs has been the standard for the mass production of AMLCDs for decades. However, even though the production line is well established and cost are relatively low, a-Si TFTs has some major drawbacks – with its low carrier mobility (<1.0 cm^2/Vs) i.e., the speed at which carriers can move through the transistor, being the most critical issue of a-Si TFTs. Whilst the value is sort of sufficient for switching the pixel elements, it is too small to operate fine-patterned pixel TFTs let alone other peripheral circuits such as the drivers for the display backplane itself. Poly-Si on the other hand offers markedly higher carrier mobility (10 ~ 900 cm^2/Vs for electron mobility) and high stability which leads to several improvements: (1) Higher pixel driving capability with larger on-current; (2) Scale down device dimension which leads to higher aperture ratio, increase brightness and reduce power consumption of display panel; and (3) Capable for monolithic integration of complementary metal-oxide semiconductor (CMOS) and other circuit elements on the FPDs [6,7].

Incorporating the use of poly-Si TFT rather a-Si TFT technology facilitates meeting the standards for high quality displays. It is worth mentioning that there are enormous researches that were and are currently undergoing that focus on improving the performance of AMFPDs, especially the TFT backplanes display. This includes the use of different types of materials for the channel region of the TFTs. However, taking into account of the standardized and establishment of the a-Si film preparation for previous TFT technology, the poly-Si film preparation by crystallization from a-Si film precursor only need one additional step which recompense in much better performance of the end products. Table 1.1 shows the performance of TFT materials used for TFT backplane and its applications.

Table 1.1: Performance of materials used for TFT backplanes and its applications.

Category	Inorganic (Si group)			Inorganic (Compound)	Organic
Material of TFT	a-Si TFT	poly-Si TFT	c-Si TFT (SOI)	Oxide TFT	Organic TFT
Channel Type	n	n, p	n, p	n	p (n)
Mobility (cm^2/Vs)	< 1.0	100 ~ 900	> 900	1 ~ 20	1.0 ~ 5
Micro-fabrication	×	○	◎	△	×
Uniformity	○	△	◎	○	×
Process	CVD	Laser Crystallization	Smart cut transfer	Sputtering and Solution	Vacuum Evaporation and Solution
Process Temp. (°C)	~ 350	~ 600	600 ~ 1000	150 ~ 400	~ 100
Stability	○	◎	◎	△	×
Cost	○	△	×	○	△
LCD Application	○	○	○	○	△
OLED Application	×	△	○	△	×
LSI / RF driving	×	△	◎	×	×

◎: Excellent, ○: Good, △: Moderate, ×: Poor.

High-performing poly-Si TFTs close to that of c-Si made it the best candidate in realizing the SOG for numerous information devices. Its high stability against environment and working loads will reflected to the longevity of the end products. This reliability rooted the researcher in poly-Si technology while finding ways to overcome the drawbacks affiliated with the poly-Si devices, which is its device-to-device performance uniformity. The uniformity issue in poly-Si technology arose in the large area displays especially in the uncontrolled nucleation regions in the poly-Si film together with the random generation of grain boundaries (GBs) as well as random crystal orientations [8]. Therefore, many techniques have been proposed and extensively studied to control the growth of the poly-Si in order to overcome this crucial issue which hold back the utilization of poly-Si from widely emerge and applied in display devices.

1.3 Poly-Si film preparation techniques

In general, there are two fundamental ways in preparing poly-Si film for TFT fabrication, namely; (1) Direct deposition process in which the silicon film is deposited directly in polycrystalline state, also referred to as-deposited poly-Si; and (2) Crystallization into poly-Si involving phase transformation, usually from amorphous state into polycrystalline state. For the as-deposited case, the film is epitaxially gown by means of vapor-phase growth method by chemical vapor deposition (CVD) or molecular beam deposition (MBD). The deposited film however suffers inferior film quality in term of grain size and defect density of the microstructure. The manifestation of this is the increased surface roughness of as-deposited films which leads to surface scattering at the insulator/poly-Si interface. Additionally, high process temperature (> 1000 °C) of CVD makes it not practical for large-area mass production especially for low thermal budget substrates.

The abovementioned crystallization process from a-Si, on the other hand may be induced by external energy (thermal or phonon excitation) source applied onto the film to

accomplish the phase transformation. The deposited a-Si film either regrown by; (1) Solid phase crystallization where rearrangement of silicon atoms occurs upon heating for a long period of time; or (2) Liquid phase crystallization where the film is melted and cooled at a certain rate. In the solid phase crystallization (SPC) process, the heating usually takes place in a furnace and heated at low to moderate temperature (~ 600 °C) for a long period of time [9]. Thermal durability of the substrate needs to be taken into account in this process as there are compromise between the annealing temperature and annealing time with film quality, especially the grain size of the poly-Si. Alternatively, the annealing time and the thermal budget can be effectively reduced to obtain higher throughput by means of rapid thermal annealing (RTA) instead of SPC but the poly-Si grain size is much smaller than that of SPC. The use of composite films such as SiGe or integration of metal catalyst film, also referred as metal induced crystallization (MIC) in SPC are some modifications made to improve the throughput of the process [10]. These catalyst films provide nucleation seeds as well as allowing the a-Si film to crystallize at lower annealing temperature. These modifications in SPC successfully increased the grain size but the film is contaminated by external impurities during the process [11]. Figure 1.2 shows the roadmap of the various poly-Si film preparation techniques in the poly-Si technology.

Liquid phase crystallization by melting and followed by cooling of a-Si or poly-Si successfully regrown the silicon film with a large grain size superior to that of SPC. A graphite strip heater as a source of thermal energy usually used and scanned on top of the sample to initiate the melting, and the subsequent cooling process of the film can be controlled by regulating the in-plane temperature gradient of the sample. Optimizing the cooling rate enables a single crystal silicon film to grow in this process [12]. However, the heating of the sample at high temperature restricted this high-quality silicon film to be grown only on thermally durable substrate (silicon wafers). On the other hand, low temperature crystallization which exhibits

rapid melting and freezing of the silicon film by phonon excitation has been the state-of-art in the TFT fabrication technology over the past few decades. The fast crystallization process with exceptionally large grain size poly-Si and low defects such as less dislocation density and minimum GB formation can be obtained even at lower process temperature (< 600 °C). Furthermore, short-time film melting by fast laser irradiation avert the damage on the substrate as the thermal strain on low temperature substrates is kept low. These advantages made the laser crystallization technique as a standard process for the fabrication of large-grain poly-Si films on transparent insulating substrates.

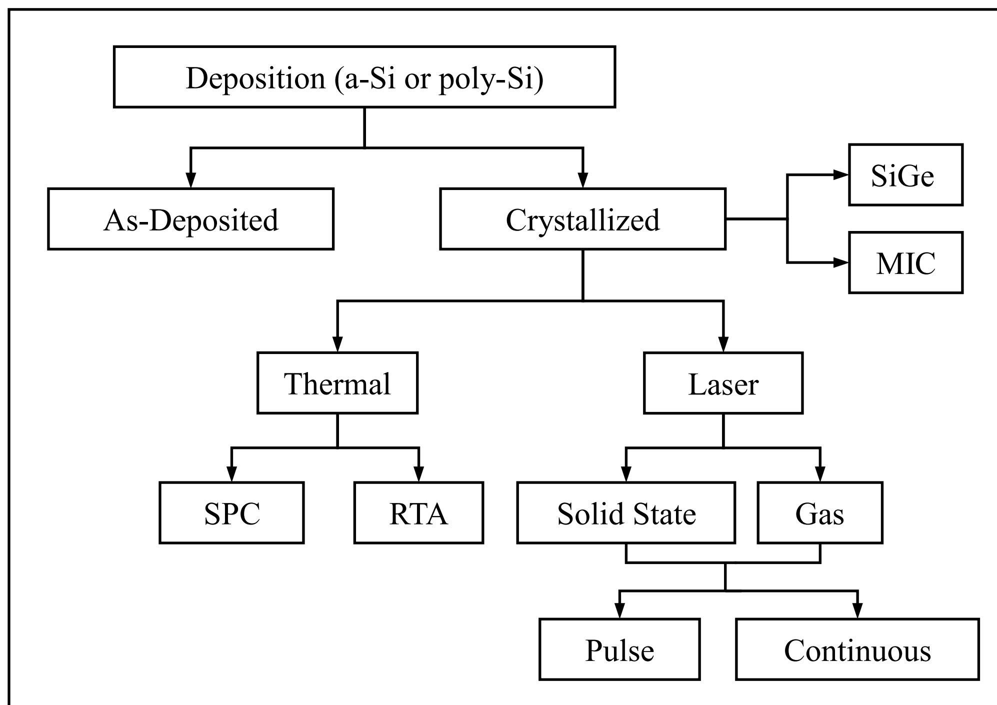

Figure 1.2: Roadmap of poly-Si preparation techniques.

1.4 State-of-the-art laser crystallization

In the early days, the use of laser irradiations in semiconductor industry was for the ion implantation purposes by means of plasma-producing multi energy ions which then accelerated to the target substrate where the pulse repetition rate and time of irradiation are tuned to control the dose of the generated ions [13]. Advancement in the laser technology has seen expansion

of its applications especially in semiconductor industry including the novel laser crystallization of a-Si precursor film into better performing poly-Si; while the cutting-edge laser-powered lithography being the most technologically advanced in the industry.

The use of excimer laser annealing (ELA) in the crystallization of a-Si precursor film into poly-Si has given the silicon-based TFTs a second life in mass production of high-resolution display panels as the low-performance a-Si TFTs are surpassed by new alternative compound-based materials especially amorphous oxides compounds [14,15]. Conventionally, the use of repeating short laser pulse (typically ~ 30 ns) of short wavelength xenon monochloride (XeCl) at 308 nm or krypton fluoride (KrF) at 248 nm in ELA allows the modification to be made on the a-Si film without imposing any damage to the underlying substrate. In this process, proper energy density exerted on the a-Si are necessary in order to let the film to grow in the preferred super lateral growth (SLG) regime as proposed by Im et al. [16]. In this regime, fractions of small unmelted islands are let to remain at the bed of the a-Si film to behave as a nucleation site during the cooling process; in contrast to full-melt regime where more random nucleation are prompted due to the absence of the seeds.

Nevertheless, the spherically grown poly-Si by SLG restricted the grain size to a limit of 500 nm which is not enough to boost the mobility of electrons due to the generation of potential barriers at GBs which scattered the carriers during operation and thus restrained the mobility to an average value of 150 cm^2/Vs. Additionally, the vertical growth of poly-Si in SLG instigated to the formation of protrusions or hillocks that led to the increase in surface roughness on the surface of the poly-Si film [17,18]. Such film properties and device performance were also seen with the crystallization using different types of lasers with pulse irradiation mode including solid-state lasers with the neodymium doped yttrium aluminum garnet (Nd:YAG) laser being the most common one[19].

On the other hand, two-directional growth of poly-Si in lateral manner allows the grain to elongate in the direction of the laser scan hence higher carrier mobility are expected with the exclusion of grain boundary in the current flow direction. To meet this purpose, modification or introduction of additional features on the laser system are necessary; for instance, crystallization with sequential lateral solidification (SLS), selectively enlarging laser crystallization (SELAX) and phase modulated ELA (PMELA) are some of the approaches demonstrated in ELA [20]. Other modifications related to the sample preparations are also implemented in order to crystallized the poly-Si in a more controlled manner; the grain size and crystal orientation being the highest concern in classifying the film quality. Such preparations include the formation of a top waveguide layer, formation of grain filters as in micro-Czochralski (μ-Cz) method and also a-Si film pre-patterning [21–27].

Alternatively, the use of continuous wave laser irradiation offers the same advantage of a stable lateral growth due to consistent energy irradiation over the surface as the laser beam sweep across the sample. The process, known as continuous wave laser lateral crystallization (CLC) produces poly-Si grains superior to the one obtained by pulse laser irradiation; commonly grew to more than hundreds of micrometers in length [28]. This allows the devices fabricated on such large grains to have uniform performance thus eliminate the uniformity issues which are often affiliated with granular grains obtained by ELA. However, this is not a straight forward process where many factors need to be optimized to achieve such compelling results; in fact, variety of results were obtained through different research thus no conclusive consent yet achieved. Furthermore, a long grain alone is not sufficient to tackle the uniformity issue of TFT due to the fact that different TFT channel direction will encounter different geometry of GBs; for instance, a TFT channel parallel to the long grains will impose less effect as compared to the one fabricated with channel direction pointing across the long grain as high possibility of GB scattering are expected in the latter case [6,29,30]. Many types of laser

systems with variety of modification are being introduced to grow the silicon domains to a largest possible size, ideally a single-crystalline-like silicon domain; this include the use of a simple neodymium doped orthovanadate ($ND:YVO_4$) laser (λ = 532 nm), a blue laser diode annealing (BLDA) system (λ = 445 nm), and multi-line beam (MLB) CLC system; with more concern was put on the shape of the beam spot for the CLC process [31,32].

Although long grains could be obtained by CLC, yet variation in the poly-Si domain size and its orientation are still observed. A trade-off between the grain size and crystal orientation were reported several times where the use of high number of laser shot (pulse) or multiple scan (CW) of laser helps in improving the orientation of the grown poly-Si with high percentage of grains were grown in the preferred {100} orientation; but enhancing the formation of GBs in the process [33]. Table 1.2 shows the summarized findings by N. Sasaki et al., Jpn. J. Appl. Phys. 58, SBBJ02 (2019) of some recent reports on laser crystallization of poly-Si concerning the orientation of the poly-Si [34]. Variation in crystallization parameters as well as the a-Si precursor film thickness do vary the orientation of the silicon domain in surface normal direction (ND) and in laser scan direction (SD). The use of single scan CW laser irradiation is proven to be good in controlling the orientation of the domains but the grain size is still a big concern.

Table 1.2: Summary of poly-Si orientation with various laser crystallization conditions. After N. Sasaki et al., Jpn. J. Appl. Phys. 58, SBBJ02 (2019).

	Shot or scan frequency	Ambient	Si thickness	Texture		Ref.
				ND	SD	
	Pulse Laser					
Granular grain	> 150 shots	N_2	40 nm	(100)	Random	[35]
	100-500 shots	Vac.	30 nm	(100)	-	[36]
	> 100 shots	Vac.	< 40 nm	(100)	Random	[37]
	> 100 shots	Vac.	> 40 nm	(111)	Random	[37]
	Continuous wave laser (CW)					
	10 times	Air	130 nm	(100)	Random	[38]
	Continuous wave laser lateral crystallization (CLC)					
Lateral grain	5-80 times	Air	60 nm	(100)	(100)	[33]
	6 times	Air	150 nm	(100)	-	[31]
	2-6 times	Air	150 nm	(100)	(100)	[32]
	1 time	Air	150 nm	(211)	(110)	[39]
	1 time	Air	60 nm	(100)	(100)	[33]
	1 tine	Air	60 nm	(100)	(100)	[40]
	1 time	Air	150 nm	(100)	(100)	[32]
	1 time	Air	60 nm	(100)	(100)	[41]

1.5 Purpose and outline of this thesis

The purpose of this thesis is to develop a technique in continuous wave laser lateral crystallization to crystallize the pre-deposited a-Si into an elongated silicon grain with preferred {100} orientation while eliminating the formation of grain boundary to achieve better device-to-device performance uniformity. Figure 1.4 shows the outline of this thesis.

The thesis contains three main parts beginning from chapter 2 which introduce the sophisticated electron backscatter diffraction (EBSD) technique in characterizing various film properties, mainly the grain structure and its orientation; supported by other conventional characterization techniques including the Raman spectroscopy, electron microscopy as well as atomic force microscopy. This chapter also shows the effect of utilizing a single capping layer in enhancing the lateral growth of the embedded a-Si layer upon laser irradiation; behaving as a heat reservoir and also acting as an anti-reflection film which resulting in a highly oriented poly-Si in the surface direction. Finally, this chapter discussed the evolution of the crystallization by varying the laser power; also analyzed by various characterization techniques.

In Chapter 3, a modification in the laser beam spot was introduced where a line beam with Gaussian profile both in the long and short axis was transformed into a rectangular beam with the long axis having a flat-top profile while Gaussian profile in the short axis was retained but expanded to a wider baseline. As a result, change in the silicon growth behavior was observed where wide and elongated single crystalline silicon domains were grown without the presence of grain boundary. The single crystalline properties were confirmed by analytical methods used for film characterization. A brief mechanism for the stable growth of extended {100}-oriented grain boundary free silicon domain also discussed in this chapter by taking the consideration of the instability on the solid/liquid frontal during the solidification which was introduced by W. W. Mullins and R. F. Sekerka.

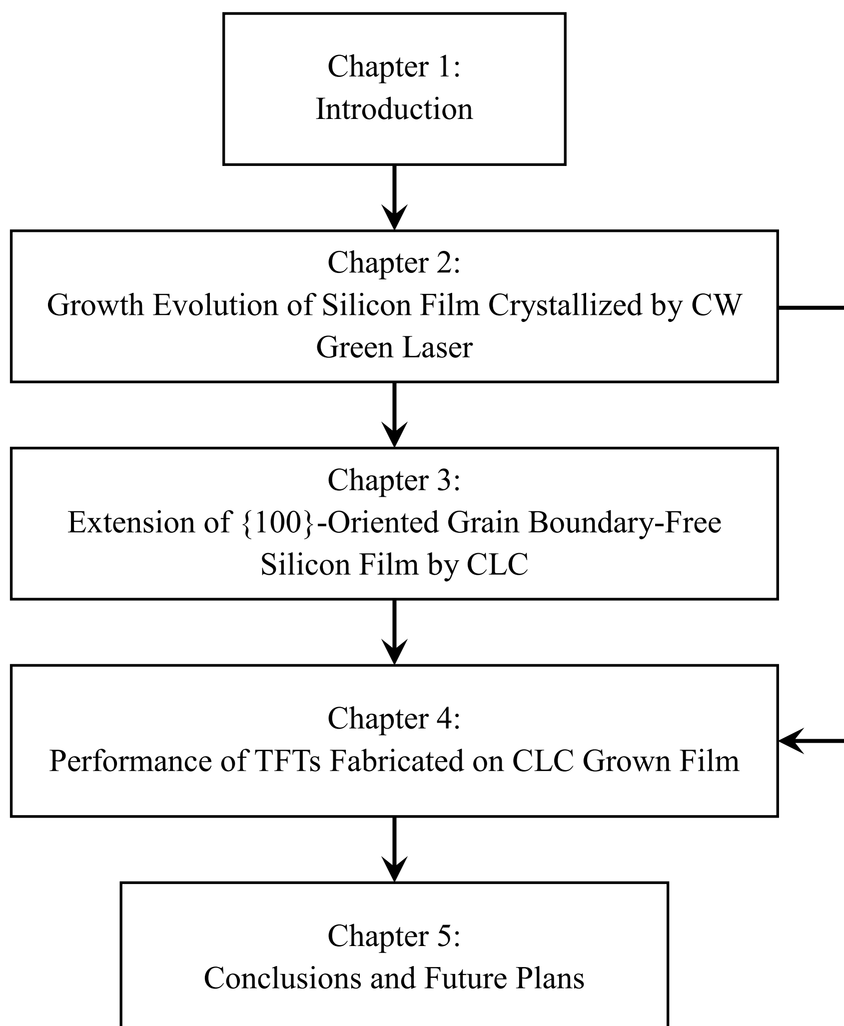

Figure 1.3: Outline of this thesis.

Finally, the properties of the silicon films crystallized by the Gaussian line beam (Chapter 2) and the modified flat-top rectangular beam (Chapter 3) were used for TFT fabrication. The electrical properties of the TFTs were analyzed and compared where grain boundaries effects on carrier mobility being the main focus. Additionally, grain boundary free region confirmation was validated by fabrication of TFTs having a channel parallel or perpendicular to the direction of the laser scan considering that the grain boundary often grows with the laser scan.

Chapter 5 summarizes all the results and findings discussed in the previous chapters and describes the overall conclusion of this work as well as further developments in the experiment to further utilize the maximum potential of the method as well as to analyze the crystallization mechanisms in whole.

1.6 References

1. P. K. Weimer, Proc. IRE **50**, 1462 (1962).

2. T. P. Brody, J. A. Asars, and G. D. Dixon, IEEE Trans. Electron Devices **20**, 995 (1973).

3. P. G. Le Comber, W. E. Spear, and A. Ghaith, Electron. Lett. **15**, 179 (1979).

4. H. S. Kim, R. H. Blick, D. M. Kim, and C. B. Eom, Appl. Phys. Lett. **85**, 2370 (2004).

5. W. Wondrak, R. Constapel, R. Traute, C. Bokeloh, and R. Herzer, IEEE Int. Symp. Power Semicond. Devices ICs 371 (1998).

6. M. Yamano, S. I. Kuroki, T. Sato, and K. Kotani, Jpn. J. Appl. Phys. **53**, 03CC02 (2014).

7. W. Yeh, M. Hirasue, K. Ohtoge, and T. Tsuchiya, Jpn. J. Appl. Phys. **59**, 071008 (2020).

8. S. Fujii, S. I. Kuroki, Y. Kawasaki, and K. Kotani, Jpn. J. Appl. Phys. **51**, 02BJ03 (2012).

9. R. Numata, K. Toko, N. Usami, and T. Suemasu, Thin Solid Films **557**, 147 (2014).

10. K. Toko, M. Nakata, A. Okada, M. Sasase, N. Usami, and T. Suemasu, Int. J. Photoenergy **2015**, 790242 (2015).

11. M. Wong, Z. Jin, G. A. Bhat, P. C. Wong, H. S. Kwok, and S. Member, IEEE Trans. Electron Devices **47**, 1061 (2000).

12. B. Y. Tsaur, J. C. C. Fan, M. W. Geis, D. J. Silversmith, and R. W. Mountain, Appl. Phys. Lett. **39**, 561 (1981).

13. F. Belloni, D. Doria, A. Lorusso, and V. Nassisi, EPAC 2006 - Contrib. to Proc. 2355 (2006).

14. K. Taira, Y. Hirose, S. Nakao, N. Yamada, T. Kogure, T. Shibata, T. Sasaki, and T. Hasegawa, ACS Nano **8**, 6145 (2014).

15. T. Kamiya, K. Nomura, and H. Hosono, Sci. Technol. Adv. Mater. **11**, 044305 (2010).

16. J. S. Im and H. J. Kim, Appl. Phys. Lett. **64**, 2303 (1994).

17. M. M. Billah, A. B. Siddik, J. Bae Kim, L. Zhao, S. Y. Choi, D. K. Yim, and J. Jang, IEEE J. Electron Devices Soc. **7**, 503 (2019).

18. S. P. Huang, H. C. Chen, P. H. Chen, Y. Z. Zheng, A. K. Chu, Y. S. Shih, Y. X. Wang, C. C. Wu, Y. A. Chen, P. J. Sun, H. C. Huang, W. C. Lai, and T. C. Chang, IEEE Trans. Electron Devices **67**, 3163 (2020).

19. A. G. Cullis, N. G. Chew, H. C. Webber, and D. J. Smith, J. Cryst. Growth **68**, 624 (1984).

20. C. L. Pan, K. W. Chen, Y. C. Wang, S. H. Kao, and P. Wu, AIP Adv. **10**, 055321 (2020).

21. S. I. Kuroki, X. Zhu, K. Kotani, and T. Ito, Jpn. J. Appl. Phys. **49**, 04DJ11 (2010).

22. Y.-D. Son, N.-K. Son, K.-H. Kim, E.-H. Kim, J.-H. Oh, and J. Jang, SID Symp. Dig. Tech. Pap. **38**, 76 (2007).

23. M. W. Geis, D. C. Flanders, and H. I. Smith, Appl. Phys. Lett. **35**, 71 (1979).

24. J. Zhang, M. Trifunovic, M. Van Der Zwan, H. Takagishi, R. Kawajiri, T. Shimoda, C. I. M. Beenakker, and R. Ishihara, Appl. Phys. Lett. **102**, 243502 (2013).

25. P. C. Van Der Wilt, B. D. Van Dijk, G. J. Bertens, R. Ishihara, and C. I. M. Beenakker, Appl. Phys. Lett. **79**, 1819 (2001).

26. A. Hara, F. Takeuchi, M. Takei, K. Suga, K. Yoshino, M. Chida, Y. Sano, and N. Sasaki, Japanese J. Appl. Physics, Part 2 Lett. **41**, L 790 (2002).

27. S. J. Park, Y. M. Ku, K. H. Kim, E. H. Kim, B. K. Choo, J. S. Choi, S. H. Kang, Y. J. Lim, and J. Jang, Thin Solid Films **511–512**, 243 (2006).

28. M. Arif, N. Sasaki, Y. Ishikawa, and Y. Uraoka, Thin Solid Films **708**, 138127 (2020).

29. T. T. Nguyen and S. I. Kuroki, Jpn. J. Appl. Phys. **58**, SBBJ08 (2019).

30. A. Hara, M. Takei, F. Takeuchi, K. Suga, K. Yoshino, M. Chida, T. Kakehi, Y. Ebiko, Y. Sano, and N. Sasaki, Japanese J. Appl. Physics, Part 1 Regul. Pap. Short Notes Rev. Pap. **43**, 1269 (2004).

31. T. T. Nguyen, M. Hiraiwa, and S. I. Kuroki, Appl. Phys. Express **10**, 056501 (2017).

32. T. T. Nguyen, M. Hiraiwa, T. Koganezawa, S. Yasuno, and S. I. Kuroki, Jpn. J. Appl.

Phys. **57**, 031302 (2018).

33. N. Sasaki, Y. Nieda, D. Hishitani, and Y. Uraoka, Dig. Tech. Pap. - SID Int. Symp. **47**, 1317 (2016).

34. N. Sasaki, M. Arif, and Y. Uraoka, Jpn. J. Appl. Phys. **58**, SBBJ02 (2019).

35. D. P. Gosain, A. Machida, T. Fujino, Y. Hitsuda, K. Nakano, and J. Sato, Japanese J. Appl. Physics, Part 2 Lett. **42**, L 135 (2003).

36. M. He, R. Ishihara, W. Metselaar, and K. Beenakker, J. Appl. Phys. **100**, 083103 (2006).

37. M. Weizman, C. Klimm, N. H. Nickel, and B. Rech, Appl. Phys. Lett. **100**, 161906 (2012).

38. J. S. Im, M. Chahal, P. C. Van Der Wilt, U. J. Chung, G. S. Ganot, A. M. Chitu, N. Kobayashi, K. Ohmori, and A. B. Limanov, J. Cryst. Growth **312**, 2775 (2010).

39. S.-I. Kuroki, Y. Kawasaki, S. Fujii, K. Kotani, and T. Ito, J. Electrochem. Soc. **158**, H924 (2011).

40. N. Sasaki, Y. Nieda, D. Hishitani, and Y. Uraoka, Thin Solid Films **631**, 112 (2017).

41. N. Sasaki, M. Arif, and Y. Uraoka, SID Symp. Dig. Tech. Pap. **49**, 755 (2018).

CHAPTER 2:

Growth Evolution of Silicon Film Crystallized by CW Green Laser

In this chapter, the basic method for laser crystallization was introduced to transform the dehydrogenated a-Si film into poly-Si by using continuous wave (CW) laser with a line beam. Various characterization methods for crystallographic analysis were used to extract as much information as possible on the poly-Si crystal growth with varying CLC laser power thus enabled the study on the mechanism of the growth evolution of the silicon film.

2.1 Laser crystallization conditions and sophisticated film characterization techniques

A simple table-top laser system was set up for the a-Si film crystallization. A diode-pumped solid state (DPSS) laser with CW output having a wavelength of 532 nm was used to crystallize unseeded a-Si film in air ambient while keeping the substrate at room temperature. A wide processing window were reported despite its simple process. The simple set up and small footprint of DPSS lasing system is advantageous in lowering the cost of fabrication and its maintenance. Above all, the liquid phase crystallization by CW laser is capable for growing the poly-Si in lateral manner parallel to the direction of the laser scan thus poly-Si with

elongated grains are expected by the CW crystallization. The crystallized films were then characterized by the sophisticated electron backscattered diffraction (EBSD), also termed as electron backscattered diffraction pattern (EBSP) to give an insight of the crystal orientation and grain boundary formation after the crystallization process. Other conventional methods also used for the film characterization such as Raman spectroscopy, electron microscopy and atomic force microscopy (AFM).

2.1.1 Laser system and optical components set up

Laser crystallization was done by a simple table top laser set up with green continuous wave irradiation at a wavelength of 532 nm produced by Verdi-V5 laser from Coherent Inc. as the energy source for crystallization. Neodymium-doped yttrium orthovanadate ($ND:YVO_4$) gain medium is diode-pumped and reflected in the resonator centered at 1064 nm wavelength as the nominal output wavelength. Birefringent crystal, lithium triborate (LBO, LiB_3O_5) that kept at 150 °C functions as second harmonic generator and frequency doubler effectively convert the fundamental 1064 nm output wavelength into half (λ = 532 nm). Relatively high deep penetration depth of green light exceeding micrometers range made it advantageous for the full melt crystallization throughout the film thickness. The laser beam is linearly polarized in the laser head with the green light polarized orthogonally to the laser base plate. The vertical to horizontal polarization ratio of more than 100:1 is the polarization state of the green laser output upon exiting the laser head. The highly parallel beam with Gaussian profile measures a beam diameter of 2.25 mm at I_0/e^2 intensity.

This parallel laser beam then passes through a set of two 70 mm focal length lenses that work as beam expander to ensure appropriate beam diameter of 2.25 mm is produced before going through a diffractive optical element (DOE). Gaussian beam from the laser head transformed into a line beam upon exiting the DOE resulted by the phase change in the laser spot. The line beam with a dimension of 470 μm × 8 μm with rounded-top or Gaussian-like

profile in the long axis and narrow Gaussian profile in short axis was then focused on the XY-axis motorized stage by a 50 mm focal Plano-convex lens. The schematic of the simple laser system set up is shown in Figure 2.1. The laser scan was completed by means of stage movement in the direction parallel to the laser beam short axis on the 15 mm × 15mm sample

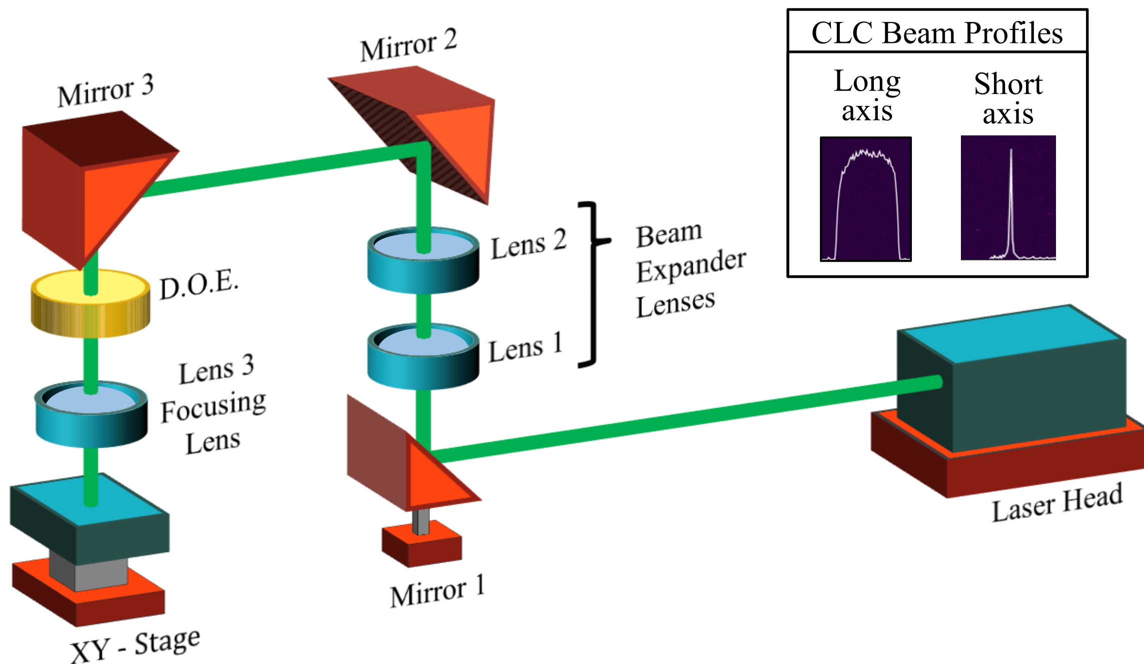

Figure 2.1: Schematic of table-top laser system for crystallization. The inset shows the final output beam profiles in long and short axes used for the CLC process.

with the stage maximum translational speed of 15 mm/s. The single scan CLC process was performed in air ambient with substrate temperature kept at room temperature.

2.1.2 Sample preparation

A single a-Si layer deposited on the quartz substrate covered by SiO_2 was used for the laser crystallization. The structure of the sample for the laser crystallization is shown in Figure 2.2. The quartz substrates were first subjected to inductively coupled plasma-chemical vapor deposition (ICP-CVD) chamber for hydrogenated a-Si (a-Si:H) deposition with silane (SiH_4)

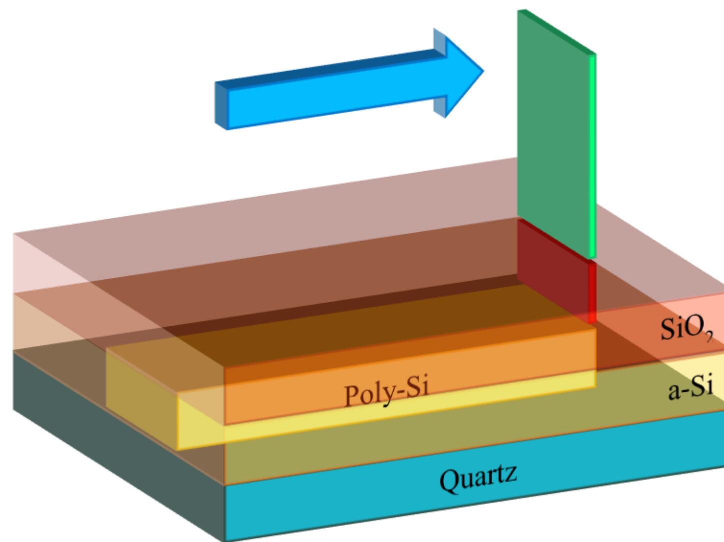

Figure 2.2: Sample structure and laser crystallization schematic.

at 250 °C and 6.7 Pa. Substrates were then cleaned by piranha solution with the mixture of sulfuric acid (H_2SO_4) and hydrogen peroxide (H_2O_2) to remove organic residue on the surface. The substrates then rinsed and transferred into 1:100 solution of diluted hydrofluoric acid (DHF) for 1 minute at room temperature to remove thin oxide layer and ionic contamination. Substrate cleaning by Radio Corporation of America (RCA) was performed afterwards where the first standard clean (SC-1) was done by immersing the sample into the 4:1:1 volume ratio of deionized water, aqueous H_2O_2 and ammonia solution (NH_3OH) for 10 minutes in 80 °C water bath to remove organic residues and insoluble particles that reside on the surface. Oxide stripping by DHF was then repeated after SC-1. The second standard clean (SC-2) follows by submerging the substrates into a mixture of 4:1:1 deionized water, H_2O_2 and hydrochloric acid (HCl) for 10 minutes in 80 °C water bath to remove metallic contaminants which may introduced in the SC-1. Once again, DHF immersion was repeated to finish the cleaning process.

Subsequently, SiO_2 caping layer (C/L) was deposited on the samples by means of plasma enhanced chemical vapor deposition (PECVD) by the reaction of tetraethoxysilane

(TEOS, $Si(OC_2H_5)_4$) and oxygen (O_2) precursors at 300 °C, 80 Pa and radio frequency (RF) power of 150 W. The SiO_2 C/L thickness was varied from 86 nm to 160 nm with the TEOS PECVD at a deposition rate of 13.3 nm/min. The sample was then subjected to dehydrogenation (de-H) annealing at 550 °C for 1 hour in nitrogen (N_2) gas ambient as the final step in the sample preparation process to reduce the hydrogen content in the a-Si layer. The sample preparation process is illustrated in Figure 2.3 and the respective process conditions are summarized in Table 2.1.

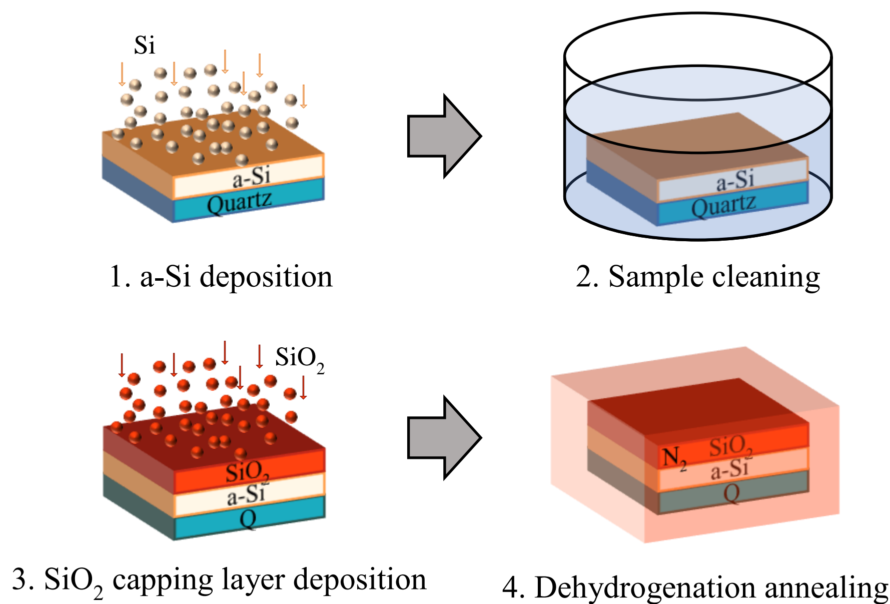

Figure 2.3: Schematics of sample preparation process.

2.1.3 Film characterization techniques

The study of the crystal texture after the crystallization process were carried out mainly by EBSD where the module is integrated in Hitachi SU6600 low vacuum scanning electron microscope (SEM). The electron acceleration voltage was set at 15 kV and the sample was tilted at 70° from horizontal. Crystal orientation analysis are done by orientation imaging microscopy (OIM) technique by EDAX. The backscattered electron exiting at the Bragg condition form Kikuchi bands and imaged by a phosphor screen located within the specimen

chamber. The indexing of the collected pattern underwent mathematical routine using a modified Hough transform to locate each band location which then enable to relate these locations to the underlying crystal orientation. Figure 2.4 shows the schematics of sample and detector configurations in EBSD and the obtained Kikuchi pattern for orientation mapping.

The capability of the EBSD in precisely determining the orientation of measured specimen in 3-directional configuration is necessary in laser crystallization study in which the control of the crystal growth and its orientation in these directions is a big concern when judging the crystal quality of the poly-Si. Those three directions are normal direction (ND) which is the direction perpendicular to the sample's surface, scan direction (SD) which referred to the direction parallel to the laser scan direction and finally transverse direction (TD) which is the direction perpendicular to both ND and SD as shown in Figure 2.4 with the thick arrows. The orientation of the crystal grains was mapped in the EBSD by the inverse pole figure (IPF) with predetermined color code in all the three directions.

Figure 2.5 shows an example of the IPF mapping in EBSD analysis for the film crystalized at 2.1 W laser power having 125 nm C/L. In addition to IPF grain orientation

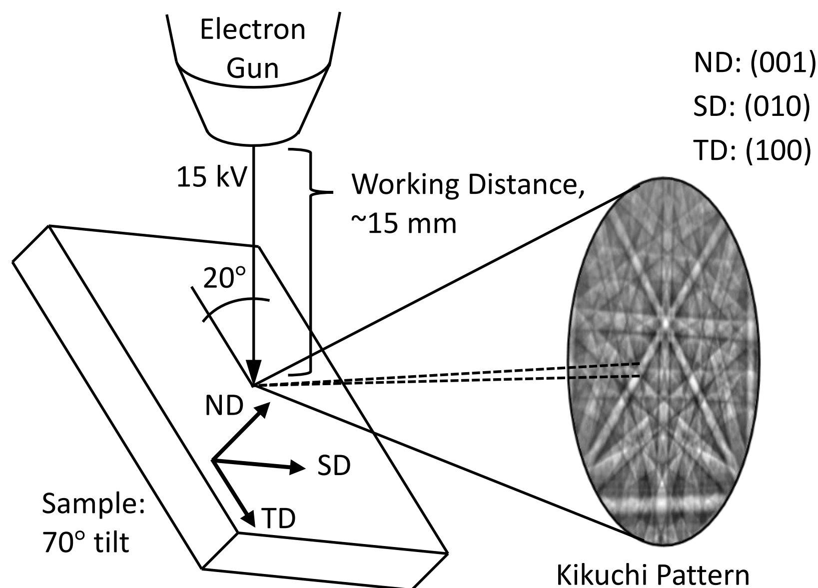

Figure 2.4: EBSD schematic diagram with sample tilt angle set at 70° and Kikuchi pattern generated by diffracted electrons.

mapping, grain boundary (GB) mapping also common in the EBSD analysis with the grain misorientation angle (GMA) of interest can be selected. In the silicon crystallization technology, 15° GB usually referred as high angle GB and GB formed between grains with misorientation angle of less than 15° is referred as low angle GB [1,2]. Figure 2.5 (d) shows the GMA 15°-65° where the grayscale lines formed when the two adjacent grains are 15°-65° rotated against each other. The same representation is applied with the GMA 2°-65° as shown in Figure 2.5 (e).

Additionally, other common crystal characterization techniques also done for the crystallized film including atomic force microscopy (AFM) to study the surface morphology of the poly-Si surface, electron microscopy to observe the crystal arrangement as well as Raman spectroscopy to investigate the induces strain in the film apart from crystallinity confirmation**.**

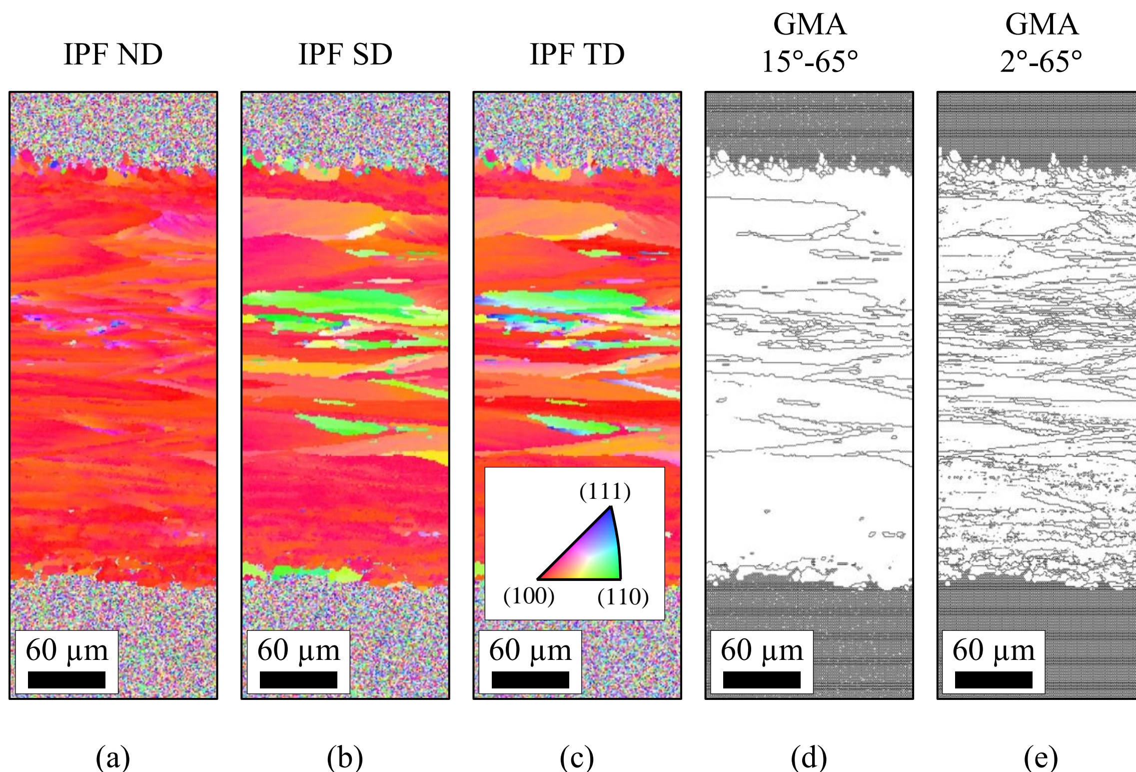

Figure 2.5: IPF images from EBSD in (a) normal direction (ND), (b) scan direction (SD), and (c) transverse direction (TD). The inset in (c) show the color code for the orientations of the crystal domains used in IPF ND, SD and TD. Grain misorientation angle (GMA) are shown in (d) for GMA 15°-65° and (e) for GMA 2°-65°.

Table 2.1: Sample preparation processes with process conditions.

1. A-Si deposition: thickness = 60 nm.	1. ICP-CVD -: SiH_4, 250 °C, 6.7 Pa.
2. Sample cleaning. 2.1. H2SO4 clean. 2.2. RCA clean.	2. Cleaning -: 2.1. H_2SO_4 clean -: 2.1.1. H_2SO_4:H_2O_2 = 1:1 (10 mins, 80 °C). 2.1.2. Oxide stripping -: HF:H_2O = 1:100 (1 min, 25 °C). 2.2. RCA clean -: 2.2.1. SC-1 -: H_2O:H_2O_2:NH_3OH = 4:1:1 (10 mins, 80 °C). 2.2.2. Oxide stripping -: HF:H_2O = 1:100 (1 min, 25 °C). 2.2.3. SC-2 -: H_2O:H_2O_2:HCl = 4:1:1 (10 mins, 80 °C). 2.2.4. Oxide stripping -: HF:H_2O = 1:100 (1 min, 25 °C).
3. SiO_2 cap layer deposition: thickness = 84, 125, 140, 160 nm.	3. PECVD -: TEOS-CVD: TEOS:O_2 = 3:300 sccm, 300 °C, 80 Pa, RF power = 150 W.
4. Dehydrogenation annealing.	4. N_2, 550 °C, 1 hr.

2.2 Effect of capping layer on laser crystallized Silicon film

It has been reported that the incorporation of silicon dioxide (SiO_2) capping layer (C/L) on top of the a-Si layer are effective in increasing the grain size in the laser crystallization of poly-Si. C/L layer serves as heat reservoir and an anti-reflection layer during the laser crystallization [3–5].

2.2.1 Heat storing

Theoretically, silicon film and underlying glass substrate stored a certain amount of heat, Q_{Si} and Q_{SiO_2} respectively upon laser irradiation and increases the temperature of the silicon film. Without the C/L layer, the total energy Q of the system will be

$$Q = Q_{Si} + Q_{SiO_2}. \tag{2.1}$$

Thermally conductive silicon film tends to diffuse the heat vertically deeper onto the substrate and upward into the air, since the lateral diffusion are negligible due to small variation in light intensity along the direction. Introduction of a C/L not only prevents the absorbed heat by sandwiched silicon layer from escaping into air, but the stored heat in the C/L itself helps the molten silicon to delay the onset of nucleation. The total energy of the system with C/L become

$$Q = Q_{CL} + Q_{Si} + Q_{SiO_2}, \tag{2.2}$$

where Q_{CL} is the absorbed heat by the C/L. By having SiO_2 C/L with slightly lower thermal conductivity (κ_{SiO_2}) of 1.1 ~1.2 W/mK compared to that of a-Si film layer (κ_{a-Si}) of about 1.5 W/mK at room temperature, the released heat by the high temperature silicon layer will be stored in the C/L layer upon laser irradiation and subsequently returns it to the silicon layer when the silicon temperature drops [6–8]. As a result, the melting time of the silicon is kept longer and elongated grains is expected by the slow solidification process. Figure 2.6 shows the temperature profile of the structures with and without the C/L layer reported by W. Yeh and M. Matsumura, Jpn. J. Appl. Phys. **41**, 1909 (2002) [8]. Incorporation of C/L layer helps in

reducing the thermal gradient at the back interface of the sample which serve its purpose as a heat reservoir for the system [3,9].

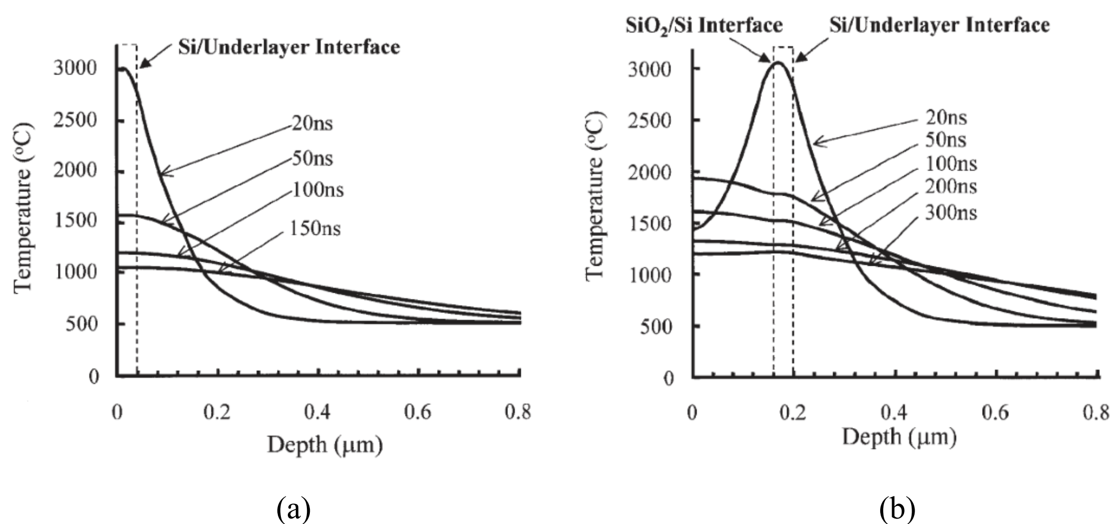

Figure 2.6: Temperature profile in the system (a) without capping layer and (b) with SiO_2 capping layer. After W. Yeh and M. Matsumura, Jpn. J. Appl. Phys. 41, 1909 (2002).

2.2.2 Anti-reflection

The C/L layer also aids in reducing the reflection of the irradiated laser light onto system which resulting in lower threshold laser power to start the crystallization process [10]. Apart from reflection of light at the interface of two different refractive indices media (air and C/L), interference of irradiated laser light on the C/L surface and the reflected light wave on the back surface of the C/L film also determine the reflectivity of the system. Figure 2.7 shows

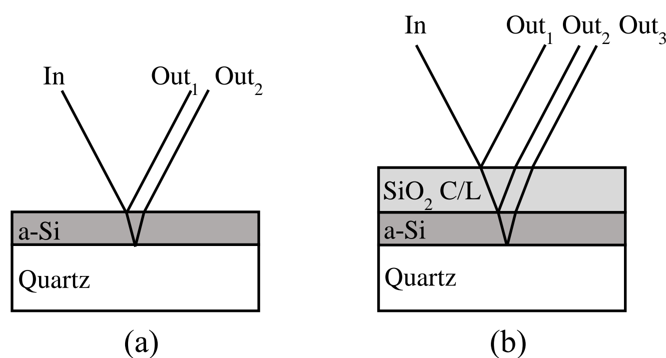

Figure 2.7: Schematic of reflection of light upon irradiation on sample (a) without capping layer and (b) with capping layer.

a schematic of the reflection of irradiated light onto a surface with and without the incorporation of the C/L layer. Reflectance, R of the laser beam irradiated normal to the surface can be determined by the Fresnel equation;

$$R = \left(\frac{\eta_0 - \eta_1}{\eta_0 + \eta_1}\right)^2, \tag{2.3}$$

where η_0 is the refractive index of the first medium (air) and η_1 is the refractive index of the top layer of the system (SiO_2 or a-Si). Taking into account the interference of light inside the thin layer of C/L, destructive and constructive interference of the reflected light from both top and bottom interface of C/L must be considered in order to minimize the reflectivity of the system's surface. With the thickness of the film that introduce optical path difference and thus phase change of the laser wavelength, the thickness selection for C/L is necessary to exploit this favor. Generally, the reflectance varies periodically with C/L thickness due to the phase change and interference of light wave [11].

2.2.3 Experimental results

The effect of the SiO_2 C/L was first investigated by comparing the crystal quality crystallized with and without the C/L. The samples with native oxide (~ 3 nm) and 125 nm SiO_2 deposited C/L by PECVD was compared. Figure 2.8 (upper images) shows the optical microscope (OM) images of the laser scan regions for both samples. Sample without C/L was crystallized at 2.5 W and the one with 125 nm C/L was crystallized at 2.1 W by the stage translation speed of 15 mm/s. The corresponding IPF ND and GMA 15°-65° images are shown in Figure 2.8 (lower images). The laser power selection of 2.5 W and 2.1 W were considered since these conditions lies within the windows for (100) ND formation for both samples. From the IPF ND images, it was confirmed that the (100) crystal growth in ND are dominant; independent of the incorporation of the SiO_2 C/L. Since the growth of the crystal starts from the bottom of the a-Si melt, the interface of a-Si/quartz is the key reason for the {100} poly-Si growth in the ND where low {100} silicon-SiO_2 (quartz) interface energy governs the

preferential growth of {100} plane [12–15]. Lateral growth of poly-Si parallel to the direction of the laser scan from right to left side is confirmed for the sample with 125 nm C/L. Heat storing capability of the system with C/L does help in prolonging the melt duration of the silicon film thus slows down the solidification process as the laser beam travels. The C/L successfully reduce the thermal gradient of the silicon film to the back substrate to enhance the lateral growth. As a result, grains with several hundreds of micrometers in length can be grown with the aid of the 125 nm C/L.

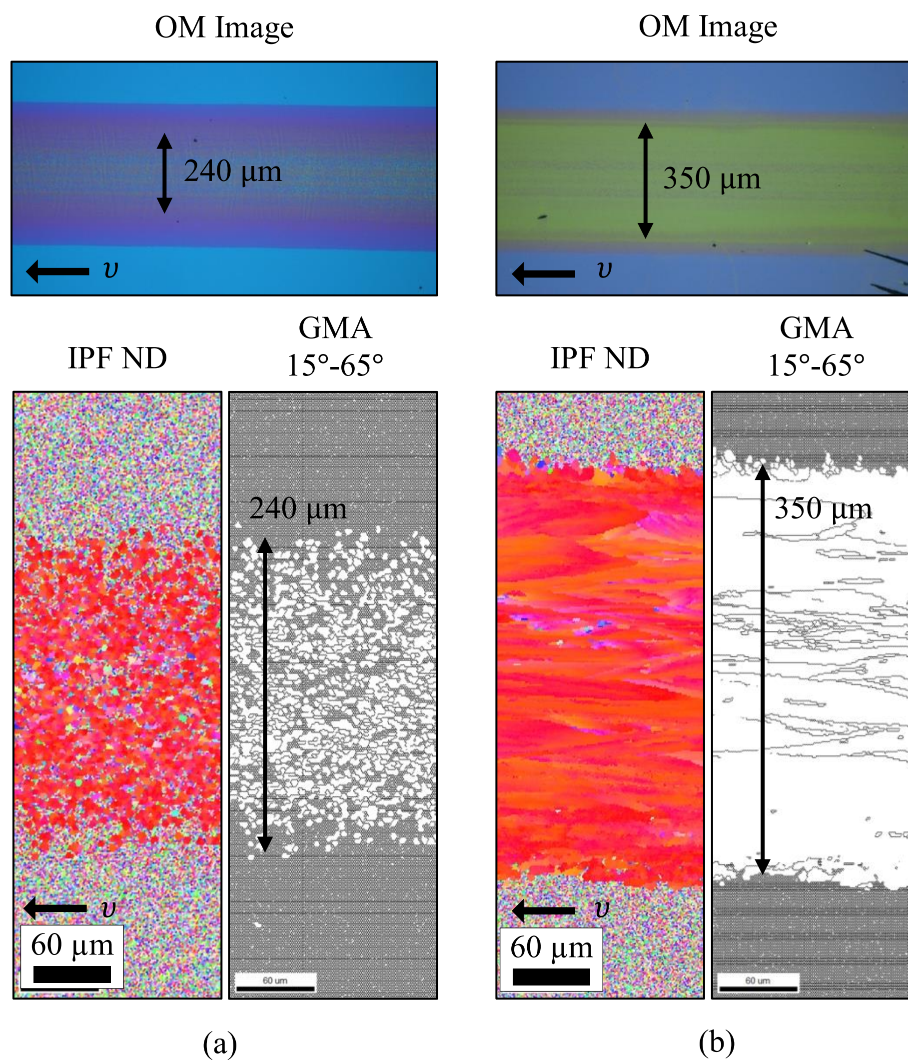

Figure 2.8: Optical microscope, inverse pole figure in normal direction and grain misorientation angle 15°-65° images of laser scan area of sample (a) without C/L crystallized at 2.5 W and (b) with 125 nm C/L crystallized at 2.1 W.

On the other hand, polygonal grains with diameters in the range of several micrometers are grown without the SiO_2 C/L. The growth mechanism of this microcrystalline silicon (μc-Si) grains is similar to the one crystallized by pulsed laser irradiation where rapid-vertical heat loss during the crystallization forces the vertical growth from bottom to surface of the silicon film [16,17]. The so-called rapid quenching leads to the formation of hillocks on the poly-Si surface as can be seen from AFM surface morphology image shown in Figure 2.9(a) [18–20]. The protrusions are avoided for the samples covered by the C/L as the SiO_2 C/L layer having smaller melting temperature compared to a-Si behaves as a solid mould when the silicon film melts; resulting in poly-Si with smoother surface as shown in Figure 2.9(b). The root-mean-square surface roughness R_{RMS} of the poly-Si surface measured on 30 μm × 30 μm square region was 7.726 nm and 1.658 nm for the sample crystallized without C/L and with 125 nm C/L respectively. Figure 2.10 shows the IPF ND images of the crystallized samples with 0 nm, 84 nm, 125 nm, 140 nm and 160 nm C/L covering the a-Si upon laser irradiation. As mentioned earlier, the (100) oriented grains in ND are dominant in CLC on quartz substrate regardless the thickness of the C/L.

Below the laser power threshold for the (100) formation, nanocrystalline silicon (nc-Si) was observed and for higher laser power over the (100) ND window, microcrystal-like structure was grown. At extremely high laser power, film damage was seen as there were too much energy been irradiated which causes the film ablation. A clear laser power window for the (100) growth in ND was observed and the power range are different for each case with different C/L thickness due to the difference in anti-reflection and heat storing capabilities of each system with different C/L thicknesses. While the laser power threshold for the (100) ND growth follows the trend of the sample reflection upon laser irradiation, the lateral growth of the poly-Si is dominated by the ability of the C/L to reserve the heat in the system. In conclusion, the use of SiO_2 C/L is advantageous in controlling the lateral growth of poly-Si.

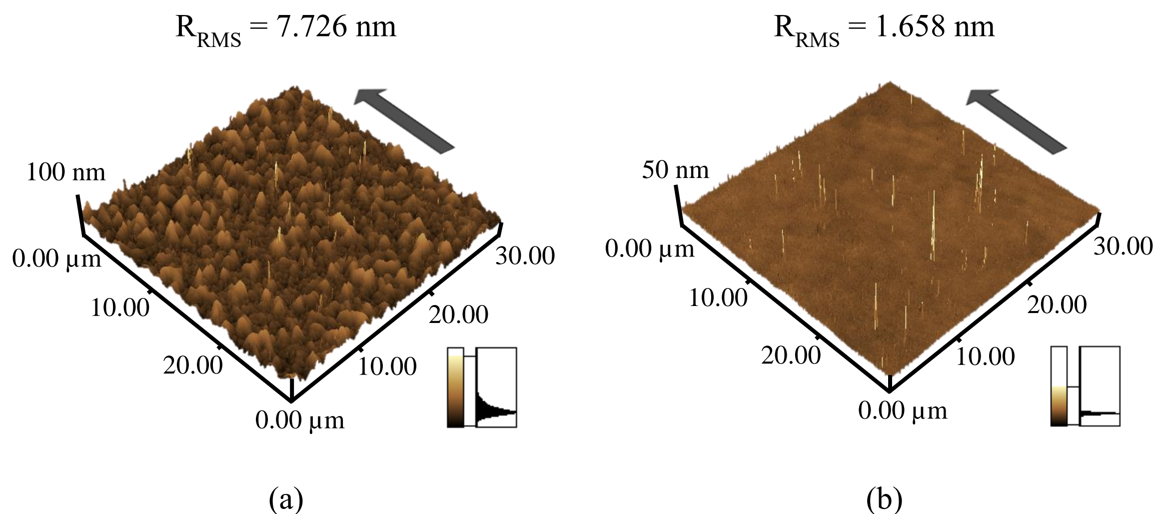

Figure 2.9: AFM images of poly-Si surface after crystallization (a) without C/L and (b) with 125 nm C/L. Root mean square roughness are shown for both cases. Thick arrows show the laser scan direction.

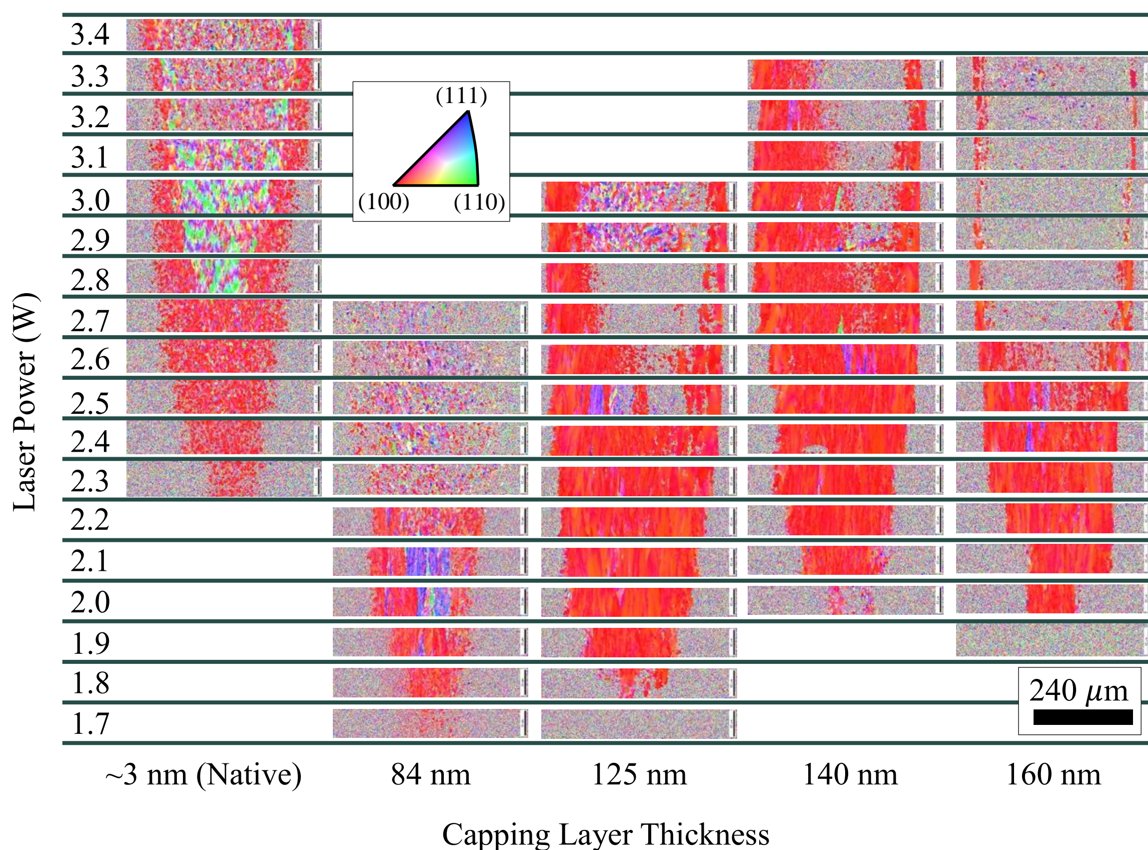

Figure 2.10: Inverse pole figure in normal direction for the laser power dependence with different capping layer thicknesses. Laser scan direction was in vertical direction for each image.

2.3 Crystal quality of grown poly-Si by CLC

The use of SiO_2 C/L is advantageous in keeping the lateral growth of poly-Si. However, controlling the growth behavior of silicon film is challenging as there are other parameters to be considered. It was reported that the use of the pencil-tip Gaussian beam for CLC resulted in three regimes of crystallization namely; (1) Fully liquid crystallization at the center of the laser trace, (2) Partial liquid phase growth at the regions with less irradiation power, and (3) Solid phase crystallized region at the much lower power region near the edge of the laser beam [21]. The least irradiated region produced partially crystallized silicon where grain with diameter of less than 20 nm or nanocrystalline silicon (nc-Si) were surrounded by clusters of uncrystallized a-Si. The use of the line beam having a dimension of 470 μm × 8 μm with rounded-top or Gaussian-like profile in the long axis used in the CLC are expected to give more control on the heat flux especially at the full-melt region as the dependency on Gaussian profile in laser scan direction are minimized. Extended crystal quality analysis is needed in order to give wider view on the crystallographic of the poly-Si.

2.3.1 Raman spectroscopy

The use of low laser irradiation power does transfer sufficient heat for local nucleation but low enough to crystallized the whole thickness of the silicon film. The partial crystallization by low laser power was analyze by Raman spectroscopy with 532 nm laser light source. Figure 2.11 shows the Raman frequencies for the laser crystallized silicon film embedded under 160 nm C/L with laser power ranging from 1.5 W to 2.0 W and the corresponding OM pictures for the CLC trace. The arrows indicate the direction of the laser power increase. From the Raman frequencies in Figure 2.11, two distinct peaks of the optical phonon mode (OPM) appeared which represent the a-Si peak (blue curve) around 480 cm^{-1} and poly-Si peak (red curve) around 510 cm^{-1}. Increasing the laser power diminishes the a-Si peaks as higher fraction of the a-Si being crystallized into poly-Si which is represented by the increase in the poly-Si peaks. In

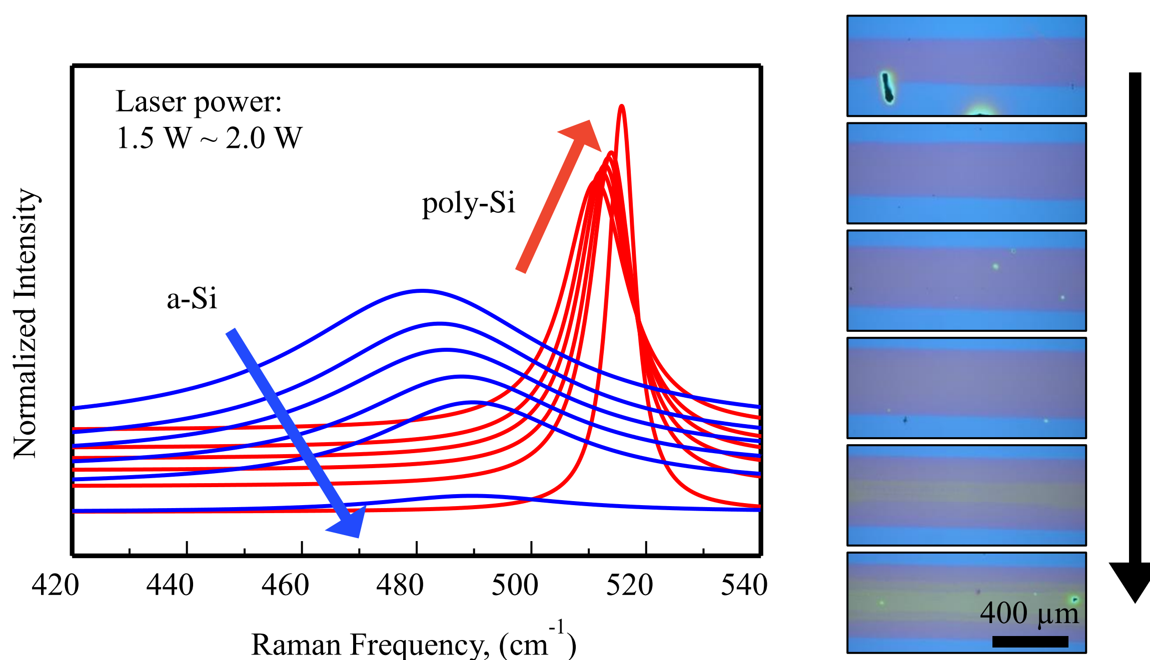

Figure 2.11: Spectra of Raman frequencies of a-Si (blue curves) and poly-Si (red curves) for laser scanned region under 160 nm C/L by 1.5 W to 2.0 W laser power. Pictures on the right shows the corresponding optical microscope images of the laser trace. The arrows indicate the direction of the increase of laser power.

general, the Raman frequency peak for c-Si is 520 cm^{-1} and this peak number is the reference for analyzing the stress induced in the poly-Si films. In this CLC poly-Si, the peak frequency shifted to a lower values compared to that of c-Si which indicate the induced tensile stress in the poly-Si film [22].

With increasing laser power, the shift of the peak frequency from c-Si peak ($\Delta\omega$) reduces since more fraction of a-Si has been crystallized and stress has been released in the process [23]. The frequency peak of the poly-Si shifted towards the c-Si peak as the laser power increased and saturated at ~516 cm^{-1}. In the crystallization of silicon film on an insulating substrate, a residual biaxial tensile stress is induced in the laser crystallization and it is attributed to the low thermal expansion coefficient of the substrate compared to the silicon film, in contrast with that of silicon crystallization on sapphire substrate [24]. Apart from reflecting

upon defect density, the ordering of the lattice structure as well commonly denoted by the full width at half maximum (FWHM) of the curve which also in conjunction with the experimental result with increasing laser power. Figure 2.12 shows the plot of frequency shift $\Delta\omega$ and FWHM against the laser power for the sample with the 160 nm C/L. After the threshold laser power for crystallization of 2.0 W, both Δω and FWHM remain unchanged regardless of the crystal orientation and crystallite size. It was reported that the high Δω and FWHM of 7 cm^{-1} and 8 cm^{-1} respectively is due to the incomplete or incipient crystallization with the formation of poly-Si crystals in the order of 100 Å in size.

The tendency is similar for other samples crystallized under different thicknesses of C/L as shown in Figure 2.13. Blue plots show the poly-Si peaks for low power CLC where a-Si peaks also detected, the red plots represented the Raman frequency peaks of (100) oriented poly-Si in ND and the black plots for the peaks at higher laser power where (100) ND was deteriorated as can be seen in EBSD mappings from Figure 2.10. For reference, the calculated spatial correlation model by Z. Iqbal et al., Solid State Commun. 37, 993 (1981) was sketched and is indicated by solid line [25][26][27]. The dashed line is the low-frequency peak shifts

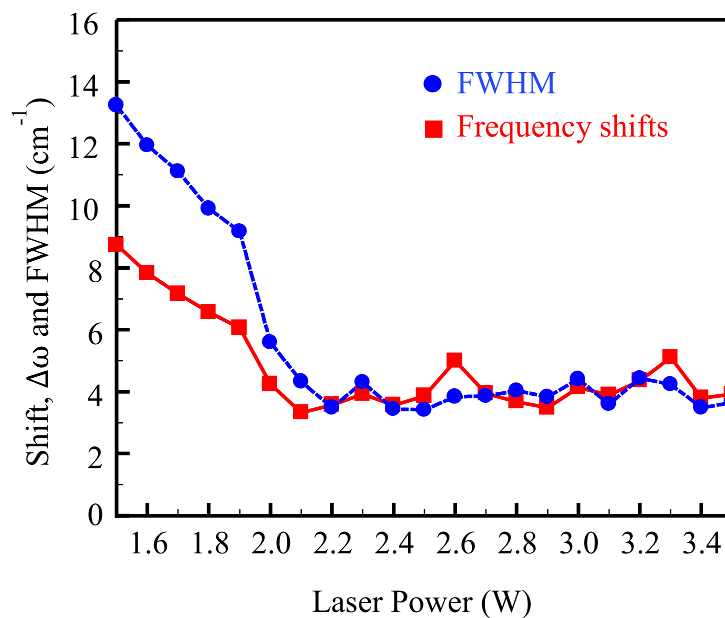

Figure 2.12: Raman frequency shift and FWHM of poly-Si crystallized under 160 nm C/L at laser power of 1.5 W to 3.5 W.

(greyed area) estimated from the obtained OPM of the CLC poly-Si which deviated about 2.8 cm^{-1} above the model values due to the residual thermal stress. This value is consistent to the estimated value of 2.75 cm^{-1} calculated using the equation:

$$\tau_{Th} = \frac{(\alpha_{Si} - \alpha_S)\,\Delta T}{S_{11} - S_{12}}, \text{ and} \tag{2.4}$$

$$\Delta\omega = \frac{\tau_{Th}}{P} \tag{2.5}$$

where α_{Si} and α_S are the thermal expansion coefficients of Si and the substrate, respectively, ΔT is the difference between the regrowth temperature or melting point of a-Si (1430 K) and room temperature (RT) of 300 K, and the compliance constants, S_{11} and S_{12} for Si are given as 0.7691×10^{-12} and -0.2142×10^{-12} cm^2/dyn, respectively. The proportional constant, P, is 2.49×10^9 dyn/cm. A mean value of 3.9×10^{-6} K^{-1} for α_{Si} over a temperature range from 300 K to 1300 K was used in the calculation as the value is temperature dependent while the α_S of

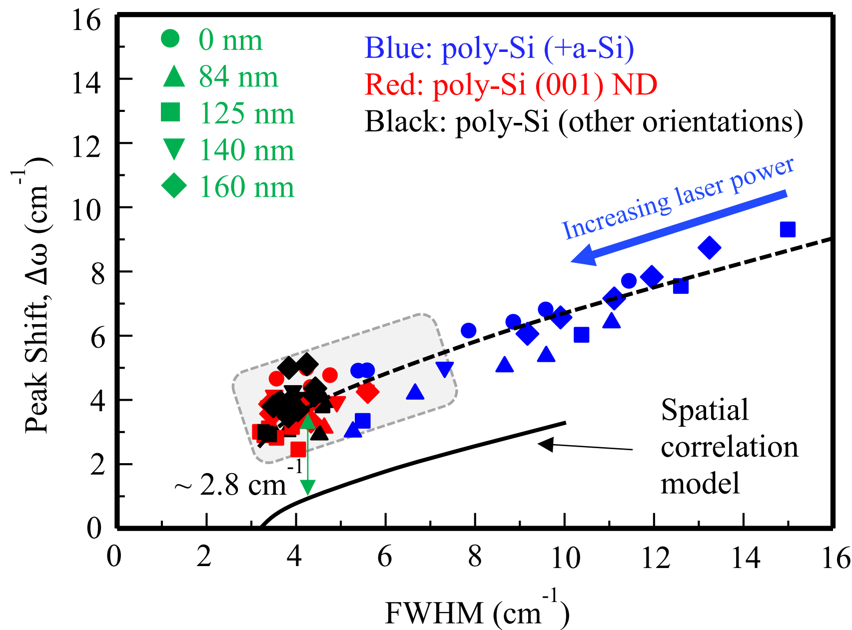

Figure 2.13: Plot of Raman frequency peak shift against FWHM for CLC with different C/L thickness. Spatial correlation model calculated by Z. Iqbal et al., Solid State Commun. 37, 993 (1981) is drawn with the solid line. Deviation of low-frequency shift (greyed area) about 2.8 cm^{-1} from the model plot is due to biaxial tensile stress of the crystallized film which agrees with the calculated value.

0.54×10^{-6} K^{-1} for fused quartz substrate was used. The FWHM of the Raman peaks that described the structural distribution of the lattice can be useful to compare the defects density of the crystallized film. However, the FWHM values are almost similar with the CLC above the threshold power for full crystallization represented by red and black plots regardless of the poly-Si grain size and orientation observed by the EBSD as shown in Figure 2.10. Additional characterization techniques are necessary in order to study the crystal lattice of the poly-Si in detail in addition to EBSD and Raman microscopy.

2.3.2 Scanning transmission electron microscopy (STEM)

Crystal lattice of the crystallized poly-Si by CLC was further analyzed by scanning transmission electron microscope (STEM) in which the ~ 20 μm × 3 μm specimen was prepared by focused ion beam (FIB) milling and thinned to less than 300 nm in the short axis to confirm the properties of the film and hence to deduce the possible mechanism of the crystal growth with varying laser power. Figure 2.14 shows a schematic of the specimen pick up position on the laser scan trace with observation plane indicated by the thin arrow. The respective picked-up specimen captured by scanning ion microscopy (SIM) is shown in Figure 2.15(a) and the thinned specimen is shown in (b). Figure 2.16 shows the STEM image in transmission electron microscopy (TEM) mode of the 160 nm capped film crystallized at 1.8

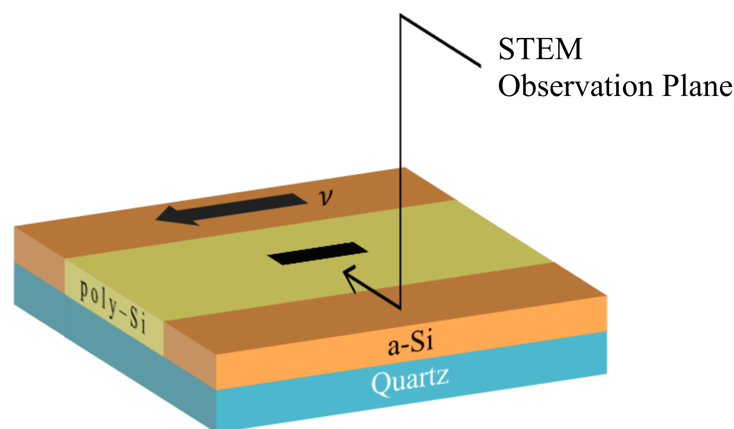

Figure 2.14: Schematic of specimen pick up position on laser scan trace. The thin arrow indicates the STEM observation plane.

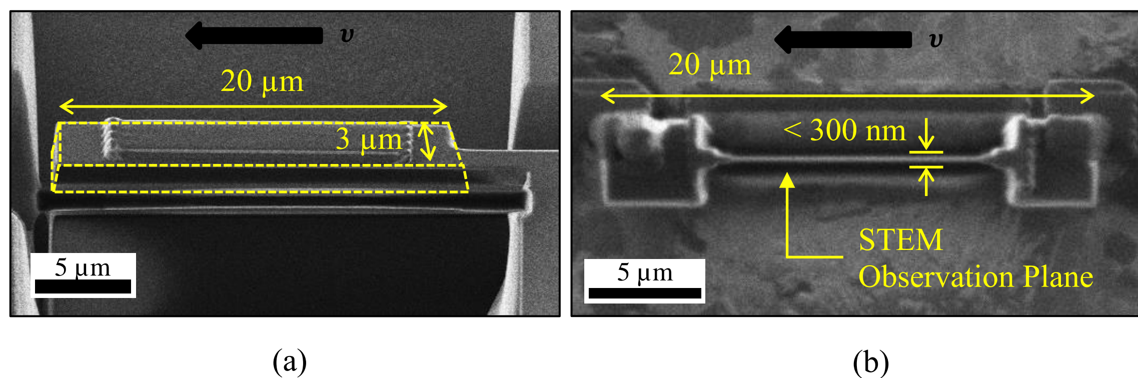

Figure 2.15: Specimen preparation for STEM observation (a) during pick-up process with specimen dimension of 20 µm × 3 µm and (b) thinning process of specimen in short axis to less than 300 nm. STEM observation plane also indicated in (b).

W together with the fast Fourier transform (FFT) image as well as IPF ND from EBSD. The laser scan direction is in the horizontal direction for the STEM case. Analyzed IPF ND with ×600 magnification shows no distinct crystal domains in micrometer size even though poly-Si peaks are visible from Raman spectroscopy; which suggests incipient crystallization. STEM observation confirms the crystallization of a-Si into nc-Si with crystallite length of 4~20 nm in addition to the FFT image which shows a clear continuous ring as well as several bright spots which suggest the presence of nanocrystals together with uncrystallized a-Si which usually termed as polymorphous state. At higher CLC power of 2.1 W, a clear single crystal-like lattice image was observed by STEM as shown in Figure 2.17 where the ordered lattice continues throughout the silicon film thickness of 60 nm. Clear bright spots are visible from the FFT image (inset) which rampant the claim that the observed region is a single crystal domain. From these observation with various methods, it complements each other for the formation of nc-Si and single crystal-like silicon film by the CLC process.

Additionally, STEM observation with both SEM and TEM modes at the center of laser trace with 2.7 W CLC power shows a formation of additional amorphous-like layer on top of the crystallized silicon film after the laser irradiation as shown in Figure 2.18(a). In this figure,

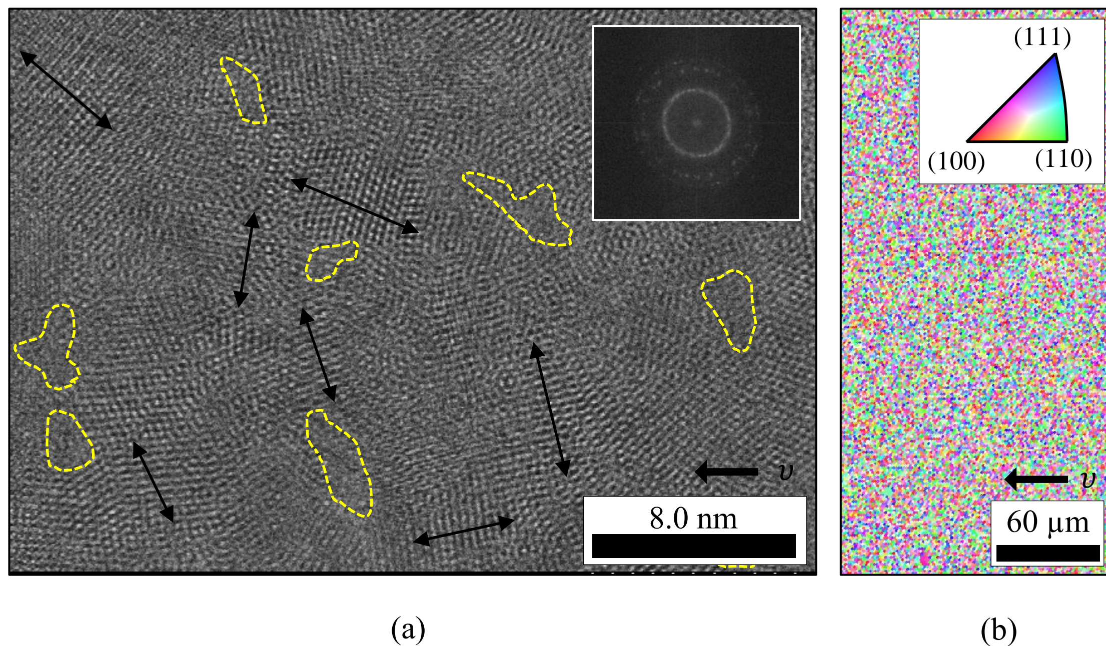

Figure 2.16: Crystal structure imaged (a) by STEM lattice observation with corresponding FFT image (inset) and (b) by EBSD IPF ND for sample with 160 nm C/L crystallized at 1.8 W laser power. The thin arrows in (a) shows the length of the nc-Si domain while the enclosed dotted yellow regions indicate the uncrystallized a-Si.

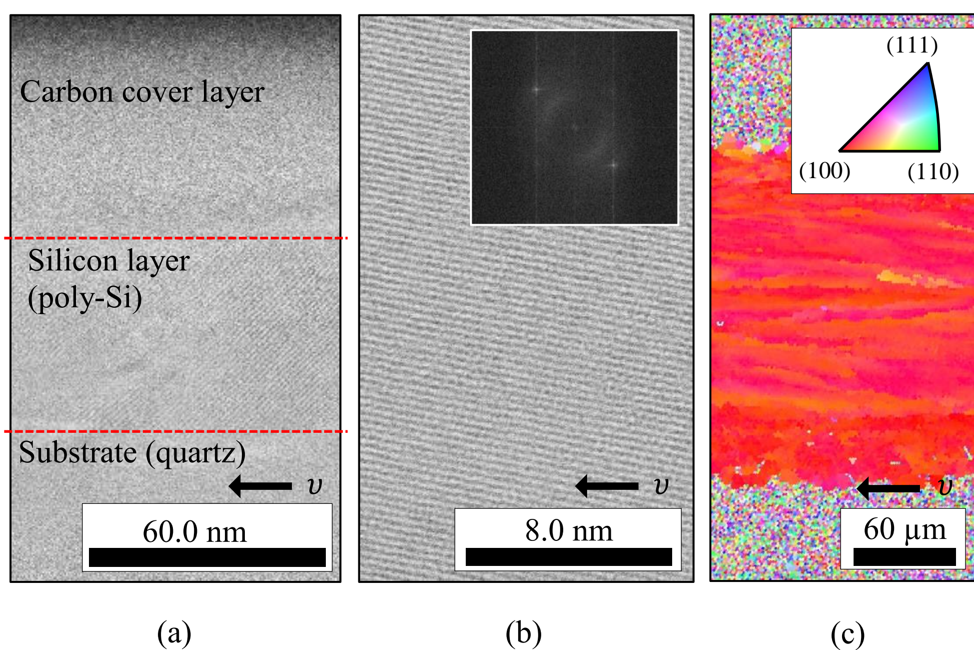

Figure 2.17: Cross section lattice structure in TD imaged (a) by STEM lattice observation at low magnification and (b) at high magnification with corresponding FFT image (inset). Normal orientation is shown by IPF ND in (c). CLC was done at 2.1 W under 160 nm C/L.

an additional layer was observed between the crystallized silicon layer and post-deposited carbon layer during FIB milling to prevent sample's surface damage. The formation of this additional amorphous layer on top of the crystallized silicon film is not properly justified. The 15 nm amorphous-like layer embedded a well crystallized single grain-like silicon film which also shows the ordered lattice structure similar to the one with 2.1 W CLC power. From this observation, it can be said that the poly-Si was grown in similar manner to the one with 2.1 W CLC power even though the EBSD observation shows the deterioration of the (100) ND crystal. Consistent Raman frequency peak around 516.0 cm^{-1} and FWHM about 4.0 cm^{-1} for the 2.1 W and higher CLC power hence correspond to the well crystallized grains although EBSD observation shows deterioration of large size and (100) oriented grains at laser power higher than 2.5 W. It is proposed that the thickness resolution of EBSD and Raman analysis does affect the outcome of the analysis for the crystallinity of CLC grown poly-Si.

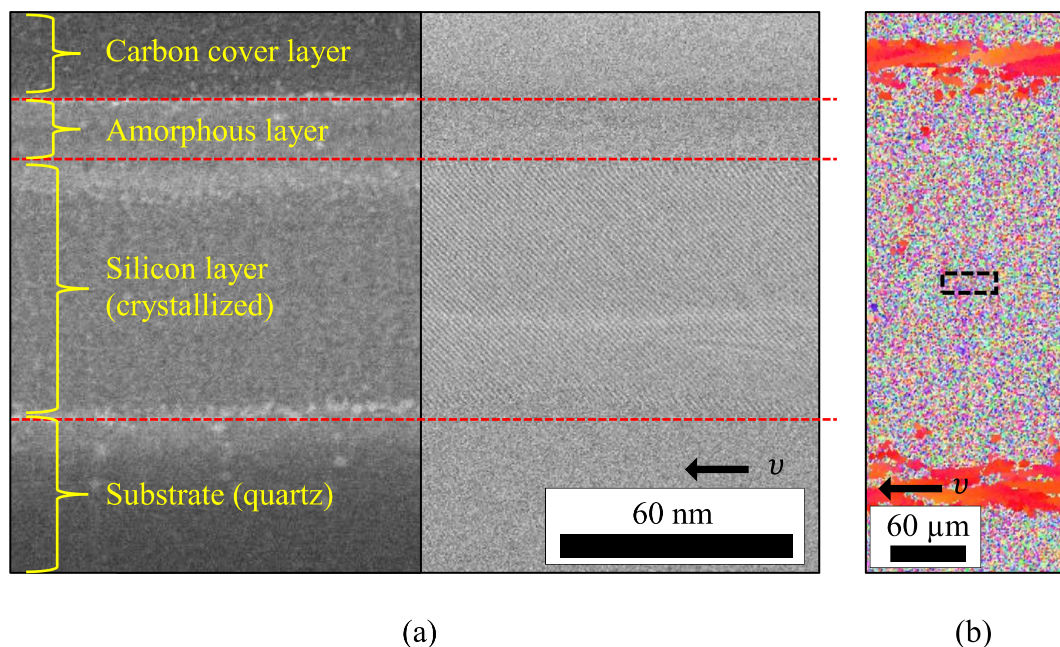

Figure 2.18: Crystal structure imaged (a) by STEM with SEM mode (left) and TEM mode (right) and (b) by EBSD IPF ND for sample with 160 nm C/L crystallized at 2.7 W laser power. Crystal growth is in the horizontal direction. Black dotted square in (b) shows the spot where specimen was extracted by FIB.

2.4 Evolution of crystal growth with varying laser power

The crystallinity of the CLC grown poly-Si was confirmed by the analysis of EBSD, Raman spectroscopy and STEM observation. It is crucial to understand the growth mechanism and its evolution with a change in crystallization parameter. It was ascertained that the incorporation of a SiO_2 C/L is beneficial in altering the growth mechanism of the embedded a-Si layer as discussed in section 2.2 where prolonging the melt duration helps to turn the vertical growth direction into in-plane horizontal growth to attain the lateral growth thus enlarged the crystal domains and reduced the surface roughness.

At low laser power it was observed that the partial crystallization occurs as can be seen in Figure 2.16 where nc-Si is surrounded by uncrystallized a-Si clusters. The phases coexistence throughout the silicon film is resulted by explosive crystallization in the vertical direction of the film thickness. The solid phase explosive crystallization allows the self-heat-propagation by means of latent heat release during the nucleation and crystallization of metastable a-Si clusters. In laser crystallization however, melt mediated crystallization is of greater interest due to possibility of single grain-like silicon growth with minimum GB formation. Figure 2.19 shows the GMA 15°-65° and the corresponding OM image of the laser scan trace done at 2.1 W under 160 nm C/L with the scanning speed of 15 mm/s. From the EBSD analysis (GMA 15°-65°), only lateral growth region of 211 μm wide is distinguishable while it is apparent that different color shades appeared on the OM image which correspond to different crystallization schemes.

Theoretically, stable temperature profile across the crystallization width allows the lateral growth in the laser scan direction keeping the crystal orientation undisturbed which reflected by stable heat distribution in the solid/liquid front. It was reported that the heat distribution on the irradiated sample in the long axis of the laser beam with Gaussian profile is sensitive to the set laser power. Figure 2.20 shows the model of the heat distribution in the

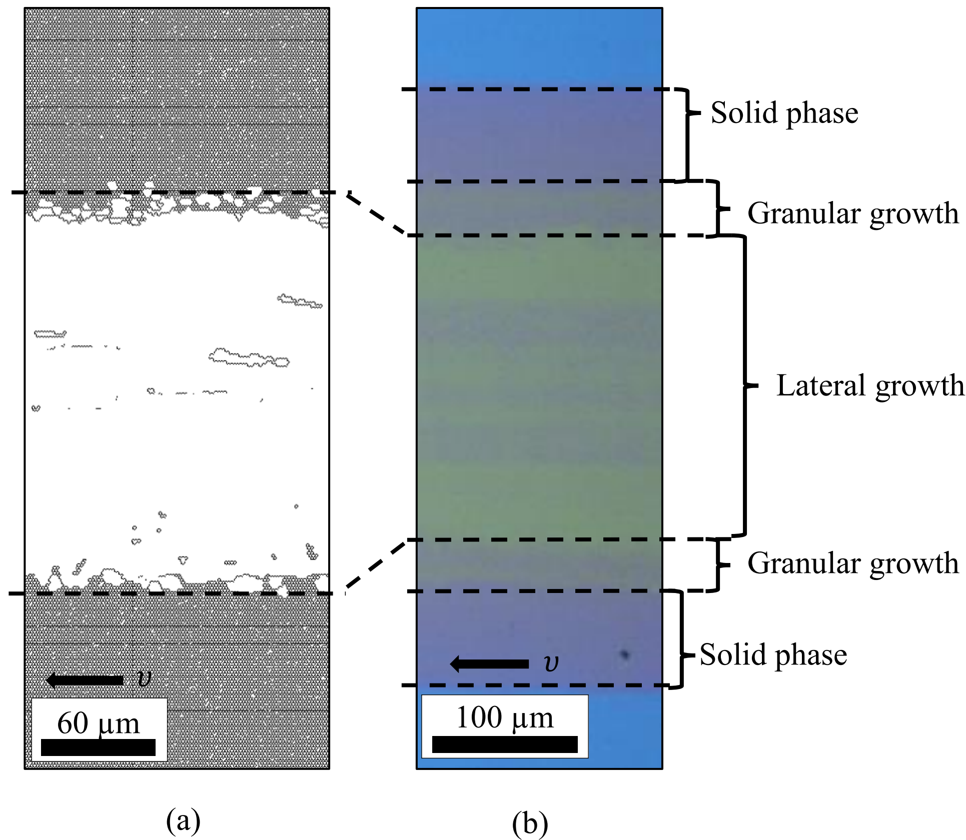

Figure 2.19: Laser trace region observed (a) by EBSD GMA 15°-65° and (b) by optical microscope. Laser scan was done at 2.1 W under 160 nm C/L at 15 mm/s.

direction perpendicular to the laser scan direction reported by G. S. Ganot, Dr. Thesis, Columbia Univ. (2012) for three different power conditions above the threshold for melt mediated crystallization with (a) optimum laser power condition with well distributed heat across melt width, (b) slightly higher power which lead to higher temperature at the center region of melt, and (c) too high temperature profile which eliminate the stable heat distribution on irradiated surface [28]. The model are extracted based on the in-situ black body emission images captured while the CW laser scan in progress with the laser beam spot having a Gaussian profile.

CLC at 2.1 W shown in Figure 2.19 shows that the grown silicon film is almost free from low angle grain boundaries (GBs) considering the GBs less than 15° are the low angle grain

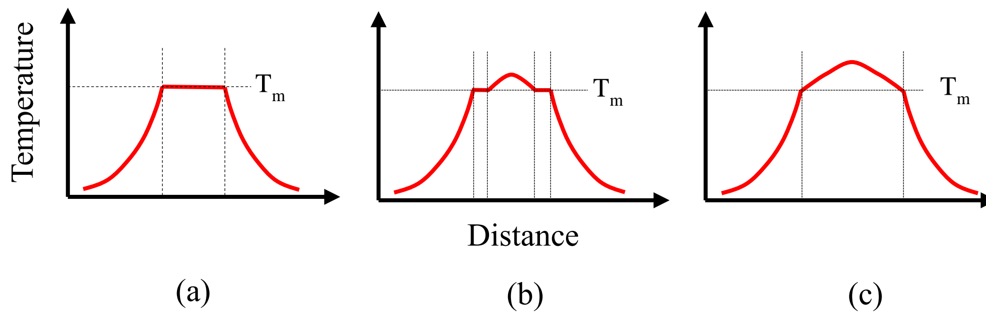

Figure 2.20: Temperature flux profile across the beam width on the irradiated silicon films above lateral crystallization threshold for (a) optimized power condition, (b) slightly higher temperature above optimized condition and (c) at much higher laser power. T_m is the melting temperature of crystalline silicon. The plot was analyzed and reported by by G. S. Ganot, Dr. Thesis, Columbia Univ. (2012) based on captured in-situ black body emission images.

boundaries which also termed as sub-grain boundaries (sub-GBs). To analyze the evolution of the silicon growth with different laser power and the formation of the GBs, a complete set of EBSD pictures for sample scanned under 160 nm C/L from 1.9 W to 2.7 W is shown in Figure 2.21 with (a) IPF ND, (b) IPF SD, (c) IPF TD, (d) GMA 15°-65°, and (e) GMA 2°-65°. It can be stipulated that the heat distribution from the laser scan width for CLC at 2.1 W follows the profile in Figure 2.20(a) while slight increase in laser power perturbed the temperature stability. The change in the temperature profile induces the GBs as the crystal growth direction in the higher temperature regions (center) is changed from the ideal condition. It can be seen from IPF SD and IPF TD in Figure 2.21(b) and (c) respectively, that <100> in-plane growth was deviated as the CLC power changed from 2.1 W to 2.2 W.

In an ideal condition, stable and uniform solid/liquid front allows the trailing solidification to continue following the growth of the seed which nucleated at the start of the laser irradiated region. High growth speed of {100} silicon plane ensures the orientation to dominate as the solidification advances. Figure 2.22 illustrates the solid/liquid interfaces of silicon upon laser irradiation (a) with straight solid/liquid front induced by uniform temperature

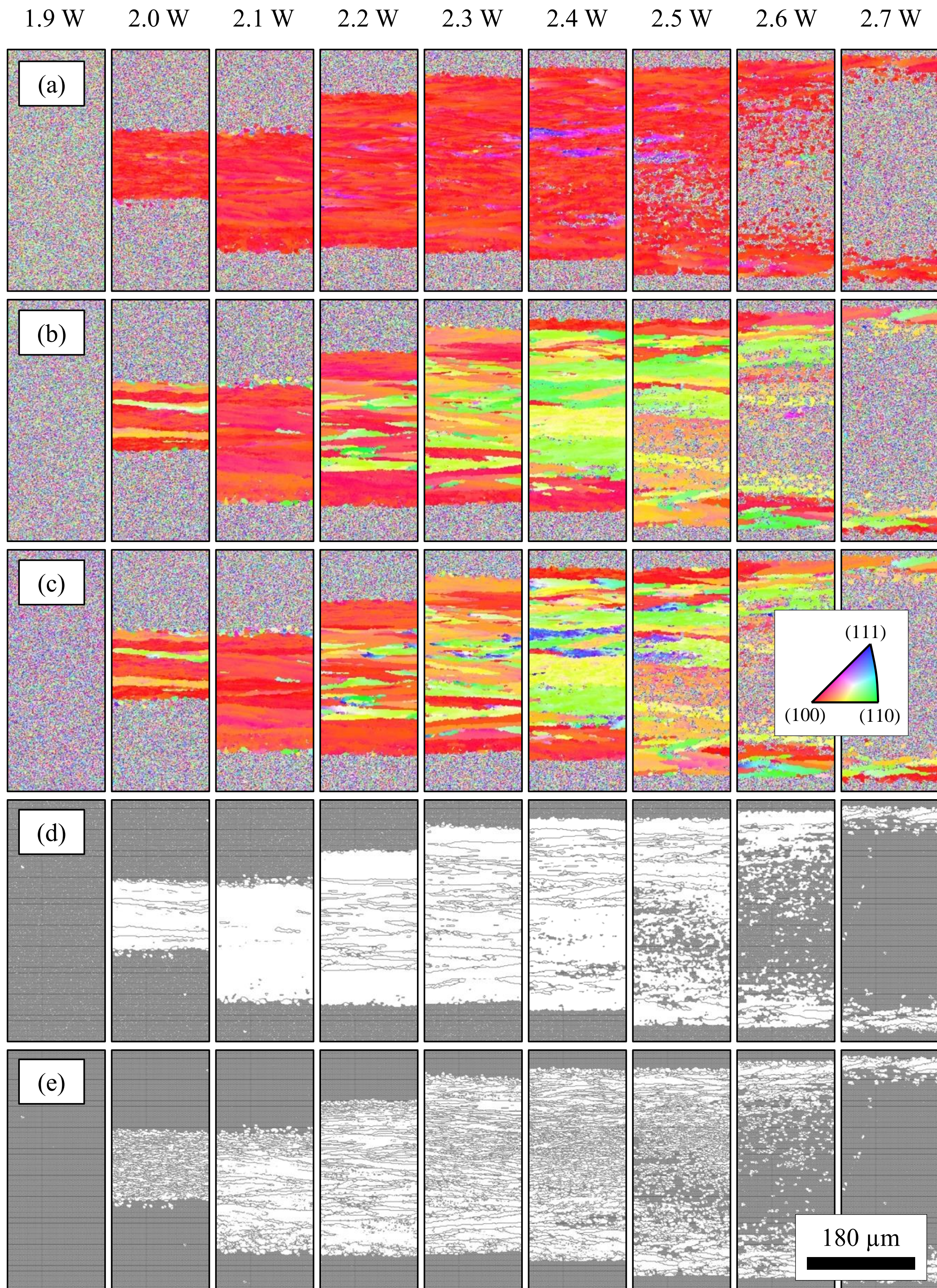

Figure 2.21: A complete set of EBSD pictures for single-scanned CLC from 1.9 W to 2.7 W under 160 nm C/L with (a) IPF ND, (b) IPF SD, (c) IPF TD, (d) GMA 15°-65°, and (e) GMA 2°-65°.

profile (Figure 2.20(a)) and (b) concaved solid/liquid interface at higher laser power. The stable isotherm parallel to the line beam allows the crystal growth parallel to the laser scan direction (scan direction, SD) and perpendicular to the isotherm. In this condition, the growth rate Rg of the averaged solid/liquid interface agrees with the laser scan velocity.

At higher laser power, higher temperature distribution at the center of the irradiated width causes longer melting time and thus deformed the stable solid/liquid interface. Consequently, in-plane rotation of grains about the [100] ND were observed and the resulting crystal orientation in SD rotated at an angle θ with respect to the preferred <100> in-plane growth. Slightly uniform temperature profile at the side (Figure 2.20(b)) keeps the stable heat distribution and thus retain the preferred {100} growth in SD at the peripheral of the scan trace. Figure 2.23 shows the IPF SD image obtained at 2.2 W CLC together with an illustration of $[0\bar{1}0]$ SD grains growth direction (red arrows) along the concaved solid/liquid interface. The resulting rotated grains are dominated by {310}, {210}, {110} and {320} crystal planes facing

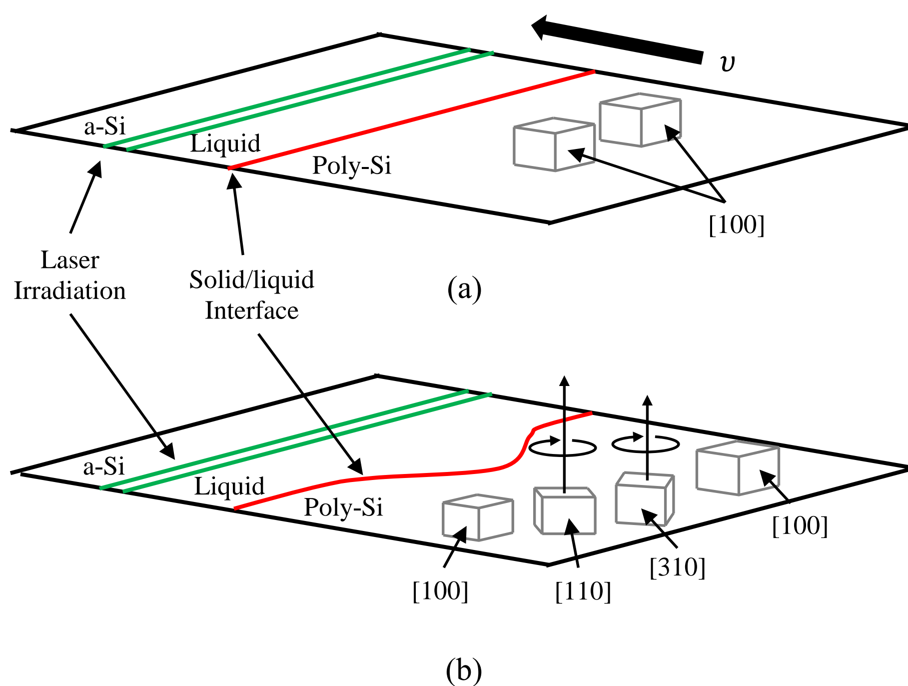

Figure 2.22: Illustration of (a) straight (b) concaved liquid/solid interface formed at different CLC laser power. Preferred <100> growth in SD induced only when the solid/liquid interface is perpendicular to the laser scan direction.

in the direction of laser scan. Those planes are rotated at deviated angles of 18.4°, 26.6°, 45.0° and 33.4° respectively with respect to the (010) SD plane.

In the concave solid/liquid region, supercooling is higher at a position with further distance between the solid/liquid interface and just-irradiated region. In this region, Rg becomes larger than laser scan speed υ because Rg increases proportionally to supercooling according to Wilson-Frenkel law. This higher Rg as well tend to induce intra-grain defects such as sub-GBs. Those sub-GBs were seen in the GMA 2°-65° with CLC at higher power than the optimal condition. No specific orientation orders were observed when comparing the upper concave part (region I) and lower concave part (region II) since the supercooling was averaged along the trailing solid/liquid interface. Further increase in laser power yielded narrower domains as well as inducing more sub-GBs in the domains. The evolution of the silicon growth orientation in laser scan direction with respect to the varying laser power were also observed for the CLC under 125 nm and 140 nm C/L thicknesses. The optimum laser power for the stable

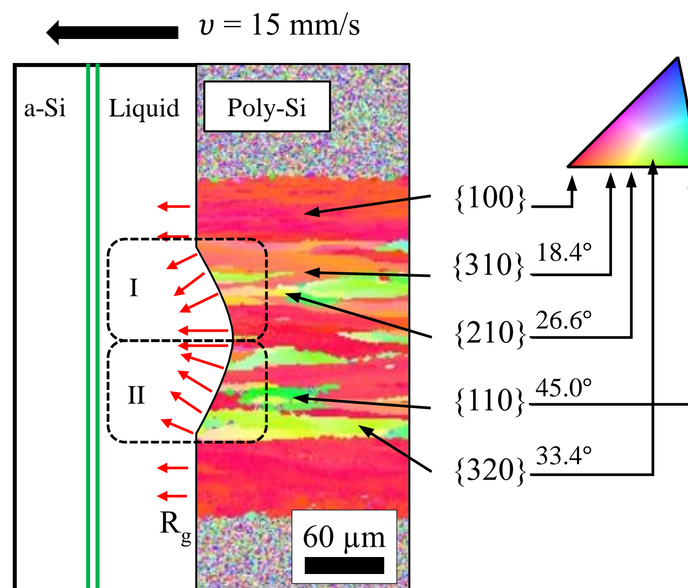

Figure 2.23: IPF SD image of 2.2 W CLC together with the solid/liquid interface illustration. Orientations and respected angles of silicon domains in SD are also shown. Red arrows indicate the crystal growth in <100> direction with growth rate R_g. Black thick arrow shows laser scan direction with scan speed *v* = 15 mm/s.

growth was different for each case owing to the C/L behaviors. Similarly, the GB formation in the center of the laser scan region with slightly increased laser power than the optimum were also observed in these cases. This confirmed that the change in the temperature flux on the sample induced the GB formation.

2.5 Summary

Crystallization by a Gaussian line beam was successfully done to transform the a-Si precursor film into poly-Si film with high percentage of {100} surface orientation owing to low interfacial energy between the {100} silicon plane with the quartz substrate. The incorporation of SiO_2 C/L promotes the lateral growth of the domain by acting as a heat reservoir to lengthen the melting time of the liquid silicon and avert vertical growth of the seeded domain. The difference in thermal expansion coefficient between silicon film and quartz substrate results to the induced tensile stress on poly-Si film as analyzed by Raman spectroscopy with the low frequency peak shift ($\Delta\omega$) of 2.8 cm^{-1} from the model for c-Si was seen. The value is consistent with the calculated $\Delta\omega$ of 2.75 cm^{-1} by considering the residual thermal stress in the film.

Crystallographic observation and analysis from a broad range of equipment namely EBSD, Raman spectroscopy and STEM altogether confirmed the growth evolution of poly-Si crystallized at different laser power with the initial formation of nc-Si coexisting with uncrystallized a-Si, followed by long grains formation and the occurrence of the so-called amorphization on the surface of the film with higher power CLC. It was observed that even though a wide CLC power windows for the formation of (100)-oriented grains are existed, there are still a narrow laser power selection for the formation of GB-free silicon film. It is concluded that the non-planar solid/liquid frontal interface culminated by the nature of the Gaussian line beam profile at high laser power has deviated the growth direction of {100} plane

from SD resulting in the formation of grain boundaries at the center area of the laser scan region. Thus, controlling the stability of the heat flux on solid/liquid frontal is crucial in controlling the in-plane growth direction of the high growth rate {100} silicon plane to minimize the GB formation.

2.6 References

1. T. T. Nguyen and S. I. Kuroki, Jpn. J. Appl. Phys. **58**, SBBJ08 (2019).

2. N. Sasaki, M. Arif, and Y. Uraoka, Jpn. J. Appl. Phys. **58**, SBBJ02 (2019).

3. R. Vikas, R. Ishihara, Y. Hiroshima, D. Abe, S. Inoue, T. Shimoda, J. W. Metselaar, and C. I. M. Beenakker, Tech. Dig. - Int. Electron Devices Meet. IEDM **2005**, 919 (2005).

4. Y. S. Li, C. Y. Wu, C. H. Chou, C. Y. Liao, K. C. Chuang, J. D. Luo, W. S. Li, and H. C. Cheng, Jpn. J. Appl. Phys. **57**, 06KB06 (2018).

5. R. Vikas, R. Ishihara, Y. Hiroshima, D. Abe, S. Inoue, T. Shimoda, W. Metselaar, and K. Beenakker, Japanese J. Appl. Physics, Part 1 Regul. Pap. Short Notes Rev. Pap. **45**, 4340 (2006).

6. W. Zhu, G. Zheng, S. Cao, and H. He, Sci. Rep. **8**, 10537 (2018).

7. S. Moon, M. Hatano, M. Lee, and C. P. Grigoropoulos, Int. J. Heat Mass Transf. **45**, 2439 (2002).

8. W. Yeh and M. Matsumura, Japanese J. Appl. Physics, Part 1 Regul. Pap. Short Notes Rev. Pap. **41**, 1909 (2002).

9. P. I. Gaiduk, S. L. Prakopyeu, V. a. Zajkov, G. D. Ivlev, and E. I. Gatskevich, Phys. B Condens. Matter **404**, 4708 (2009).

10. S. Fujii, S. I. Kuroki, M. Numata, K. Kotani, and T. Ito, Jpn. J. Appl. Phys. **48**, 04C129 (2009).

11. M. Chahal, Dr. Thesis, Columbia Univ. (2012).

12. D. P. Gosain, A. Machida, T. Fujino, Y. Hitsuda, K. Nakano, and J. Sato, Japanese J. Appl. Physics, Part 2 Lett. **42**, L 135 (2003).

13. H. I. Smith, C. V. Thompson, M. W. Geis, R. A. Lemons, and M. A. Bosch, J. Electrochem. Soc. **130**, 2050 (1983).

14. M. W. Geis, H. I. Smith, B. -Y. Tsaur, J. C. C. Fan, D. J. Silversmith, and R. W.

Mountain, J. Electrochem. Soc. **129**, 2812 (1982).

15. Y. Wang, M. D. Chahal, J. J. Wang, A. B. Limanov, A. M. Chitu, and J. S. Im, Mater. Res. Soc. Symp. Proc. **1770**, 55 (2015).

16. J. Jin, Z. Yuan, L. Huang, S. Chen, W. Shi, Z. Cao, and Q. Lou, Appl. Surf. Sci. **256**, 3453 (2010).

17. P. C. Van Der Wilt, B. D. Van Dijk, G. J. Bertens, R. Ishihara, and C. I. M. Beenakker, Appl. Phys. Lett. **79**, 1819 (2001).

18. S. P. Huang, H. C. Chen, P. H. Chen, Y. Z. Zheng, A. K. Chu, Y. S. Shih, Y. X. Wang, C. C. Wu, Y. A. Chen, P. J. Sun, H. C. Huang, W. C. Lai, and T. C. Chang, IEEE Trans. Electron Devices **67**, 3163 (2020).

19. M. M. Billah, A. B. Siddik, J. Bae Kim, L. Zhao, S. Y. Choi, D. K. Yim, and J. Jang, IEEE J. Electron Devices Soc. **7**, 503 (2019).

20. J. S. Im and H. J. Kim, Appl. Phys. Lett. **64**, 2303 (1994).

21. C. H. Chou, I. C. Lee, P. Y. Yang, M. J. Hu, C. L. Wang, C. Y. Wu, Y. S. Chien, K. Y. Wang, and H. C. Cheng, Appl. Phys. Lett. **103**, 053515 (2013).

22. S. Fujii, S. I. Kuroki, X. Zhu, M. Numata, K. Kotani, and T. Ito, Jpn. J. Appl. Phys. **47**, 3046 (2008).

23. K. Kitahara and A. Hara, Cryst. - Sci. Technol. (2012).

24. K. Kitahara, R. Yamazaki, T. Kurosawa, K. Nakajima, and A. Moritani, Japanese J. Appl. Physics, Part 1 Regul. Pap. Short Notes Rev. Pap. **41**, 5055 (2002).

25. K. Kitahara, T. Ishii, J. Suzuki, T. Bessyo, and N. Watanabe, Int. J. Spectrosc. **2011**, 632139 (2011).

26. H. Richter, Z. P. Wang, and L. Ley, Solid State Commun. **39**, 625 (1981).

27. Z. Iqbal, S. Vepřek, A. P. Webb, and P. Capezzuto, Solid State Commun. **37**, 993 (1981).

28. G. S. Ganot, Dr. Thesis, Columbia Univ. (2012).

CHAPTER 3:

Extension of {100}-Oriented Grain Boundary-Free Silicon Film by CLC

It is regarded that the use of a Gaussian profile line beam is sensitive to control the irradiated heat flux on the sample surface during CLC thus easily alter the planar solid/liquid frontal interface during the crystallization which resulted to the formation of GBs. A uniform beam profile is expected to overcome this hitch thus the use of a flat-top beam was proposed. Additionally, it was also reported that the use a gradual temperature slope in the direction of the crystal growth can helps in producing elongated grain from the laser crystallization. The advantages of these properties were taken into consideration in order to stably grow silicon film from a-Si precursor with melt-mediated crystallization.

3.1 Effect of silicon interface energy on domain growth

Preferred {100}-oriented silicon grains in surface normal direction conquered the film's surface texture upon crystallization by CLC on an insulated quartz substrate as discussed in. the previous chapter. This condition was met regardless of some manipulated variables including the incorporation of C/L with varying thicknesses as well as crystallization at varying laser power. Occupancy of grain orientation within <100> in ND reaching 99% in the full melt

crystallization region under the CLC optimized conditions were also shown. This high occupancy percentage is attributed to the favorable silicon growth in <100> ND direction due to the {100} silicon plane's lowest energy for the case of silicon/quartz interface and this occurrence worth an extended explanations from reported experiments to strengthen the claim [1].

Being a most popular material in semiconductor technology made silicon as one of the most extensively investigated material. Theoretical calculation on the Si/SiO_2 interfacial energy are less extensive and less conclusive than the experimental attempts due to a serious obstacle of the complexity of the atomic arrangements in the vicinity of the interface as the crystallographic surface of silicon and an amorphous SiO_2 or quartz substrate may not be precisely smooth and exactly stoichiometric. Some experimental works however are successful in determining the relative difference in the interfacial energies for different silicon orientations, especially related to {100}, {110}, and {111} planes. Specifically, the hierarchical of interface energy was investigated by analyzing the evolution of crystal orientation with multiple laser scan on a-Si/SiO_2 sample [2,3].

The survivability of a specific orientation upon multiple number of laser scans determined the anisotropic nature of Si/SiO_2 interfacial energy. The grains with lower Si/SiO_2 interfacial energy grows at the expense of the grains with higher interfacial energy so least interfacial energy grains are dominant even only after the first scan. Additionally, the orientation with lower interfacial energy grows at a faster rate while melts at a slower rate. With that being said, by applying multiple laser scans one can determine the hierarchy of the orientation's interfacial energy by analyzing the survivability in term of the rate at which the orientation expands or shrink. Figure 3.1 shows the occupancy of different oriented silicon grains in surface normal direction as a function of CW laser scan number(s). The plot was reported by M. Chahal, Dr. Thesis, Columbia Univ. (2012)[4]. From Chahal's experimental

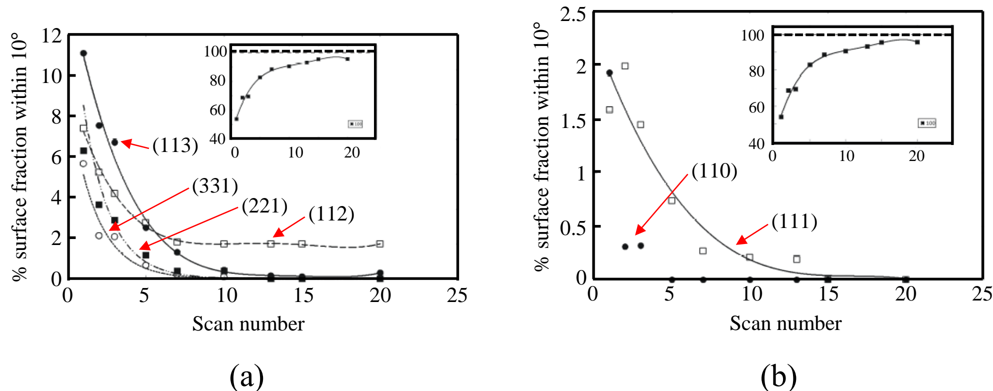

Figure 3.1: Plot of silicon grain orientation fraction number within 10° in surface direction as a function of CW laser scan number(s). The insets show the plot for <100> surface direction. After M. Chahal, Dr. Thesis, Columbia Univ. (2012).

results, the growth of silicon in <100> reached 50% in the first laser scan and grows as the number of scans increases. At the same time, the occupancy of non-{100} counterparts decayed as a function of laser scan numbers. The hierarchical order of Si/SiO_2 interfacial energies, σ as a function of grain orientation then summarized as:

$$\sigma_{\{100\}} < \sigma_{\{211\}} < \sigma_{\{311\}} < [\sigma_{\{221\}}, \sigma_{\{331\}}] < \sigma_{\{111\}} < \sigma_{\{110\}}.$$

The same behavior was also seen for the multi-scan crystallization under the C/L where preferred {100} ND growth boosted; however, the lateral-grown poly-Si from the first scan tend to cultivate the GBs in the process thus transform the elongated domain into granular grains [5]. The use of appropriate dwell time of 0.53 ms in the radiative-heating (results in Chapter 2 – see Figure 2.11) allows the rearrangement of the atoms in a manner to reduce the formation of less-favorably-oriented neighboring domain even with a single laser scan. Increasing the laser power for capped silicon induces portions of non-{100} ND grains following the orders of the Si/SiO_2 interface energy reported by Chahal [1,4].

3.2 Achieving stable temperature profile with laser beam tuning

It was discussed in Chapter 2 that the preferred <100> in-plane growth are achievable given that the stable liquid/solid front of the irradiated film is retained. By accommodating a Gaussian profile line beam, a flat temperature profile along the line beam was attained with an optimum laser power which then offer the planar isotherm in the silicon film. In order to maximize the width and perhaps to minimize the laser power dependency of the planar heat flux in the direction of the laser beam long axis, the use of a flat-top laser beam profile is the best approach. First thing first, the dependency of the laser oscillation in the laser head when changing the irradiated laser power must be minimized as the stability of the output might fluctuate. The use of external components to control the laser power is a good way to achieve such output stability. Specifically, the use of half-lambda ($\lambda/2$) plate together with a beam splitter help to attenuate the output laser power keeping the laser power fluctuation from the laser head to be minimal.

Polarization separation of the beam is also manifested by the use of those components. Additionally, incorporation of a quarter-lambda ($\lambda/4$) plate helps to transform the linear polarized beam into a circular polarization. This is to eliminate any effect of the beam polarization on the CLC process even though minimal to no effect was observed. Figure 3.2 shows the CLC set up with installed $\lambda/2$ plate, $\lambda/4$ plate and beam splitter. With the original purpose of the DOE for transforming the Gaussian beam in to a flat-top beam, a well align and well-placed DOE and focusing lens will enable such advantage to be utilized. Figure 3.3 illustrates the beam shape formation with in-focus and out-of-focus condition formed when the beam pass through the DOE provided that the original Gaussian beam has a beam diameter of 2.25 mm measured at I_0/e^2. The focus point of the DOE is marked as position III form Figure 3.3. With 2.25 mm diameter of incoming beam, a top flat in the long axis formed at the focus

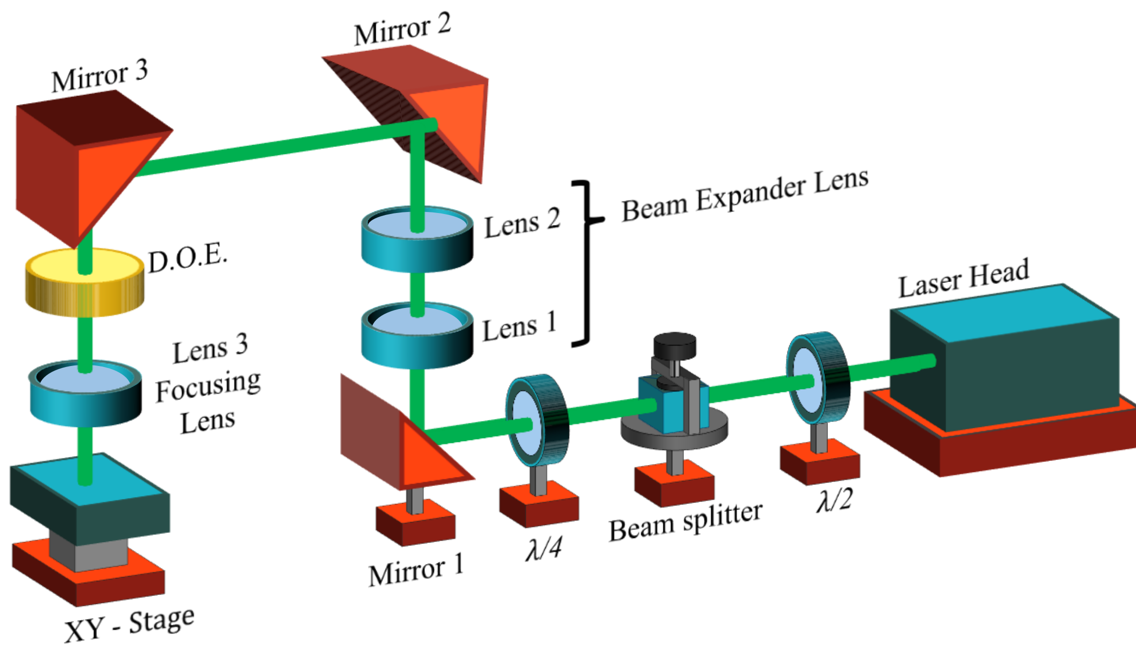

Figure 3.2: Laser system set up with installed λ/2 plate, λ/4 plate and beam splitter.

point (III) and beam profiles at out-of-focus positions are marked as I, II, IV and V. A rounded-top beam formed at position I and II while M-shaped beam formed at position IV and V.

The versatility of the diffractive optical element (DOE) not only restricted the beam profile adjustment in the long axis but also in the short axis. This enables more control of the laser beam profile in the laser scan direction which can lead to enhancement of the crystal quality in CLC [6]. Changing the incoming beam diameter to a value smaller than 2.25 mm by the beam expander will shift the output beam profile as illustrated in Figure 3.3. In this condition, the flat-top long axis profile shifted to a position further from focus point but keeping the profile in the short axis unchanged. This adjustment allows a wider short axis beam to be utilized for the CLC process. The Gaussian profile line beam with dimension of 470 μm × 8 μm (Chapter 2) was transformed into a rectangular beam with dimension of 460 μm × 35 μm for laser crystallization by utilizing the versatility of the DOE.

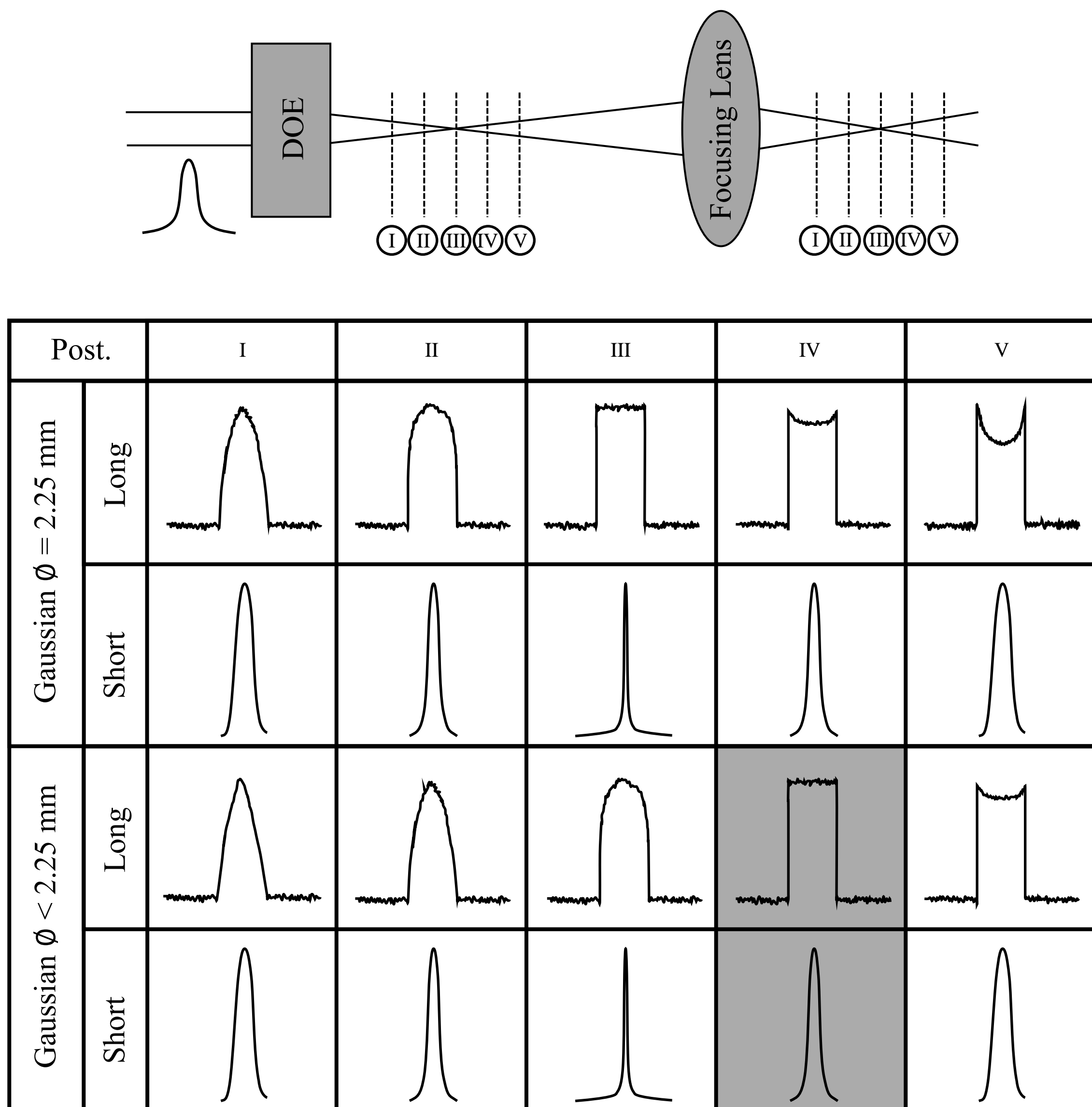

Figure 3.3: Beam profile formed after Gaussian beam pass through the diffractive optical element (DOE). Illustration on the top shows the DOE and focusing lens arrangement as well as the positions for the beam profile observation marked with I,II,III,IV and V. Position III is the focus point where highest intensity measured. Table at the bottom shows the illustration of normalized long axis and short axis beam profiles formed at each position when the original Gaussian beam has a diameter of 2.25 mm and smaller than 2.25 mm.

3.3 Characterization of well-oriented silicon film

Laser crystallization using flat-top beam profile is beneficial in keeping the uniform heat flux on the irradiated region to ensure stable growth of the silicon grains. It was also reported that crystallization with elongated gaussian beam in the direction of the laser scan can enhance the lateral growth of the silicon grains as the gradual temperature slope which leads to gradual cooling will suppress the creation of new nucleus and thus enhances the growth of the crystal domains.

3.3.1 Stable growth of {100} oriented grains

The combination of aiding parameters of flat-top long axis and wider-Gaussian short axis beam indicated by the grey shaded regions from Figure 3.3 which expected to elongated the crystal domains was made possible with the adjustability of the beam profile by the DOE and other optical components in the laser set up. Figure 3.4 shows the OM image of a laser trace together with the corresponding IPF ND, SD, TD, and GMA 2°-65° for the CLC at 3.3 W under 133 nm C/L with scan speed of 15 mm/s. A rectangular beam with flat-top profile in long axis and Gaussian profile in short axis having a dimension of 460 μm × 35 μm was used in the CLC where the laser scan direction was perpendicular to the beam's long axis. As expected, the silicon orientation in ND is dominated by the preferred {100} orientation following the thermodynamic of interfacial energy between the Si/SiO_2 interface. As for the in-plane growth, grains with random orientations were generated but fast growth rate of {100} oriented plane ensures the survivability towards the end of the laser scan. As can be seen from IPF SD and GMA 15°-65° mappings, when the translational speed of the stage reaching the set 15 mm/s mark, the randomly nucleated grain widens in from ~35 μm to ~120 μm and occluded other oriented grains in the process while maintaining the $(0\bar{1}0)$ growth in SD. The width of this {100}-oriented grain monotonically increases with laser scan and almost saturates after

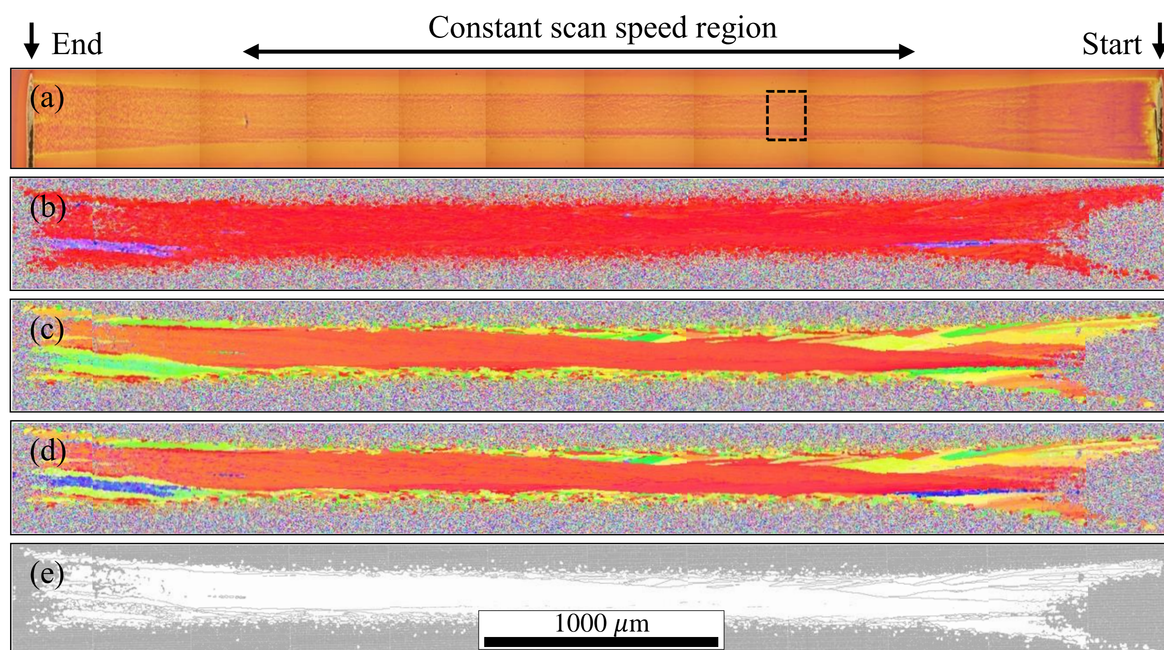

Figure 3.4: Laser scan trace crystallized at 3.3 W under 133 nm C/L at 15 mm/s represented as (a) optical micrograph, (b) IPF ND, (c) IPF SD, (d) IPF TD, and (e) GMA 15°-65. Arrows on top right and top left side show the start and end point of the laser scan, respectively. Squared region in (a) is the region for further analysis.

~300 μm scan travel in the constant speed region. Stable and fast growth rate of {100} oriented crystal plane ensures the dominance of the <100> lateral growth in both SD and TD directions with maintained orientation within 10°. A long grain boundary (GB) free domain with preferred {100}-orientation was stably grown near the vicinity of the start point extending to more than 4 mm in length all the way to the end of the laser scan region.

Figure 3.5 shows the IPF SD and GMA 15°-65° mapping for the CLC region with slightly high laser power of 3.4 W. A large {100}-oriented grain boundary free crystal domain was realized but it takes a longer scan travel of ~1200 μm for this domain to expand to its maximum width. Initially, randomly oriented grains generated near the start point behave in a similar manner as CLC with Gaussian profile in beam's long axis. Slightly higher effective energy at the center rotated the {100} growth towards the center of the scan trace which resulted in the convergence of the crystal domains from both sides of the scan trace. The growth

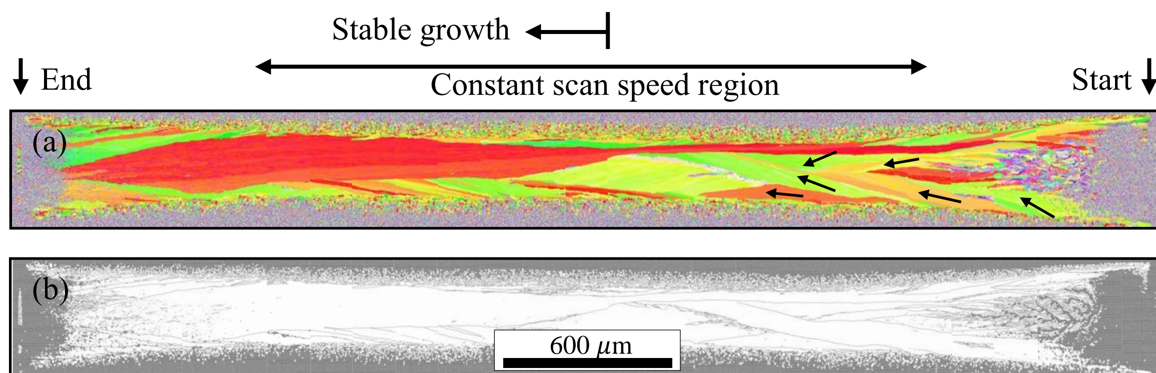

Figure 3.5: Laser scan trace crystallized at 3.4 W under 133 nm C/L at 15 mm/s represented as (a) IPF SD and (b) GMA 15°-65 mappings from EBSD.

of the $(0\bar{1}0)$ SD grain near the side region with lower effective energy made the grain to stably grows as the scan sweeps across the sample. This $(0\bar{1}0)$ SD survived with lateral growth owing to the high {100}-plane growth rate which then expanded perpendicularly towards the center of the scan; about 1200 µm after the constant speed was achieved. A distinct transition between lateral growth at the center region and granular growth at the peripheral of the lateral growth region can be seen with the utilization of the flat-top beam profile which is different to the Gaussian profile's case as discussed in Chapter 2. This is due to the fact that the gradient of the heat flux at the side region is more gradual for the former compared to a sudden heat flux drop in the latter case.

Figure 3.6 shows the number fraction of grains having an in-plane orientation within 10° growing in the direction of <100>, <210>, <310> and <320> with respect to SD obtained by CLC with varying laser power from 3.1 W to 3.5 W. Figure 3.6(a) shows the number fraction taken 600 µm away from the start point where constant scan speed was just achieved. High number fraction of the preferred {100} SD grains was obtained with CLC laser power of 3.1 W which was lower than the optimized power of 3.3 W; resulted by the high effective power in the beam's accelerating region (low speed). In the constant scan speed region however, the preferred $(0\bar{1}0)$ SD grains could not retain the stability of the growth due to reduced effective

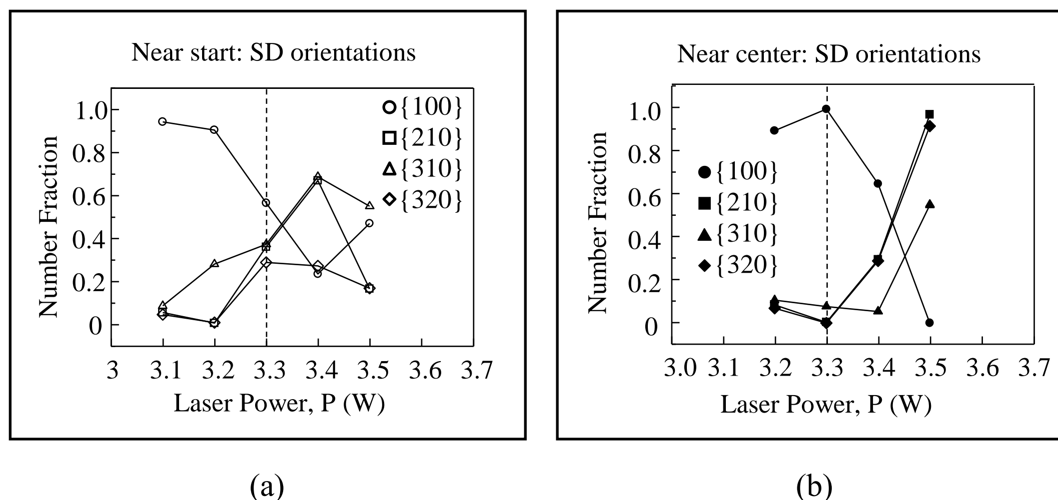

(a) (b)

Figure 3.6: Number fraction of grain having in-plane orientation of {100}, {210}, {310} and {320} in SD with varying laser power (a) at a point where set speed just attained and (b) after the laser beam sweep to more than 3000 µm after constant scan speed was gained. The vertical dotted lines indicate the optimum laser power for the particular condition.

power thus reduction in the number fraction of {100} was observed. Consequently, lateral growth of silicon domain vanished as the laser beam travels in the case of 3.1 W. On the other hand, the $(0\bar{1}0)$ SD grain continues to travel and expand under the optimized condition which in this particular case using 3.3 W laser power as shown in Figure 3.4. This resulted in 99.4% of the in-plane plane to be in the preferred {100} orientation. Figure 3.6(b) shows the number fraction of four planes crystallized at 3.1 W to 3.5 W laser power observed at the center of the laser trace about 3000 µm after the constant laser scan speed was attained. Beyond the optimum laser power, the number fraction of the preferred {100} orientation in SD significantly reduced as the $(0\bar{1}0)$ SD plane growth direction was rotated following the modified, non-planar solid/liquid frontal as discussed in Chapter 2. These rotated grains induced GB formation but in a more subtle manner where individual grain with more than tens of micrometers wide were retained and less likely to have sub-GBs, opposing to the CLC with Gaussian line beam. Stable growth of silicon film by CLC was realized by the beam spot modification where the {100} domain length extended to more than 4000 µm long was observed.

3.3.2 Surface morphology

A very long GB-free silicon domain with the preferred {100}-orientation was successfully grown by improving the laser system in general and specifically, a modification on the beam profile for the CLC process. Unlike a smooth surface obtained on the laser trace by using Gaussian's profile line beam for the CLC (Figure 2.10(b)), there are apparent periodic patterns formed on the surface during the growth of the elongated grains. Figure 3.7 shows the OM picture (Figure 3.7(a)) and an IPF SD masked with GMA 2°-65° from EBSD (Figure 3.7(b)) taken at the center of the scan trace of the 133 nm capped sample scanned at 3.3 W (squared region in Figure 3.4(a)). Two large clusters of parallel lines formed on the upper and lower region of the scan width with an angle of 3.9° and 8.6° deviated from $(0\bar{1}0)$ SD, respectively. Inside these clusters, formation of small angle GB is minimal as analyzed by the

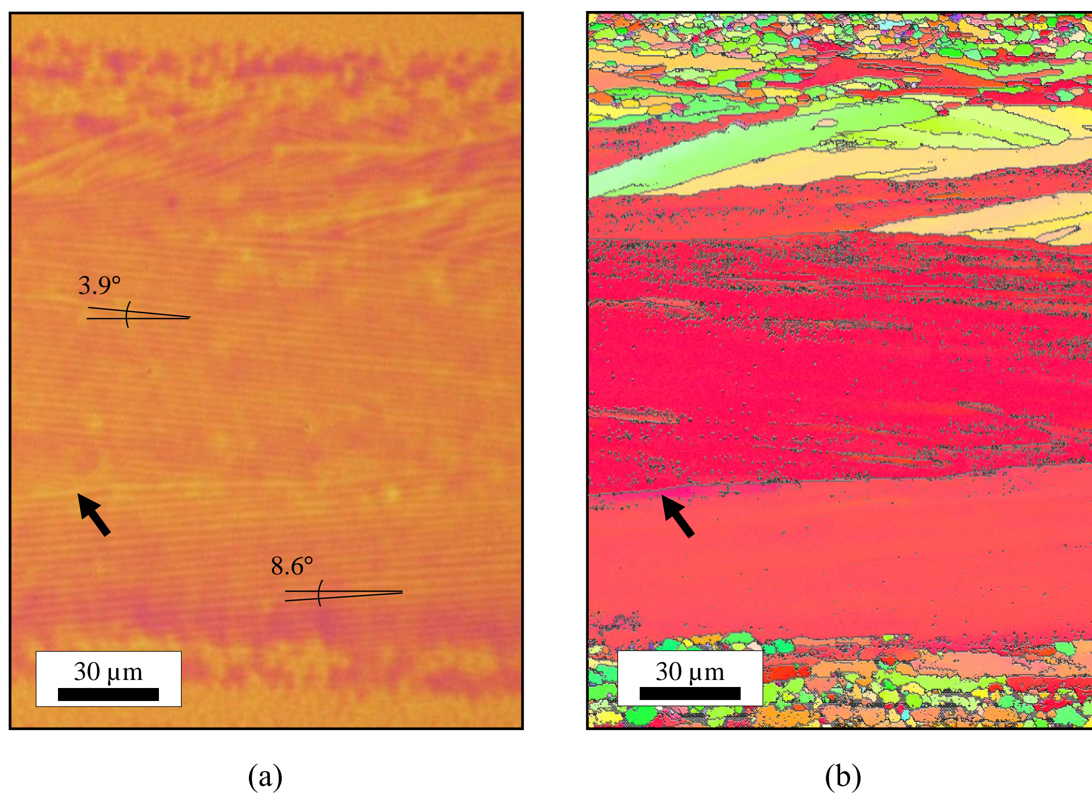

Figure 3.7: Laser scan region captured by (a) optical microscope and (b) IPF SD masked with GMA 2°-65° from EBSD. The magnified images are extracted from squared region in Figure 3.4(a). Laser scan direction is from right to left.

GMA 2°-65° mapping; which suggests that a cluster of parallel lines is corresponded to a single grain of silicon [7]. The intersection of the two clusters made up a low angle grain boundary <15° observed as bright lines as marked with black arrow from the OM picture. The parallel lines in a cluster (single silicon domain) which also referred as "columnar" structure horizontally grow in the direction perpendicular to the solid/liquid front during the crystallization process [8].

Figure 3.8(a) shows the surface morphology of the similar columnar pattern formed by the CLC on the full-melt crystallized region. The AFM topographic imaging was done after the removal of the C/L layer which was deposited prior to the CLC (125 nm C/L, 4.2 W, 12 mm/s) process. The cross-section profile of the columnar structure across the grey shaded

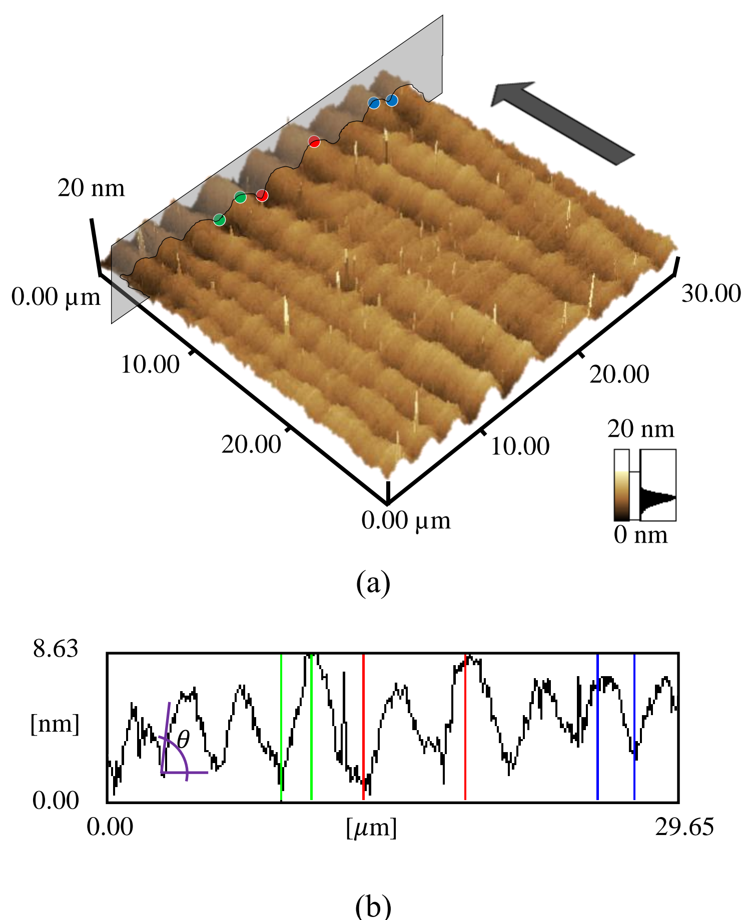

Figure 3.8: Cellular growth structure obtained by AFM shown in (a) 3-dimensional representation and (b) cross-section of the structure at region marked with grey region from (a). Thick arrow in (a) indicates the laser scan direction.

region in Figure 3.8(a) is shown in Figure 3.8(b). Peak to valley height of the columnar pattern averaged at 7 nm throughout multiple samples with similar columnar patterns. The peak-to-peak or valley-to-valley distance on the other hand varies (2 ~ 5 μm) between traces with different CLC parameters; the frequency of the columnar patterns tends to increase with increasing effective energy absorbed by the film, which also means the peak-to-peak distance reduce with increasing energy. This relation is identical to the experimental and theoretical results obtained with the melt-mediated crystallization reported by C. Grigoropoulos et al., Phys. Rev. B - Condens. Matter Mater. Phys. **73**, (2006) where the wavelength of the observed columnar structure decreases with increasing substrate temperature [9]. The groove that alternates the columnar structure possesses an average incline angle (marked as θ from Figure 3.8(b)) of 0.57° with respect to the planar surface of the film. These irregularities on the surface however, did not induce in-plane grain boundary which easily generated with the association of surface tension.

With increasing laser power for CLC exceeding the window for steady growth of the silicon film, a more chaotic cellular structure was observed; resembling the out-of-equilibrium

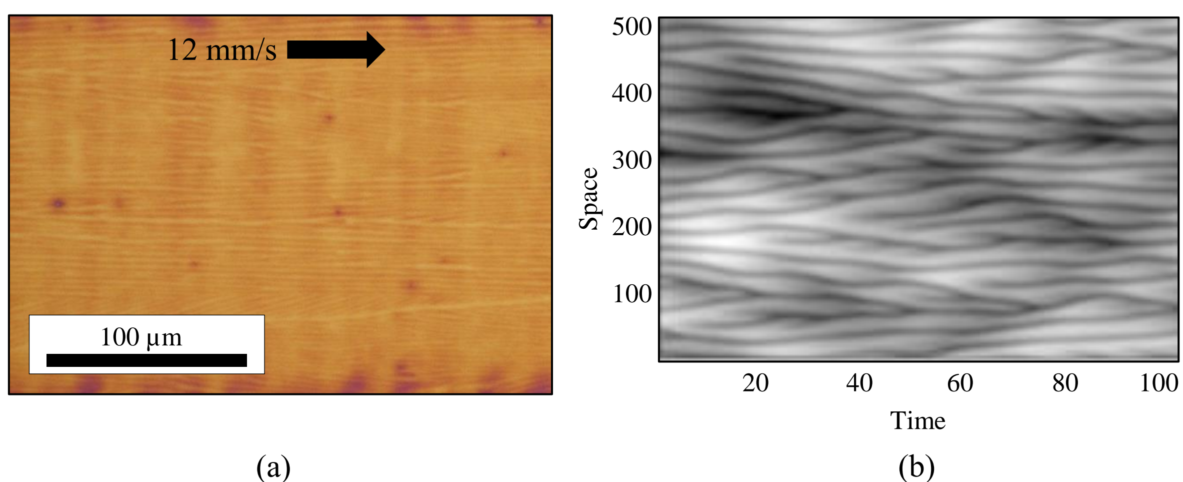

Figure 3.9: Chaotic cellular structures (a) observe by OM on CLC region and (b) example of spatiotemporal diagram resulted by evolution of perturbed frontal shape obtained by solving the nonlinear KS equation reported by C. Grigoropoulos et al., Phys. Rev. B - Condens. Matter Mater. Phys. 73**, (2006).**

spatiotemporal chaos obtained by solving a well-known Kuramoto-Sivashinsky (KS) nonlinear partial differential equation [10]. Figure 3.9 shows an OM image with a chaotic cellular structure observed on the silicon surface after crystallization with CLC (125 nm C/L, 4.5 W, 12 mm/s) condition deviated from the optimized steady state growth. Figure 3.9(b) shows an example of a spatiotemporal diagram described by the evolution of nonstable solid/liquid frontal structure obtained by C. Grigoropoulos et al. by solving the KS equation [9]. In this CLC experiment, the degree of the chaos increases at further higher laser power which often associated with laser ablation on the film. Such columnar growth by CLC enables an instant glimpse on the growth direction of the crystal domain as well as in-plane grain boundary generation at the intersection of the clusters of parallel columnar patterns.

3.3.2 In-plane orientation

Lattice structure and diffraction pattern observation was carried out on the elongated crystal domain to study the crystallinity as well as the orientation of the film. To meet this purpose, high resolution transmission electron microscopy (HRTEM) observation was carried out in the region with parallel columnar structure growing in the direction of the laser scan.

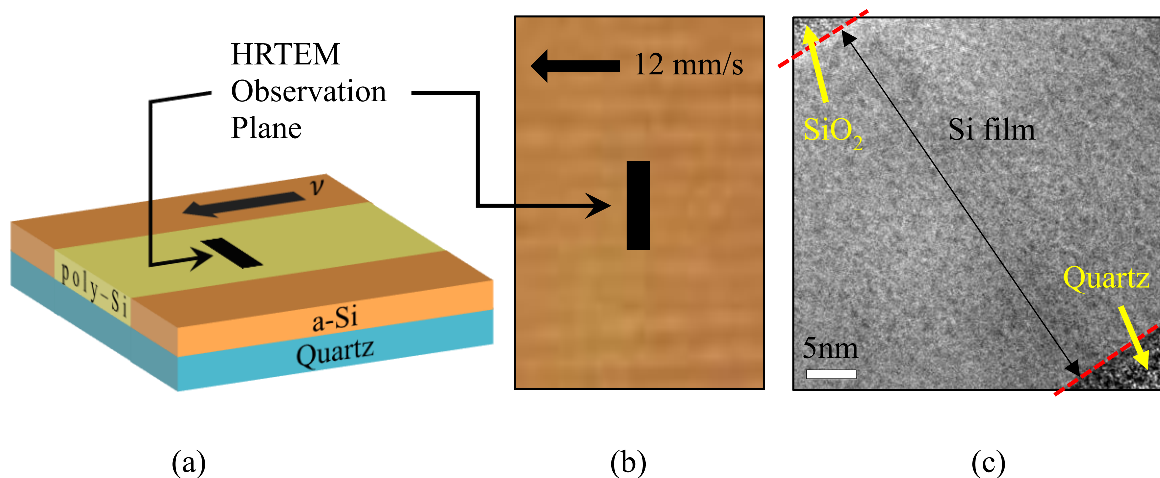

Figure 3.10: Sample used for TEM analysis showing (a) an illustration of specimen pick-up position and (b) the OM image indicating TEM observation plane which was perpendicular to the growth direction of columnar structures. Low magnification TEM cross section image in (c) shows that the silicon film was crystallized throughout the film thickness.

Figure 3.10(a) and (b) shows the illustration and OM image of the laser scanned region selected for the TEM observation, respectively. A 20 µm × 3 µm specimen was picked up by FIB and thinned in the short axis before the observation. The specimen was selected with the long axis plane specified to be perpendicular to the direction of the laser scan and also perpendicular to the growth direction of the columnar structure as represented by the black rectangular box in Figure 3.10(b). A clear crystalline silicon layer is observed from the low magnification TEM image shown in Figure 3.10(c) with the crystallized silicon film sandwiched between top SiO_2 layer and the underneath quartz substrate. Furthermore, the silicon film was fully crystallized with a single lattice structure throughout the thickness.

As previously mentioned, the surface plane of the TEM image is the plane of the silicon domain facing in the direction of the laser scan and this plane are supposed to be in {100} SD direction as expected by EBSD analysis. Fundamentally, a silicon growing in <100> direction possess two major planes of {100} and {110} planes perpendicular to the surface plane. Figure 3.11(a) and (b) shows the illustration of silicon's diamond cubic crystal structure with drawn (100) and (110) planes, respectively. Viewing from <$\bar{1}$00>, the shortest interplanar spacings in <100> and <110> directions are d_{400} = 1.36 Å and d_{220} = 1.92 Å respectively. At high TEM magnification, a clear arrangement of lattice structure on the specimen was observed as shown in Figure 3.11(c); the associated image with 2 million times magnification in inset (i) distinctly shows the representation of the atomic structure having a characteristic {100} surface plane with the corresponding FFT image analyzed by ImageJ software shown in (ii). Measured lattice spacings from the FFT are 0.13 nm and 0.19 nm, representing the primary (400) and (220) silicon planes, respectively.

Similarly, the selected area electron diffraction (SAED) pattern directly extracted from the TEM shows the diffraction pattern representing the {100} plane with reciprocal lattice points in the <110> and <100> directions were highly contrasted in dark-field image as shown

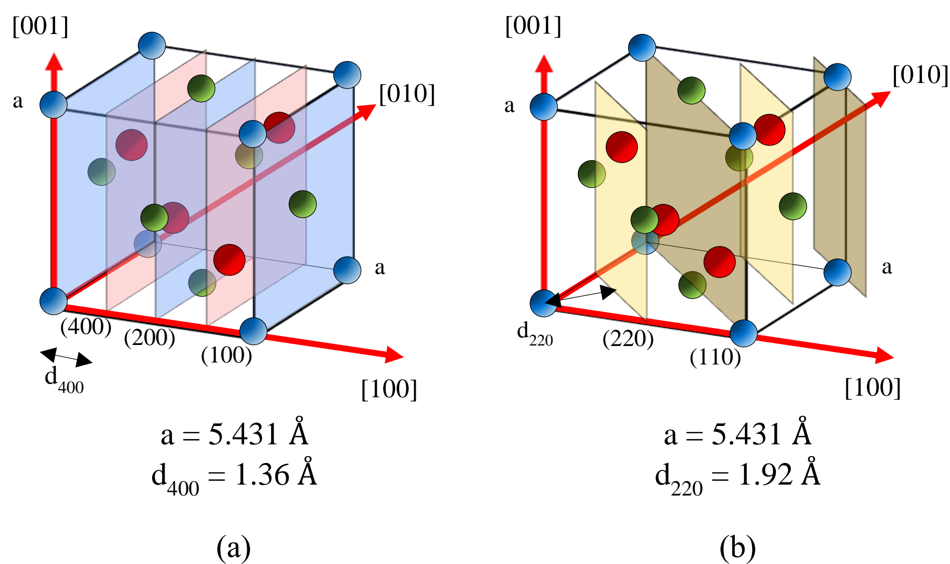

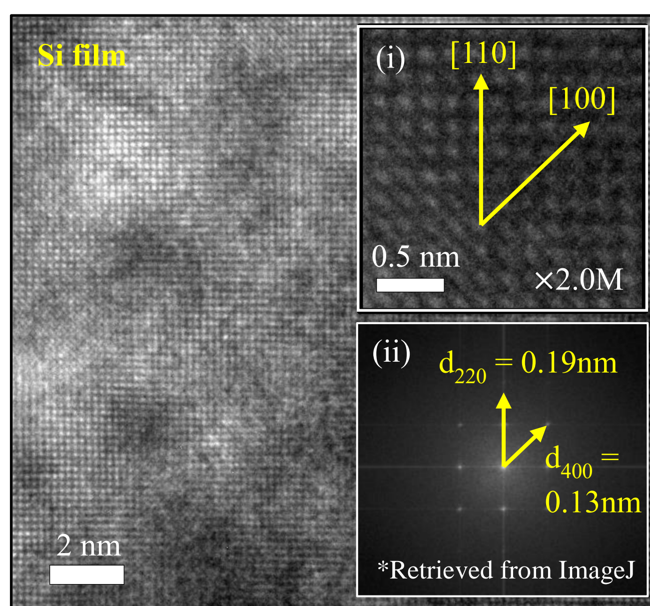

(c)

Figure 3.11: Schematics of diamond lattice structure (a) with drawn (400), (200) and (100) planes and (b) with drawn (220) and (110) planes. Shortest interplane spacing of d_{400} and d_{220} also shown. Lattice image by TEM of the crystallized film is shown in (c) with inset (i) showing higher magnification image and inset (ii) showing FFT image with measured plane spacing.

in Figure 3.12(a). For reference, the reciprocal lattice points for (100) plane diamond structure is shown in (b) with the ratio of two shortest reciprocal points gives a value of 1.414. The average value measured from SAED was 1.413 which confirmed the analyzed specimen to

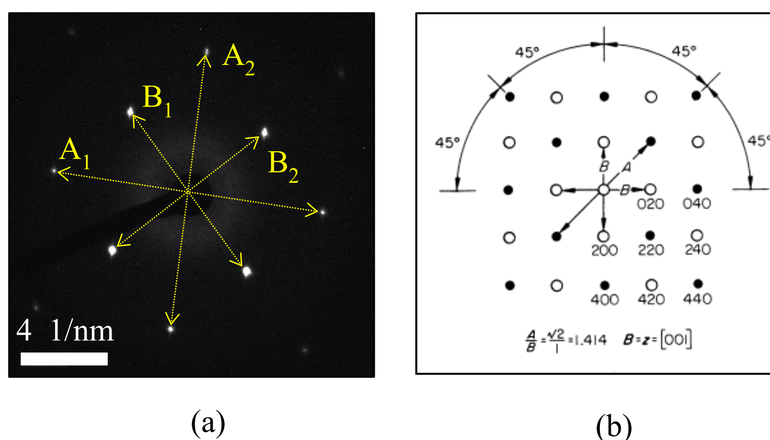

(a) (b)

Figure 3.12: (a) SAED pattern retrieved from HRTEM representing silicon (100) plane. Ratio of (220) plane to (200) plane of 1.413 measured from SAED agrees with the characteristic (100) plane of diamond lattice structure shown in (b) with the ratio of 1.414.

have a characteristic of {100}-oriented plane facing the growth direction. The average value was considered due to the nonsymmetric of the reciprocal lattice points from SAED which were likely arose from a slight beam offset with respect to the zone axis during TEM observation. The {100} oriented plane extend throughout the specimen length as evidenced by similar SAED patterns observed along the specimen at three different observation sites marked with P-1, P-2 and P-3 as shown in Figure 3.13(a). The SAED patterns extracted at the corresponding positions are shown in Figure 3.13(b), (c) and (d), respectively. From the TEM lattice observation and SAED pattern analysis, the growth of the silicon domain with in-plane orientation in SD having the {100} characteristics are in agreement with the IPF SD mappings from EBSD.

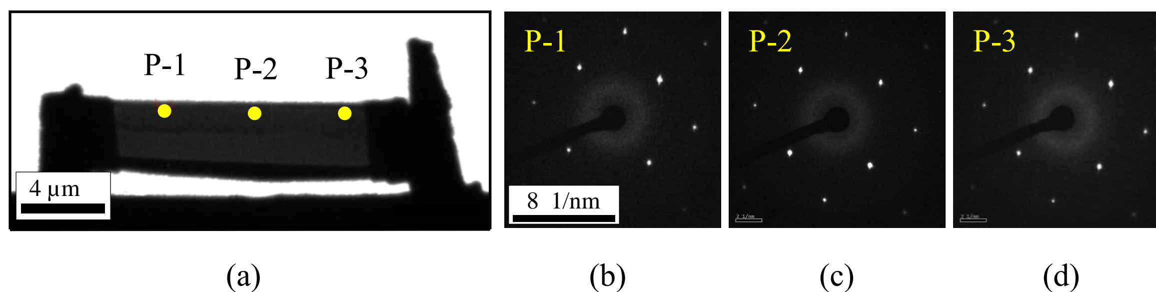

(a) (b) (c) (d)

Figure 3.13: (a) Three different SAED extraction site on one specimen marked with P-1, P-2, and P-3. The corresponding SAED patterns are shown in (b), (c), and (d) respectively.

Additionally, in-plane X-ray diffraction (XRD) analyis also evidenced the preferred {100} growth with strong diffration peaks appeared on the spectrum as shown in Figure 3.14. With the CuK_α radiation used as the X-ray source with λ=1.5406 Å, two distinct peaks emerged at the characteristic diffraction angle (2θ) of 47.0° and 68.8° correspond to the (220) and (400) planes respectively. This shows that the (220) plane and (400) plane are the dominating plane for the in-plane observation on the CLC film thus supports the observatons form EBSD and TEM. These in-plane observations confirmed that the well-oriented {100} plane growth given that the direction of the horizontal columnar structure follows the direction of the laser scan direction.

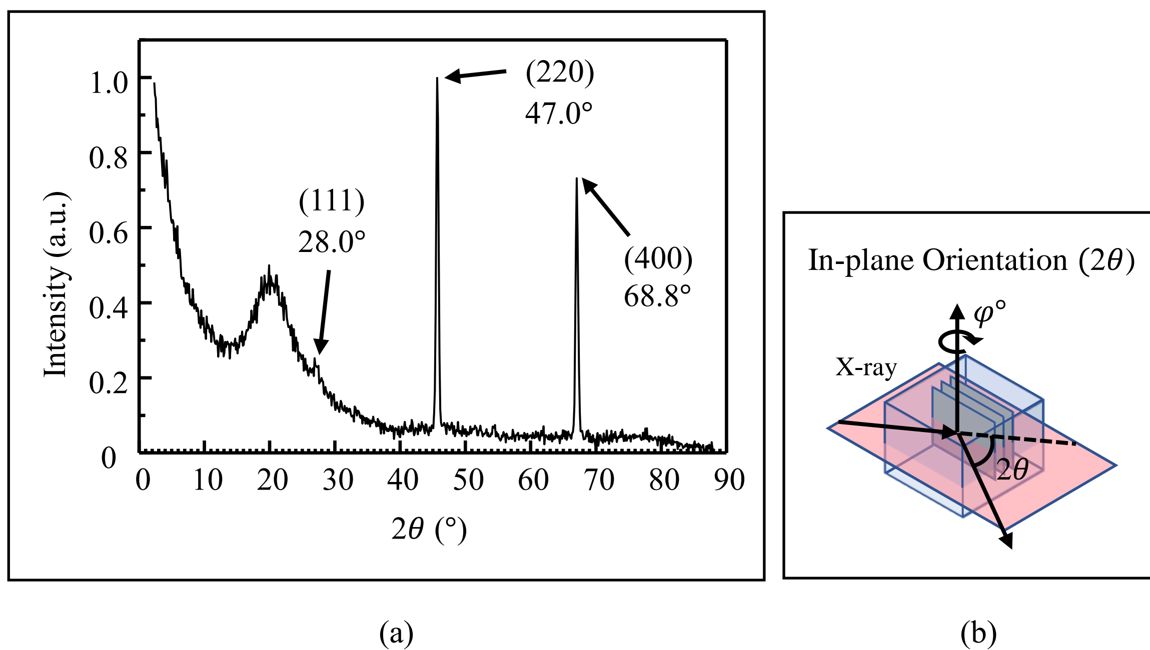

Figure 3.14: (a) XRD spectrum obtained from in-plane measurement with (b) showing schematic of the in-plane measurement.

3.4 Extended growth of {100}-oriented GB free grains

The formation of horizontal columnar structure on the surface of the crystallized film gives an insight on the growth direction of the silicon crystal domains as well as the formation of high angle GBs. This helps in making an instantaneous judgement upon laser irradiation especially on finding the optimum CLC conditions without having to do crystallographic observation by EBSD.

3.4.1 Growth of 12 mm elongated grain

Taking the advantage of the columnar pattern formation, a long GB-free silicon domain extended to more than 12 mm long was successfully grown by CLC under 92 nm C/L at laser power of 3.55 W. Figure 3.15 shows the OM images of the CLC trace on 15 mm × 15 mm

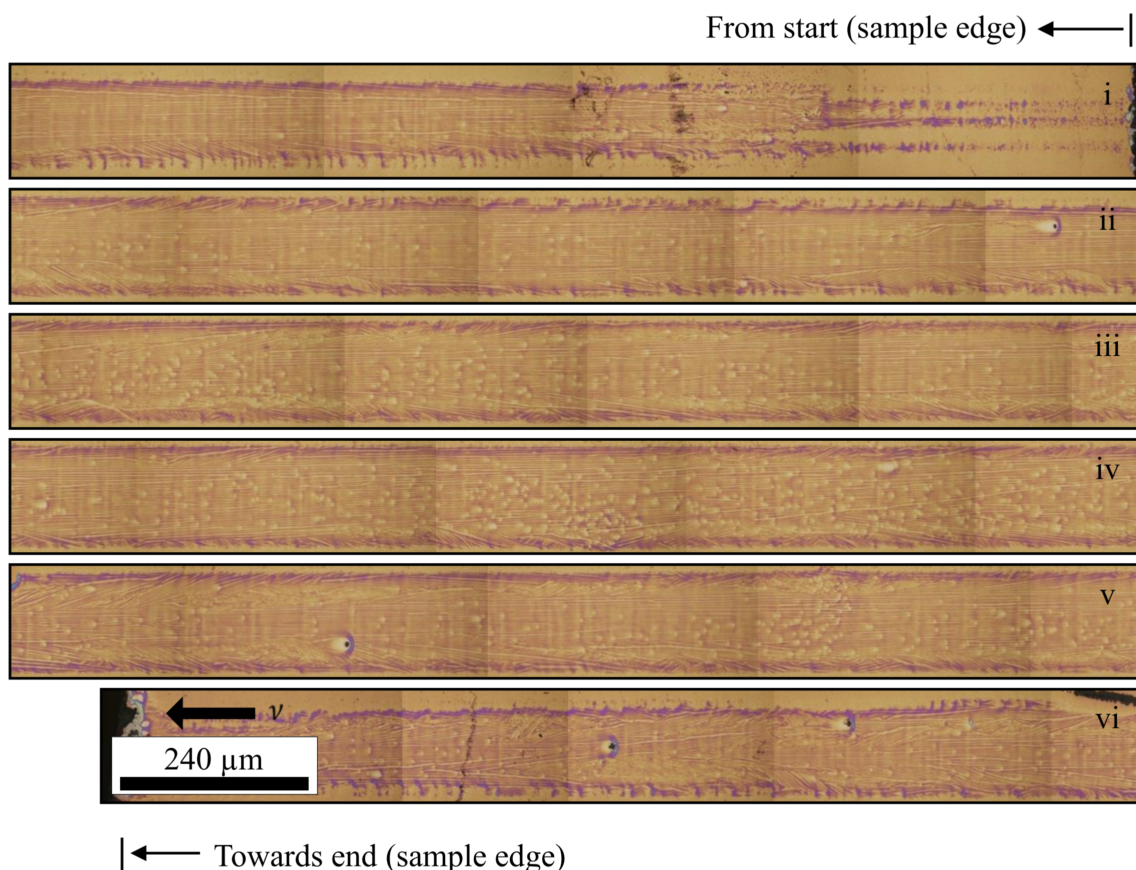

Figure 3.15: OM image of a long scan trace across 15 mm sample. Laser scan was continuous from i to vi and travel from right to left for each image.

sample scanned from outside of one edge and ends at the outside of the other edge as marked with the two vertical lines. The horizontal columnar lines stably grow form the vicinity of the sample edge all the way to the opposite edge which resulted in GB-free domain. The mapping of GMA 15°-65° in Figure 3.16 shows no formation of high angle GB at the center of the domain; observed near the start point of the CLC trace to a point near the end point. This shows that the stable growth of silicon domain by CLC can extend thus far following the laser beam given that no interruption introduced along the way.

The stable growth of the {100} plane may be attributed to the stable solid/liquid frontal plane during the CLC process. However, the formation of the columnar structure might be due to the instability of the solid/liquid frontal shape which induce periodic undulations on the interface with a characteristic wavelength. This phenomenon of columnar structure formation often associated with melt-mediated crystallization and reported multiple of times either experimentally or/and theoretically. Same experimental observation also reported by Grigoropoulos et al. in the laser crystallization of 890 nm thick Germanium film with heated quartz substrate to more than 770 K [9]. The instability of the solidification front was first explained theoretically by Mullins and Sekerka, which interpreted that the diffusion of excess heat from solid/liquid interface leads to the interface shape instability generating sinusoidal

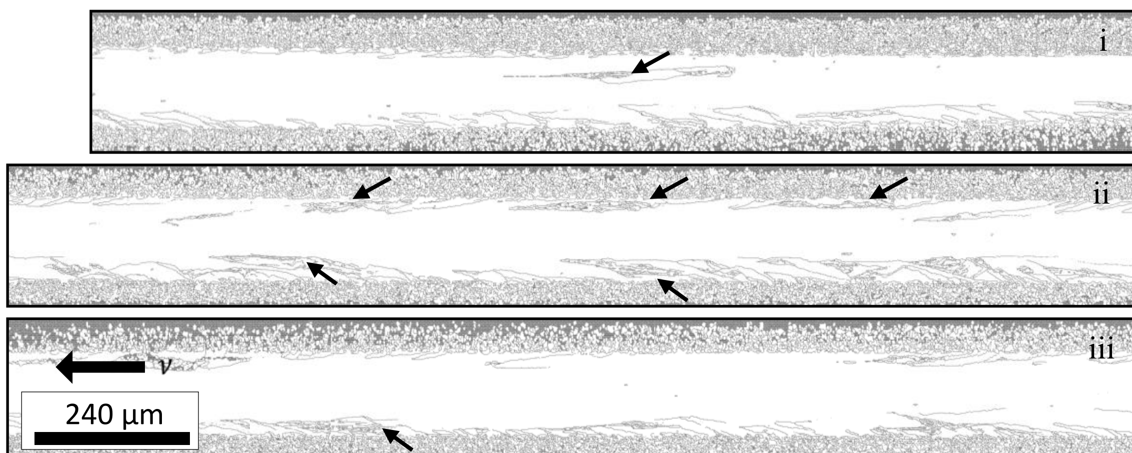

Figure 3.16: GMA 15°-65° from EBSD for the same scan trace in Figure 3.15 at the center of the scan length.

perturbation on the solid/liquid frontal [11]. The instability of the originally planar solid/liquid interface is also referred as the criterion of the growth conditions whenever the unidirectional solidification involves a layer of constitutionally supercooled liquid where the characteristics of the supercooling often depends on the growth rate and the temperature gradient in the liquid melt [12].

Mullins and Sekerka, as well introduced the concept of marginal stability when the amplitude of the perturbation does not change in time, which also referred as the steady-state condition. Deviation from this marginal stability, for instance inducing higher interface velocity during solidification will cause the increase of the amplitude of the perturbation that led to the cellular and dendritic solid/liquid interface. In this experiment, the steady-state sinusoidal interface resulted in the formation of groovy or the so-called columnar trace on the trailing solidified structure due to difference in freezing time of the film behind the protruded front and the non-protruded front. The delayed solidification behind the non-protruded frontal interface causes the higher melt volume to diffuse onto the formerly solidified region which then led to the formation of alternating peaks and valleys in transverse direction. Figure 3.17 illustrates the sinusoidally perturbed solid/liquid frontal interface and the resulting peaks and

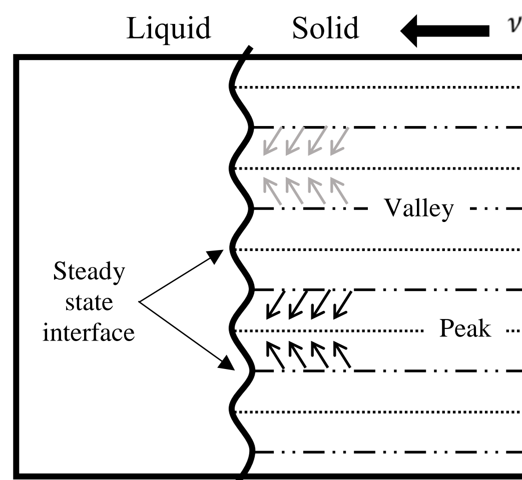

Figure 3.17: Sinusoidally perturbed solid/liquid interface that resulted to the formation of columnar structures on sample surface.

valleys formation during the solidification. The stability of the initial sinusoidally perturbed solid/liquid front are crucial in maintaining the stable growth of the domain. The transformation of the beam shape from line beam into a rectangular beam with Gaussian profile in short axis does modulate the temperature gradient in a manner to reduce the solid/liquid frontal velocity during the solidification thus enhance the stable growth of silicon crystal domains. This mechanism would be the best explanation on the experimental results on the formation of the GB-free silicon film with the horizontal columnar structure.

3.4.1 Formation of low angle GBs and twin boundaries

It is now clear that the formation of the GB-free large silicon domains is manifested by the modification on the laser beam especially on the wider short axis which modulated the temperature gradient in the direction of the solidification. As expected, the orientation of the GB-free domain does follow the direction of the growth direction of the horizontal columnar patterns analyzed by IPF ND, SD and TD from EBSD as shown in Figure 3.18(a), (b) and (c) respectively. Crystal domains with non {100} in-plane orientations at the periphery of the large domain with maintained (100) ND orientation suggests that tilt boundaries are dominant with the rotation axis about [100] direction, a similar phenomenon observed when the CLC was done by using line beam spot.

The {100} in-plane orientation stably grows without the formation of high angle GBs but induces low angle GBs as can be seen from GMA 2°-65° shown in Figure 3.19. The grain boundary angles distinguished by different color code of the mapping with - blue: 2°-5°, red: 5°-10°, green: 10°-15°, and grey: 15°-65°. The low angle GB less than 15° usually regarded as sub boundaries as the GBs did not form any enclosure but rather a form of lineage formed in large crystal domains generated from arrays of edge dislocations during the domain growth. These sub-GBs are expected to impart minimum to no effect on carrier movement on device with such inclusion of sub-GBs.

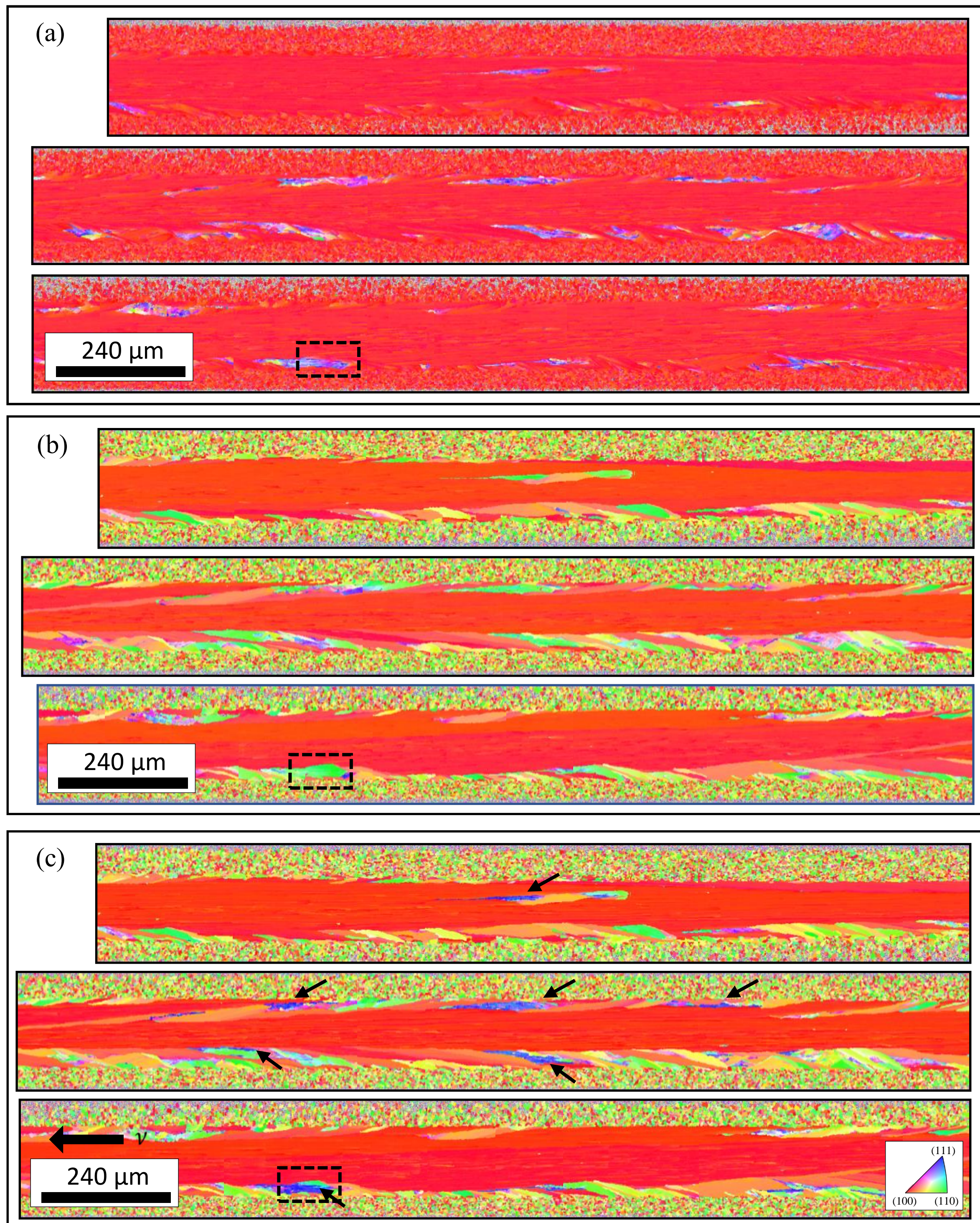

Figure 3.18: Set of EBSD mapping showing (a) IPF ND (b) IPF SD and (c) IPF TD. Laser scan direction was from right to left for each picture and continuous from top to center to bottom of each set.

Another criterion in the studies of grain boundary is the formation of twin boundaries. In the cubic diamond lattice structure, twin boundaries are usually associated with crystal domains having {211}, {110} and {111} planes in the 3 directions of the cubic structure. This twinning formation were observed in the CLC film where the second lowest interface energy of {211} silicon film with SiO_2 substrate (Section 3.1) favors the formation of {211} planes in ND, associated with {110} planes in SD and {111} in TD. These orientations can be observed from Figure 3.18(a), (b) and (c) where the {211}, {110} and {111} orientations are represented by purple, green and blue IPF color code respectively. The areas with the twin boundary formation are shown by the arrows in Figure 3.18(c). Consequently, the boundaries in these regions also indicated by the arrows in Figure 3.16 where high density of GBs were seen in these regions.

Under the stable growth of {110} crystal plane in SD, the twin boundaries will grow in a straight line parallel to the {110} growth direction which is the laser scan direction as shown in Figure 3.20 in the grey shaded area of GMA 2°-65°. The area of the twin analysis was taken from the square dotted area form Figure 3.18. From the observation by optical microscope on the surface of the twinned domain, the formation of columnar structure was distorted in the

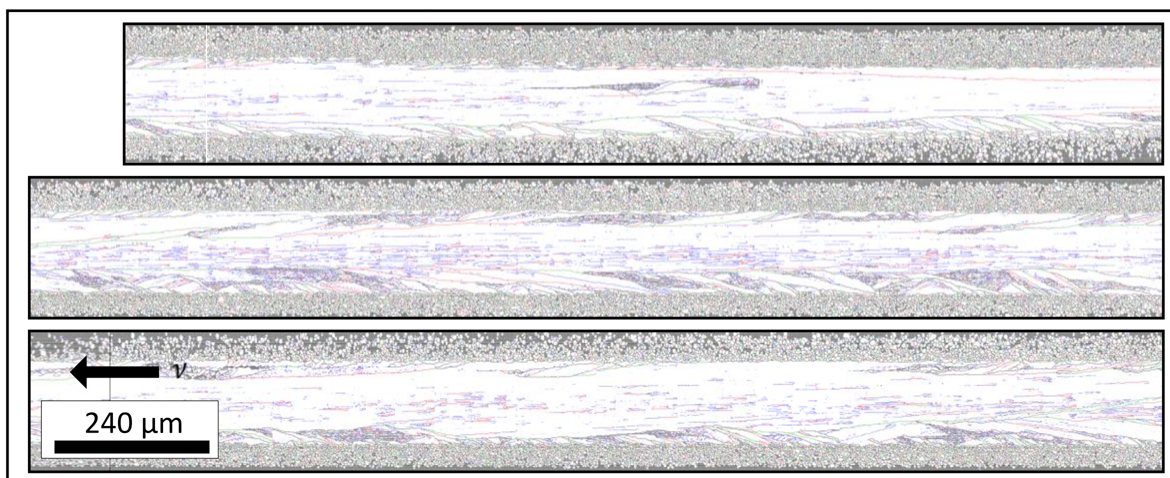

Figure 3.19: GMA 2°-65° mapping from EBSD with different line colors for specific range of GB angles with; - blue: 2°-5°, red: 5°-10°, green: 10°-15°, and grey: 15°-65°.

regions as shown in Figure 3.20(b). The formation of the closely packed twin boundaries parallel to the laser scan direction was due to the fact that the twin formation is associated with the stacking fault of the {111} plane with the rotation angle of 60° about the [111] axis in TD and the generation of twin region is explained by the deformation twinning [13]. The stacking fault induced in the crystals are supposed to promote relaxation of the atoms near the faults [14]. This stacking fault with rotated {111} plane does not cause any change in orientation of the crystal plane in any direction as evidenced by the consistent purple and green color domain in ND and SD respectively, whenever the twin boundaries are formed. Figure 3.21 illustrates the cubic lattice structure in ND and SD with respect to the rotated {111} plane 60° about the <111> axis. The plane orientations in those directions were maintained but the direction of the cubic lattice changes which may be the reason for the dying-out of columnar structure on the surface of the silicon film due to inconsistent {211} structure in ND. The formation of twins usually affiliated with the dendritic growth in silicon and often resulted by fast growing {111}

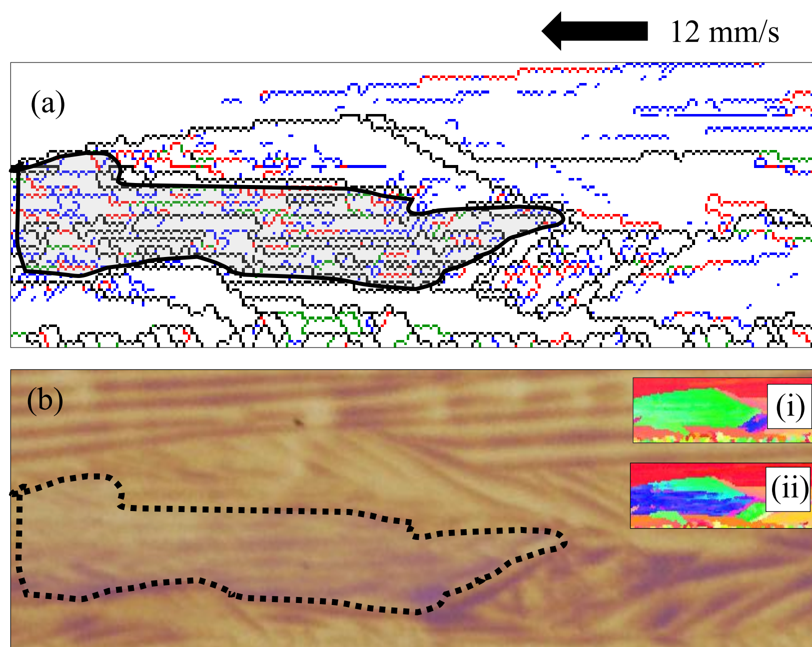

Figure 3.20: Scanned area with twin boundary formation captured by (a) GMA 2°-65° mapping by EBSD and (b) optical microscope shown in the enclosed shape. The inset (i) and (ii) shows the IPF SD and TD respectively.

plane during the solidification induced by rapid cooling process in the region [4,15–21]. Experimentally, crystal domain with twin formation usually observed when irregularities or contaminations on the a-Si film are present as well as at the periphery of the large crystal domain which suggest that the twin formation by CLC may be resulted by the change in temperature gradient in the silicon film at these regions. Additionally, the faceted, tapered looking shape of the domain with twins can be related to the dendritic-like growth. Formation of unwanted twinned domain are uncontrollable and the twin boundaries usually defined as coincidence site lattice (CSL) boundaries or sigma boundaries such as Σ3, Σ9, or Σ27 which possess less effect on the electrical properties of the film compared to other high angle GBs [22].

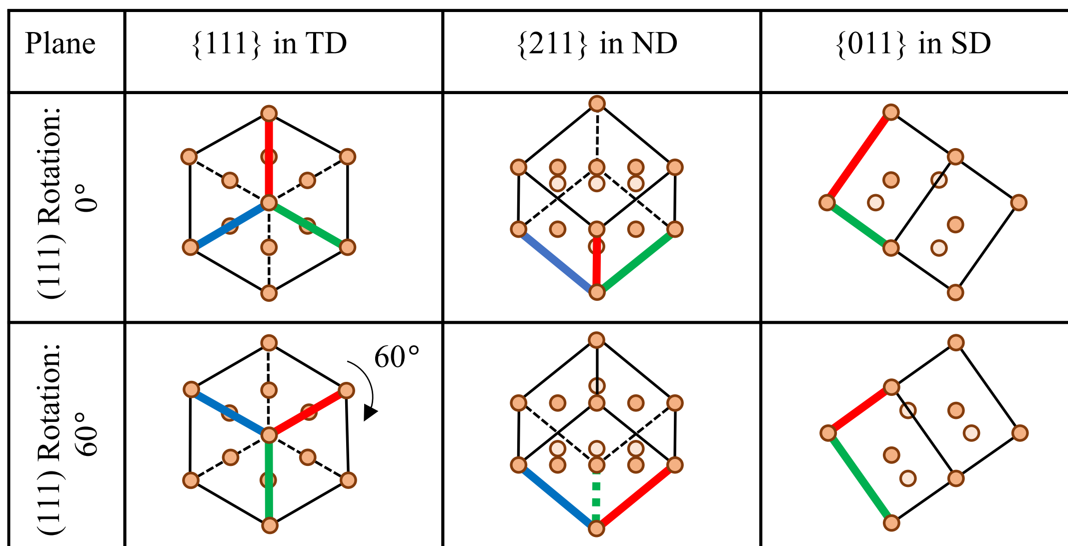

Figure 3.21: Illustrations of diamond cubic lattice structure in {111}, {211} and {110} plane without and with {111} plane rotated 60° about <111> rotation axis.

3.5 Summary

High occupancy percentage of {100} oriented crystal plane in surface normal direction in correspondence to the interfacial energy between the silicon film and underneath quartz substrate was further discussed by referring to reported studies. With the modification made on

the beam shape for CLC; that was from a Gaussian line beam into a rectangular beam with flat-top profile in long axis and Gaussian profile in short axis resulted in a distinct improvement related to silicon domain size and the exclusion of GB formation. The modification in the beam shape was made possible with the combination use of beam expander, DOE and the focusing lens. However, the solidified film upon laser irradiation leaves a pattern of parallel lines which also termed as horizontal columnar lines growing in the direction of the laser scan direction. The columnar structure formed a periodic peaks and valleys separated at a pitch of 2 μm to 5 μm which alternates in the direction of the laser trace width with an average peak-to-valley height of 7 nm. The columnar structures are the artifacts of the sinusoidally perturbed solid/liquid front formed as a characteristic of solidification involving supercooled liquid. The columnar structure serves a guideline in the optimization process since the growth direction of the lines represent the growth of the {100} plane in SD as analyzed by HRTEM. In consequence, a large silicon domain elongated to 12 mm long was stably grown with the exclusion of GBs. Small angle GBs or sub-GBs however are still present in the large domain but expected to impose marginal effect on carrier transport in the film. Small fraction of domains with twin boundaries also grown in the vicinity of the large domain due to expected change in temperature gradient in the area. This large, highly oriented film crystallized by rectangular beam are expected to offer better TFTs performance with minimum point-to-point disparity.

3.6 References

1. Y. Wang, M. D. Chahal, J. J. Wang, A. B. Limanov, A. M. Chitu, and J. S. Im, Mater. Res. Soc. Symp. Proc. **1770**, 55 (2015).

2. D. P. Gosain, A. Machida, T. Fujino, Y. Hitsuda, K. Nakano, and J. Sato, Japanese J. Appl. Physics, Part 2 Lett. **42**, L 135 (2003).

3. M. He, R. Ishihara, W. Metselaar, and K. Beenakker, J. Appl. Phys. **100**, 083103 (2006).

4. M. Chahal, Dr. Thesis, Columbia Univ. (2012).

5. N. Sasaki, Y. Nieda, D. Hishitani, and Y. Uraoka, Dig. Tech. Pap. - SID Int. Symp. **47**, 1317 (2016).

6. S. Fujii, S. I. Kuroki, K. Kotani, and T. Ito, Japanese J. Appl. Physics, Part 1 Regul. Pap. Short Notes Rev. Pap. **46**, 2501 (2007).

7. J. W. Rutter and B. Chalmers, Can. J. Phys. **31**, 15 (1953).

8. K. Hirose, M. Kobata, T. Sato, K. Kitahara, and A. Hara, Jpn. J. Appl. Phys. **49**, 03CA07 (2010).

9. C. Grigoropoulos, M. Rogers, S. H. Ko, A. A. Golovin, and B. J. Matkowsky, Phys. Rev. B - Condens. Matter Mater. Phys. **73**, 184125 (2006).

10. K. A. Takeuchi, H. L. Yang, F. Ginelli, G. Radons, and H. Chaté, Phys. Rev. E - Stat. Nonlinear, Soft Matter Phys. **84**, 1 (2011).

11. W. W. Mullins and R. F. Sekerka, J. Appl. Phys. **35**, 444 (1964).

12. W. A. Tiller, K. A. Jackson, J. W. Rutter, and B. Chalmers, Acta Metall. **1**, 428 (1953).

13. N. Sasaki, M. Arif, and Y. Uraoka, Jpn. J. Appl. Phys. **58**, SBBJ02 (2019).

14. M. Y. Chou, M. L. Cohen, and S. G. Louie, Phys. Rev. B **32**, 7979 (1985).

15. K. Fujiwara, K. Maeda, H. Koizumi, J. Nozawa, and S. Uda, J. Appl. Phys. **112**, 113521 (2012).

16. J. Pohl, M. Müller, A. Seidl, and K. Albe, J. Cryst. Growth **312**, 1411 (2010).

17. K. Kutsukake, T. Abe, N. Usami, K. Fujiwara, K. Morishita, and K. Nakajima, Scr. Mater. **65**, 556 (2011).

18. G. S. Ganot, Dr. Thesis, Columbia Univ. (2012).

19. J. S. Im, M. Chahal, P. C. Van Der Wilt, U. J. Chung, G. S. Ganot, A. M. Chitu, N. Kobayashi, K. Ohmori, and A. B. Limanov, J. Cryst. Growth **312**, 2775 (2010).

20. R. Trivedi and W. Kurz, Acta Metall. **34**, 1663 (1986).

21. P. K. Galenko and D. A. Danilov, Phys. Rev. E - Stat. Physics, Plasmas, Fluids, Relat. Interdiscip. Top. **69**, 14 (2004).

22. K. Kitahara and A. Hara, Cryst. - Sci. Technol. (2012).

CHAPTER 4:

TFT Characteristics Fabricated on GB-free Silicon Film

A long GB-free silicon domain resembling a single crystal was obtained by a modification in the laser beam spot from a line beam to a rectangular beam with flat-top profile in long axis and Gaussian profile in short axis. Furthermore, the grown domain shows a very high percentage of {100} plane growing in ND, RD and TD. The consistent RD and TD is expected to allow the carrier movement to be uniform regardless the direction of the carries in RD or TD given that there are no geometrical defects that can selectively hinder the carrier movement in a certain direction. The obtained {100} oriented quasi-single crystal silicon are expected to serve such purpose in order to reduce the point-to-point TFT performance as well as the effect of channel geometric in order to improve the uniformity of the device fabricated on large are. This chapter focus on TFT fabrication to justify that the crystallized film possesses the characteristic of high-performance, high-uniformity SOI TFTs.

4.1 Grain boundary effects on TFT carriers

Grain boundary scattering is one of the natures of poly-Si that needs to be delt with in order to improve the carrier transport. Literally, this is the main factor that degrade the

performance of poly-Si away from that of single-crystal silicon. GBs in poly-Si introduce discontinuity of the periodic lattice structure and regarded as defects with inclusion of dangling bonds and strained bonds. These defects account for the introduction of electronic states in the band gap where dangling bonds will lead to deep states while stranded bonds lead to tail states formation [1,2]. Like a-Si, deep state and tail state act as the trapping centers which enhance the recombination and generation of charges in the film. Figure 4.1 illustrates the model of grain boundary in n-type semiconductor with hole trapping at the grain boundaries. The trapping prompted to charge depletion region and eventually caused the band bending in the

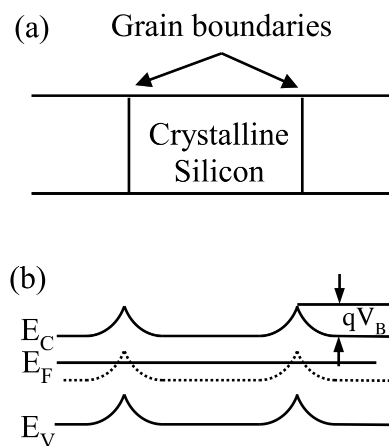

Figure 4.1: Grain boundary (a) illustration in poly-Si film and (b) band bending in the energy diagram for n-type poly-Si.

vicinity of the GB as illustrated in Figure 4.1(b) where qV_B is the barrier height [3]. The induced potential barriers restrict the electron mobility in the poly-Si at the grain boundary during the operation of the device, a TFT in particular. In order to minimize the effect, exclusion of grain boundaries is necessary to achieve the device performance comparable to that of fabricated with single crystalline silicon. Conventional poly-Si TFTs fabricated by means of SPC or ELA which induces granular grains suffer from this problem. Lateral grown poly-Si domains by CLC on the other hand reduce the effect with the elongated grains. Nevertheless, given that TFTs fabricated for a single pixel in display manufacturing which

might have up to four TFTs to compensate for the threshold voltage for instance, the orientation of the TFT channels might not always be in the same direction as the lateral grown poly-Si [4]. In such case, the performance of the elongated poly-Si TFTs will differ depending on the geometry of the TFT structure as the carriers moving in the direction parallel to the GBs will encounter less GB effects compared to the one moving perpendicular to the GBs [3,5].

Figure 4.2 illustrates the TFT structures with channel orientation directed in a parallel (∥) and perpendicular (⊥) manner with respect to the GBs; with GBs grown in the direction of the laser scan. Figure 4.2(a) and (b) represent the ∥ and ⊥ TFTs respectively, fabricated on granular poly-Si grains which might have less performance disparity compared to elongated grains shown in (c) and (d) where carriers in ⊥ TFTs need to pass the potential barrier at GBs. Such dependency can be avoided by fabricating the TFTs on quasi-single crystalline silicon without incorporation of high angle GBs. Given that such grain can be grown with rectangular

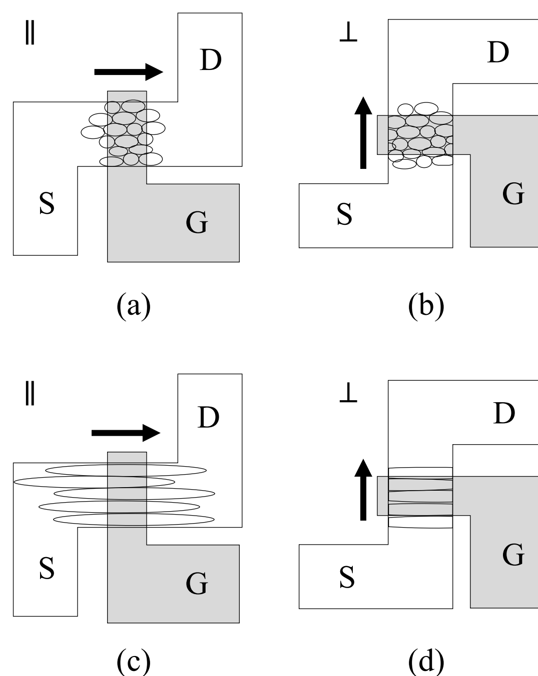

Figure 4.2: Illustration of TFTs fabricated with channel direction oriented (a) parallel and (b) perpendicular to laser scan direction on granular grains as well as TFTs with elongated grains with channel direction (c) parallel and (d) perpendicular to laser scan direction. The arrows show the direction of carrier flow during operation.

beam by CLC as discussed in Chapter 3, the geometrical dependency of the channel direction with respect to the silicon growth direction can be minimized. Thus, TFT performance fabricated on silicon grown by line beam (Chapter 2) and rectangular beam (Chapter 3) were compared to justify the quality of the elongated GB-free silicon domain.

4.2 TFT fabrication process

The CW laser crystallized samples were used for the TFT fabrication with coplanar top gate structure to study the electrical characteristic of the poly-Si film. The complete flow of the TFT fabrication process is illustrated in Figure 4.3. After laser crystallization, SiO_2 C/L was removed by buffered hydrofluoric (BHF) solution until de-wetting was observed on the silicon film. High SiO_2 to silicon etching selectivity of BHF prevents over etching of the original 60 nm silicon film. Channel patterns were then formed by means of ultraviolet (UV) lithography using the conventional photomask with chromium pattern on quartz substrate. Samples with patterned resist were subjected to inductively coupled plasma-reactive ion etching (ICP-RIE) to translate the pattern onto the underneath silicon layer. The anisotropic etching was completed by ions formed by a mixture of 29:1 flow rate ratio of carbon tetrafluoride (CF_4) and oxygen (O_2) plasma generated by 300 W ICP bias power and 10 W lower cathode bias at 1 Pa with Helium (He) used to control the stage temperature to ensure uniform etching over the samples.

After channel island formation, the exposed channel islands were then cleaned by piranha solution followed by RCA cleaning before SiO_2 gate insulator deposition. The flow of the cleaning process and conditions were similar to that of a-Si film cleaning process before SiO_2 C/L deposition prior to the laser crystallization. Similarly, the 120 nm SiO_2 gate insulator deposition by TEOS-CVD followed the same deposition technique with that of C/L deposition at 300°C in 80 Pa pressure and 150 W bias. Next, gate structure was patterned with sacrificial

photoresist for lift-off process and subsequently, 250 nm molybdenum (Mo) film was deposited by sputtering technique with 100 W radio frequency (RF) power in 15 sccm flowing Argon (Ar) to keep the pressure at 0.25 Pa before resist stripping by acetone was carried out to complete the gate formation process. After gate formation, the samples were sent to Toray research center for ion implantation where 4×10^{15} cm^{-2} phosphorus ions (P^+) were implanted at 90 keV to define the self-align source and drain region of the TFTs. Thick Mo gate which prevents the ion penetration ensures the intrinsic channel properties while source and drain regions are highly doped which transforms the TFTs into an n-type TFTs. The implanted ions then activated by furnace annealing at 550°C in N_2 ambient for 30 minutes.

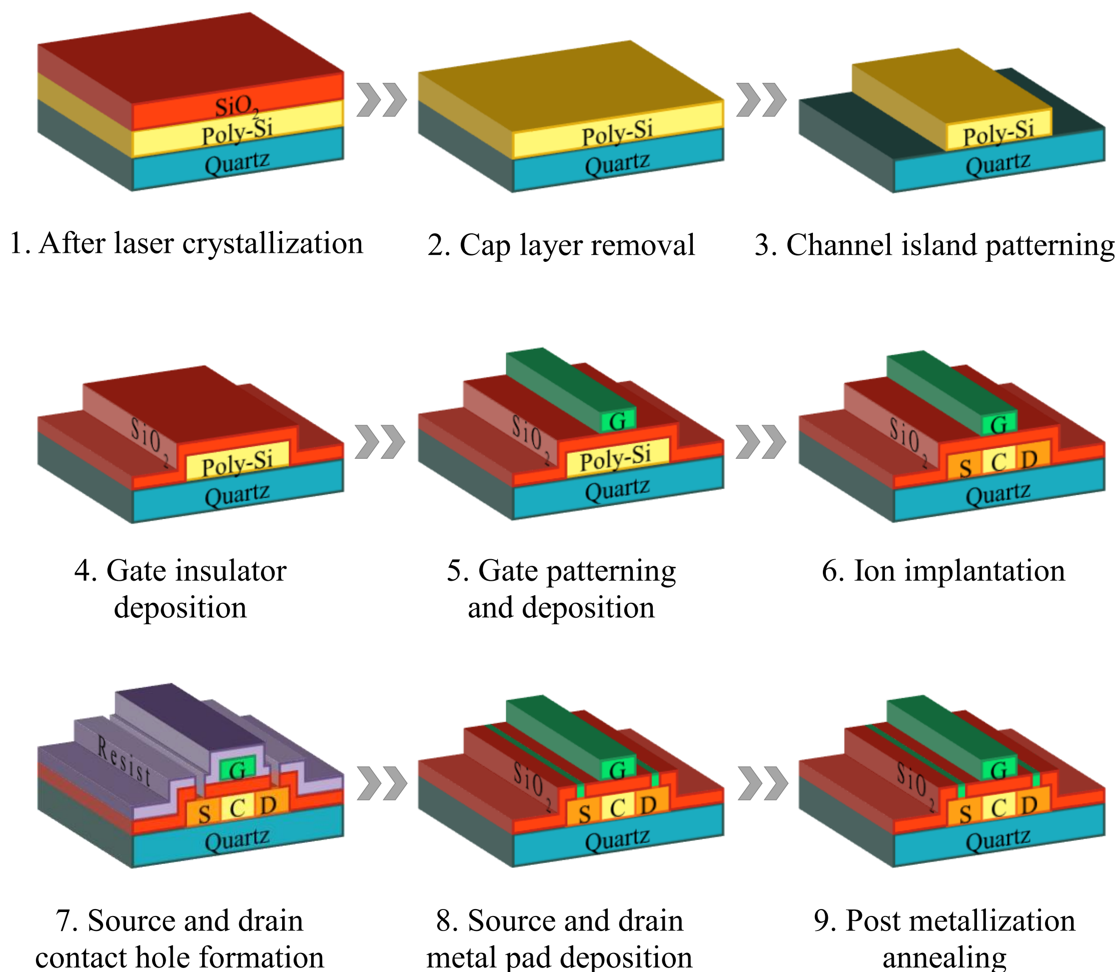

Figure 4.3: Schematics of TFT fabrication process and the illustration of cross-sectional structure.

Then, contact holes were patterned on top of the source and drain regions where the SiO_2 gate insulator film was then etched by BHF solution. The same photoresist for the contact hole formation was used as the sacrificial film in the lift-off process for the source and drain metal pad deposition. Sputtered Mo film was used for the metal electrode in the source and drain regions similar to the one used for the gate metal with the same thickness of 250 nm. To complete the fabrication process, the TFTs were subjected to post metallization annealing (PMA) in forming gas with 5% H_2 in N_2 ambient at 400°C for 30 minutes to minimize the density of interface state which may lead to increase in device's leakage current as well as to improve the ohmic contact between the source and drain with the newly deposited Mo pad. Table 4.1 shows the summarized details of the TFT fabrication process with every process conditions.

Figure 4.4 shows the plane view of a fabricated TFT having a channel width of 5 µm and length of 10 µm captured by optical microscope. Figure 4.4(a) shows the picture of channel pattern after ICP-RIE, (b) after gate formation, (c) after contact hole opening by BHF and (d) after source and drain metal pad formation which referred to the TFT structure after process number 3, 5, 7 and 8, respectively from Figure 4.3. Figure 4.5 shows the magnified plane view of channel area for the TFT pattern extracted from the squared region in Figure 4.4(d). The

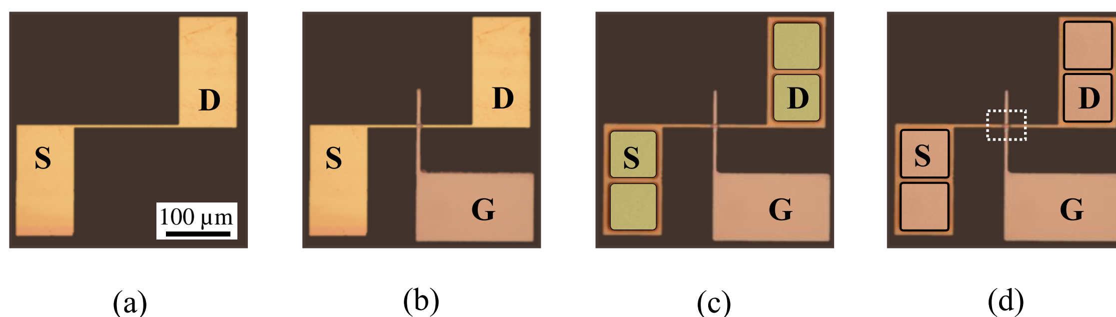

Figure 4.4: Top view of TFT pattern with channel width/length of 5 µm /10 µm captured by optical microscope after (a) channel patterning, (b) gate formation, (c) contact hole opening and (d) source and drain metal pad deposition. Transistor's source, drain and gate are marked with S, D and G respectively.

channel area has a dimension of 5 μm in width and 10 μm in length. The thick black arrow indicates the typical laser scan direction. Figure 4.6 shows the cross-section schematic of the fabricated self-align n-type top gate TFT with the CLC processed channel region.

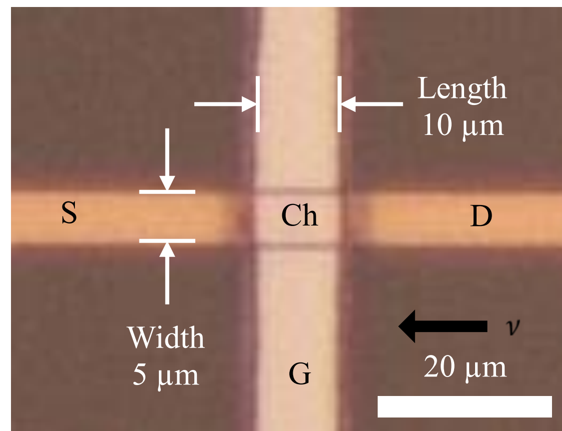

Figure 4.5: Magnified plane view of TFT channel region (Ch) with channel width of 5 μm and length of 10 μm.

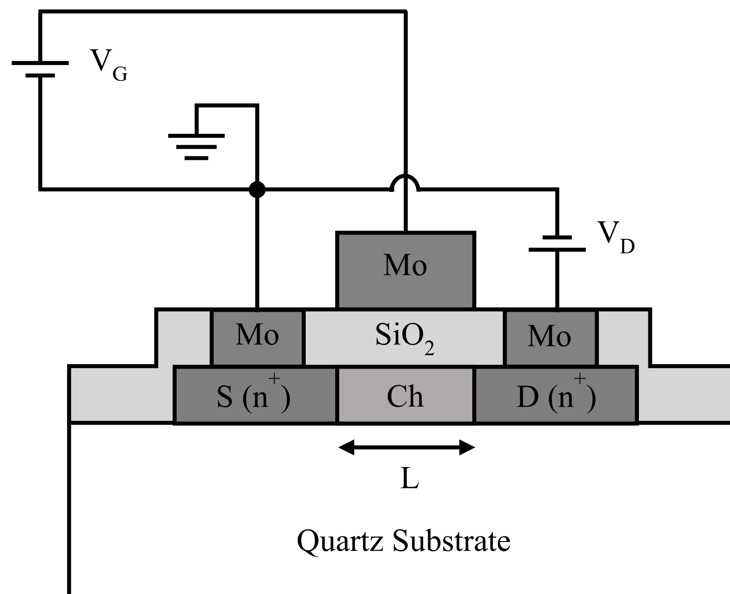

Figure 4.6: Schematic structure of n-type top gate TFT with heavily doped source (S) and drain (D) regions.

Table 4.1: Details of the TFT fabrication process conditions.

1. Laser crystallization	1. Verdi V-2: Nd:YVO_4 (λ = 532 nm), ν = 12~15 mm/s, P = 1.0~5.0 W.
2. SiO_2 cap layer removal	2. BHF solution, 2~3 mins, room temperature
3. Channel island pattering and etching	3.1. Resist patterning (for channel island): - AZGXR602 positive photoresist spin coating (3000 rpm,15 s), prebaking (100°C, 60 s), UV exposure (10 s), developing by AZ300MIF (35 s), post baking (120°C, 120 s). 3.2. Channel etching: - (Samco ICP-RIE) CF_4:O_2 = 29:1 sccm, ICP = 300 W, Bias = 10 W, 1 Pa, He = 10 × 10^2 Pa.
4. Sample cleaning and gate SiO_2 gate insulator deposition	4.1 Cleaning: - H_2SO_4 clean and RCA cleaning: - (refer to Table 2.1 No.1) 4.2 Gate Insulator deposition (120 nm): - PECVD: TEOS:O_2 = 3:300 sccm, 300 °C, 80 Pa, RF power = 150 W.
5. Gate Patterning and deposition	5.1 Resist patterning (for gate): - AZ5218 negative photoresist spin coating (3000 rpm,15 s), prebaking (90°C, 60 s), UV exposure (2 s), mid baking (110°C, 90 s), UV flood exposure (15 s), developing by AZ300MIF (45 s), post baking (120°C, 60 s). 5.2 Gate deposition: - Molybdenum, Ar = 15 sccm, RF = 100 W, 0.25 Pa, rotation = 8 Rot/m, target-sample distance: 50 mm.
6. Ion implantation and activation	6.1 Ion implantation: - Phosphorus ion (P^+), 4 × 10^{15} cm^{-2}, 90 keV 6.2 Dopant activation: - N_2 ambient, 500°C, 30 mins.
7. Contact hole formation	7.1 Resist patterning (for contact hole): - same process condition as in 3.1. 7.2 Contact hole etching: - BHF solution, 2~4 mins, room temperature.
8. Source and drain metal pad deposition	8. Molybdenum deposition: - Same process condition as in 5.2.
9. Post metallization annealing	9. Forming gas: 5% H_2 in N_2, 400°C, 30 mins.

4.3 Channel geometrical effect on TFT performance

In order to confirm the grown film by rectangular laser beam which expected to have no grain boundary, TFTs were fabricated on such film in a manner that the channel direction is aligned to be in the direction of laser scan or perpendicular to laser scan. By comparing the performance of the TFTs with such dependency, the existence of grain boundary can be expected if large variation of TFTs performance is seen for different channel orientation. Normally, TFTs with carrier movement direction parallel to GB will experience less scattering effect compared to the one travelling through the GBs [3,6]. For reference, TFTs were also fabricated on a typical poly-Si film crystallized by the Gaussian line beam.

4.3.1 TFTs on typical CLC poly-Si

The crystallized area by Gaussian line beam were selected for the TFT fabrication where the channel patterns were aligned on the laser scan trace to accommodate the “parallel” and “perpendicular” TFTs. Figure 4.7(a) shows the OM image of the TFT islands photoresist aligned with the laser scan trace. Black dotted lines indicate the side of a scan trace with the width pointed by the arrow. The orientations of the TFT channels are indicated by ∥ and ⊥ for the parallel and perpendicular channel, respectively. Figure 4.7(b) and (c) shows the EBSD

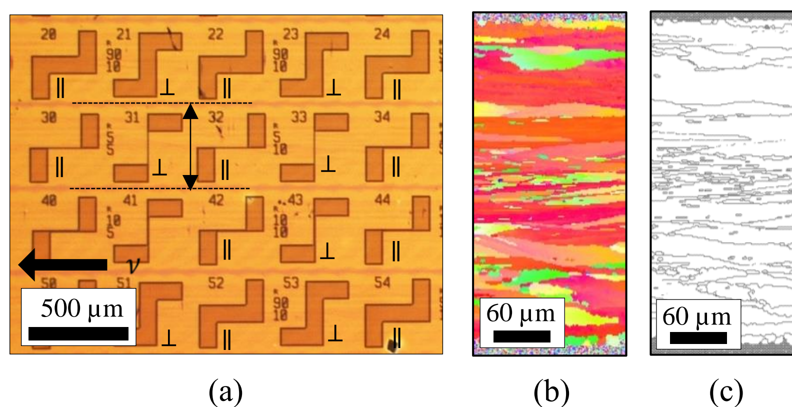

Figure 4.7: TFT islands patterned on laser scan trace by line beam CLC (a) captured by optical microscope. Dotted lines indicate the side of the single scan trace. The orientation of each TFT channels with respect to laser scan direction are also indicated. EBSD mappings show the (b) IPF RD and (c) GMA 15°-65° for each laser scan.

mappings of IPF RD and GMA 15°-65° for each of the laser scans which was crystallized with same CLC conditions. Note that GBs are included in the center of the laser trace where the channel area of the TFTs are patterned. Two sets of TFT channel dimensions are compared for the particular case with TFTs having a width/length (W/L) value of 5μm /10μm (referred as 5/10 hereafter) and W/L of 90μm/10μm (referred as 90/10 hereafter). Figure 4.8 shows the transfer characteristics of the measured TFTs with W/L = 5/10. The measurement was done at room temperature with Drain bias voltage (V_D) of 0.1 V while the Gate voltage (V_G) sweeps from -10 V to 10 V with 100 mV step.

For the parallel TFTs, average electron field effect mobility (μ_{FE}), of 326.29 ± 50.41 cm^2/Vs was obtained with threshold voltage (V_{Th}) of -0.96 ± 1.23 V and subthreshold swing (S.S.) of 0.196 ± 0.020 V/dec. Meanwhile, the values obtained for perpendicular TFTs were averaged at 252.49 ± 53.57 cm^2/Vs, -0.94 ± 1.45 V and 0.194 ± 0.036 V/dec, respectively. TFT transfer characteristics for W/L = 90/10 are shown in Figure 4.9 where the measurement conditions were similar to that of W/L = 5/10. For the W/L = 90/10 TFTs with parallel channel, average μ_{FE}, V_{Th}, and S.S. were 380.37 ± 62.60 cm^2/Vs, -2.52 ± 1.45 V and 0.267 ± 0.089 V/dec respectively. With perpendicular channel, those values degraded to 233.29 ± 42.75 cm^2/Vs, -3.63 ± 1.48 V and 0.348 ± 0.117 V/dec, respectively.

The summarized average values of the electron mobility (μ_{FE}), threshold voltage (V_{Th}) and subthreshold swing (S.S.) together with the standard deviations are tabulated and shown in Table 4.2 for both W/L of 5/10 and 90/10. The threshold voltage was considered as the minimum V_G required to reach at least 1 nA drain current (I_D). For the W/L = 5/10 TFTs, the average mobility drops 22.6% from 326.29 cm^2/Vs to 252.49 cm^2/Vs when the channel orientation changed from parallel to perpendicular while the TFTs with W/L = 90/10 shows a more drastic mobility drop of 38.6% which was from 380.37 cm^2/Vs to 233.29 cm^2/Vs. It is apparent that a perpendicular TFT with a wider channel will encounter more potential barriers

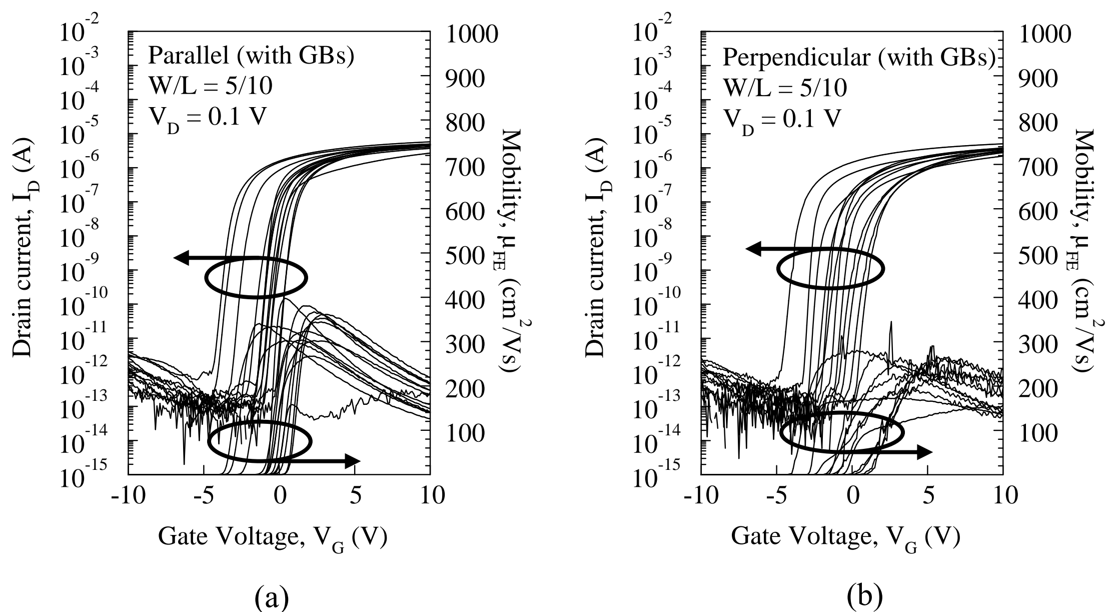

Figure 4.8: Transfer characteristics of W/L = 5/10 TFTs fabricated on CLC trace with GBs for channel orientation in (a) parallel and (b) perpendicular to the laser scan direction.

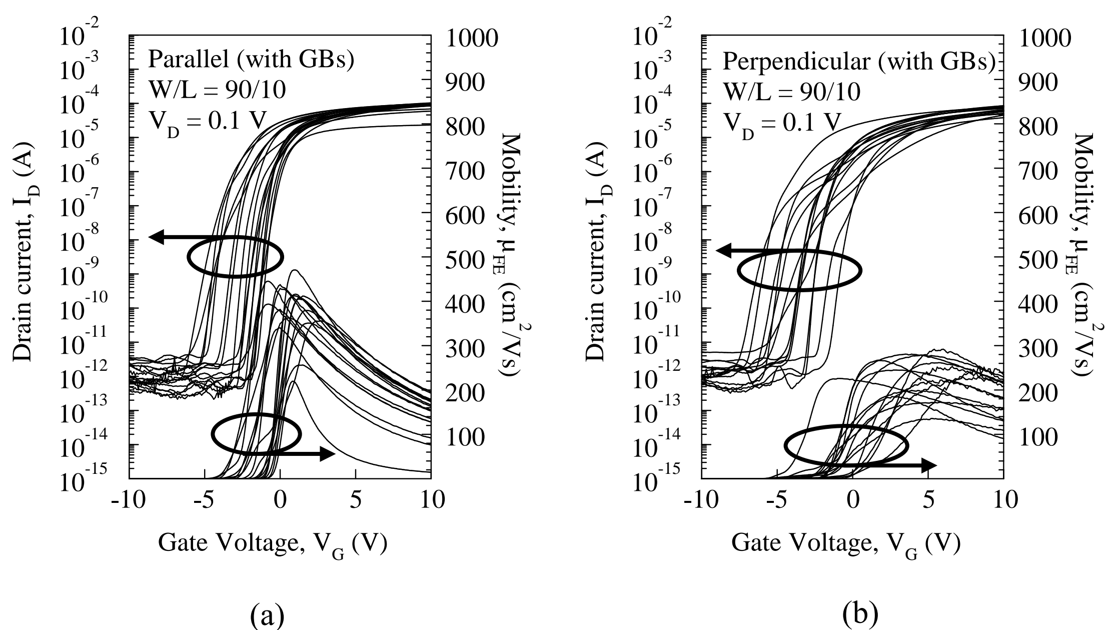

Figure 4.9: Transfer characteristics of W/L = 90/10 TFTs fabricated on CLC trace with GBs inclusion for channel orientation in (a) parallel and (b) perpendicular to the laser scan direction.

at the GB during the operation compared to the one with narrower width thus resulting in more severe mobility drops. A noticeable degradation in V_{Th}, and S.S. also seen for TFTs with W/L = 90/10 with percentage of 44.31 % and 30.38% respectively while the change was kept minimum for the 5/10 TFTs. The high ratio of the on current to the off current (I_{on}/I_{off}) about 10^8 are almost consistent across the TFTs regardless the channel dimension and orientation. However, the highs and lows of the I_D in ON mode and OFF mode are slightly changed for different channel dimensions. It was seen that the I_{off} for W/L = 5/10 lies around 10^{-13} and increase up to 10^{-5} during the ON mode, which is different for the case of W/L = 90/10 with $I_{off} = 10^{-12}$ and $I_{on} = 10^{-4}$. Nevertheless, the ratio did not change regardless the orientation of the carrier flow which is different from the reported results by Nguyen et. al [3] where the I_{off} of the parallel TFT was two orders larger than that of perpendicular TFT. From this experiment, the I_{off} are less likely affected by the grain boundary but the small difference between the I_{off} of the parallel and perpendicular TFTs might be due to the surface orientation of the silicon film. The highly (100) ND orientation promotes low interface states between the silicon channel and gate insulator thus reduce the chance of the trap-assisted tunnelling [7].

Table 4.2: Summary of average electron mobility, threshold voltage and subthreshold swing of W/L = 5/10 and 90/10 TFTs with parallel and perpendicular channel direction.

Channel Orientation	**Mobility, μ (cm^2/Vs)**	**Threshold Voltage, V_{Th} (V)**	**Subthreshold Swing, S.S. (V/dec)**
Parallel (ǁ) – 5/10	326.29 ± 50.41	-0.96 ± 1.23	0.196 ± 0.020
Perpendicular (⊥) – 5/10	252.49 ± 53.57	-0.94 ± 1.45	0.194 ± 0.036
Difference percentage – 5/10	**22.60 %**	**0.76%**	**0.89%**
Parallel (ǁ) – 90/10	380.37 ± 62.60	-2.52 ± 1.45	0.267 ± 0.089
Perpendicular (⊥) – 90/10	233.29 ± 42.75	-3.63 ± 1.48	0.348 ± 0.117
Difference percentage – 90/10	**38.60 %**	**44.31 %**	**30.38%**

4.3.2 TFTs on GB-free quasi-single crystal silicon film

The formation of the clusters of horizontal columnar structure on the surface of the CLC silicon film by rectangular beam which resembled a large silicon domain made the area selection for the TFT fabrication to be possible. In another word, the TFT channel position can be patterned on the GB-region by considering those columnar structures. For instance, channel

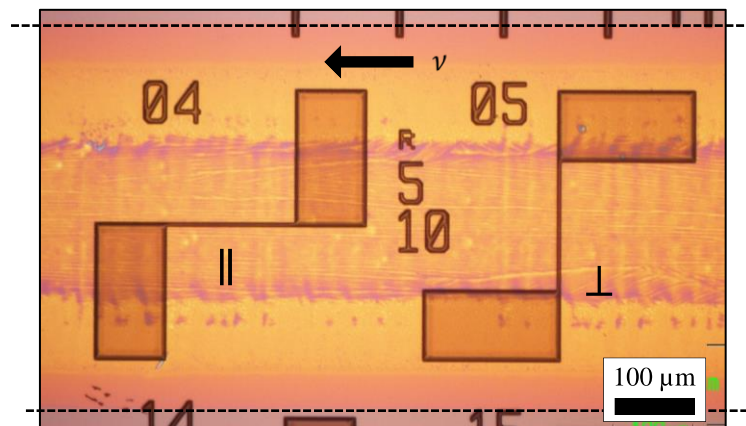

Figure 4.10: Optical microscope image of patterned photoresist for TFT island formation. The channel direction of the left TFT is parallel to the laser scan direction while the one on the right is perpendicular to the laser scan direction.

island on the left side in Figure 4.10 shows the aligned channel pattern (photoresist) in a direction parallel to the laser scan direction while the pattern on the right side shows the one oriented in perpendicular direction. Horizontal dotted lines represent the edge of the laser scan trace while the black arrow shows the laser scan direction. Since the cluster of highly parallel columnar structure can be regarded as a single silicon domain, it was expected that no active GBs were existed in the domain thus eliminate the dependency of the TFT channel orientation on the carrier mobility. Figure 4.11 shows the transfer characteristics of the parallel (a) and perpendicular (b) TFTs measured with the same conditions as the one fabricated on typical CLC poly-Si film. A rather small difference was seen between the two different channel orientation TFTs. The average μ_{FE} obtained for parallel TFTs are 362.81 $\pm$ 81.41 cm^2/Vs with

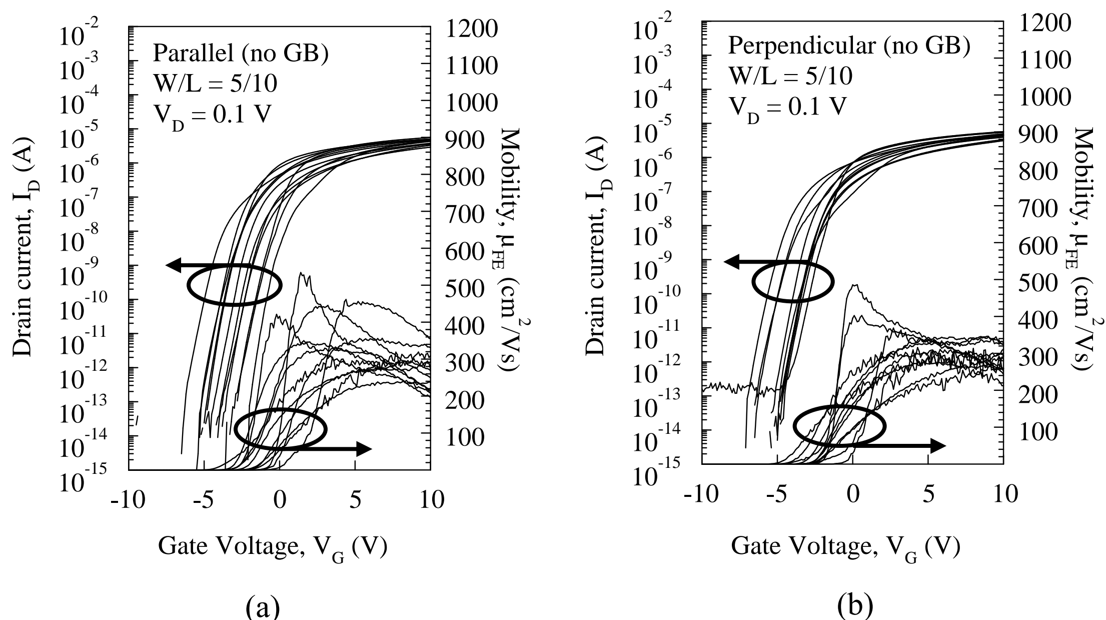

Figure 4.11: Transfer characteristics of W/L = 5/10 TFTs fabricated on GB-free silicon domain for channel orientation in (a) parallel and (b) perpendicular to the laser scan direction.

V_{Th} of -2.34 ± 1.25 V and S.S. of 0.309 ± 0.055 V/dec. The values measured for the perpendicular TFTs averaged at 343.46 ± 54.35 cm^2/Vs, -3.13 ± 1.05 V and 0.296 ± 0.093 V/dec respectively. The measured average values are tabulated in Table 4.3 together with the standard deviation. The most prominent improvement seen on the TFT with GB-free film is that the very subtle difference in the mobility value for perpendicular TFTs compared to the parallel one with only 5.33% reduction. The overall comparison between the TFTs fabricated on typical CLC poly-Si with W/L = 5/10 and 90/10 with the one fabricated on GB-free silicon domain as shown in Table 4.4.

Table 4.3: Summary of average electron mobility, threshold voltage and subthreshold swing of W/L = 5/10 TFTs fabricated on GB-free silicon domain.

Channel Orientation	Mobility, μ (cm^2/Vs)	Threshold Voltage, V_{Th} (V)	Subthreshold swing, S.S (V/dec)
Parallel (‖)	362.81 ± 81.41	-2.34 ± 1.25	0.309 ± 0.055
Perpendicular (⊥)	343.46 ± 54.35	-3.13 ± 1.05	0.296 ± 0.093
Difference percentage	**5.33%**	**34.11%**	**4.22%**

Table 4.4: Overall TFT performance for TFTs fabricated on typical poly-Si and on GB-free domain.

GB-free	W/L	Mobility (cm^2/Vs)		Threshold Voltage (V)		Subthreshold swing (V/dec)	
		∥	⊥	∥	⊥	∥	⊥
×	90/10	380.37	233.29	-2.52	-3.63	0.267	0.348
		38.60 %		44.31 %		30.38%	
×	5/10	326.29	252.49	-0.94	-0.95	0.196	0.194
		22.60 %		0.76%		0.89%	
○	5/10	362.81	343.46	-2.34	-3.13	0.30	0.296
		5.33%		34.11%		4.22%	

Overall, the quality of the TFTs fabricated on poly-Si by CLC shows a promising electrical characteristics with high electron mobility exceeding 300 cm^2/Vs regardless the thin 60 nm channel layer. The value are considered the average value at such thickness comparing to other reports [8,9]. Besides the mobility values, other parameters also shows a good characteristics, for instance the high I_{on}/I_{off} ratio as well as remarkably low off current. Highly oriented silicon domains even for the film with GB formation in the direction of laser scan does promote good switching behaviour for example when comparing the parallel 5/10 TFTs with and without GB film formation. This is due to the negligible effect of GB when the carrier moves along the direction of the GBs.

Ultimately, the exclusion of GB in the film crystallized with rectangular beam successfully eliminated the dependency on the TFT channel direction with respect to the laser scan direction by promoting consistent carrier mobility moving parallel or perpendicular to the direction of the crystal growth. The typical lateral grown poly-Si by CLC induces the GB formation growing in the direction of crystal growth; thus restrict the carrier movement when prompted to move in the direction perpendicular to the grain boundary. The effect of the grain boundary became more pronounce in this manner as there are no other way for the carriers to

pass across the channel region without interacting with the charges trapped at the vicinity of the GBs.

4.4 Summary

The TFT performance compared on typical CLC poly-Si shows an overall good TFT performance owing to the large and long lateral grown domains with rather good crystal orientation especially the high occupancy of {100} plane in the surface normal direction. When taking the consideration of the direction of carrier flow with respect to the lateral-formed GB, extra step need to be considered to minimize the GB effect. Miniaturization of the device is one way to reduce the GB effect as seen from the experiment where TFT with 90 µm wide degraded 38.6% when the direction of carrier movement changed from parallel to perpendicular. The percentage of the mobility difference reduced to 22.6% with narrow channel width of 5 µm.

A more comprehensive way to reduce the geometrical effect on the carrier mobility is by eliminating the GB itself. An effective way in achieving such goal was introduced in Chapter 3 by a simple adjustment of laser beam shape. The justification of the high expectation GB-free crystallized by such method was proven to be effective in minimizing the effect geometrical effect of the carrier movement. The similar TFTs with 5 µm channel width operating on such film show a significant reduction on the effect of carrier movement direction with negligible 5.33% mobility decrease when operating in perpendicular direction of laser scan.

These experiments prove the success of the GB-free growth and the geometrical effect of the TFT channel was sufficiently lowered. The findings and its significant improvement can help in eliminating the TFT’s non-uniformity issue which is often associated with laser grown poly-Si.

4.5 References

1. M. M. Billah, A. B. Siddik, J. Bae Kim, L. Zhao, S. Y. Choi, D. K. Yim, and J. Jang, IEEE J. Electron Devices Soc. **7**, 503 (2019).

2. V. Rana, Dr. Thesis, Delft Univ. Technol. (2006).

3. T. T. Nguyen and S. I. Kuroki, Jpn. J. Appl. Phys. **58**, SBBJ08 (2019).

4. N. Sasaki, M. Arif, and Y. Uraoka, SID Symp. Dig. Tech. Pap. **49**, 755 (2018).

5. T. T. Nguyen, M. Hiraiwa, and S. I. Kuroki, Appl. Phys. Express **10**, 056501 (2017).

6. B. Y. Tsaur, J. C. C. Fan, M. W. Geis, D. J. Silversmith, and R. W. Mountain, IEEE Electron Device Lett. **3**, 79 (1982).

7. H. I. Kim, J. M. Sung, H. U. Cho, Y. J. Kim, Y. G. Park, and W. Y. Choi, Electron. **10**, 29 (2021).

8. A. Hara, M. Takei, F. Takeuchi, K. Suga, K. Yoshino, M. Chida, T. Kakehi, Y. Ebiko, Y. Sano, and N. Sasaki, Japanese J. Appl. Physics, Part 1 Regul. Pap. Short Notes Rev. Pap. **43**, 1269 (2004).

9. M. Yamano, S. I. Kuroki, T. Sato, and K. Kotani, Jpn. J. Appl. Phys. **53**, 03CC02 (2014).

CHAPTER 5:

Conclusions and Future Plans

5.1 Conclusions

The main purpose of this thesis is to use CW laser with small footprint and simple set up to crystallize a-Si precursor film with elongated grain taking the advantage of the constant heating of the sample by CW laser. The crystallized film is expected to offer a better TFT performance fabricated on the film by excluding the GB scattering effect as the GB formation by CLC can be minimized. Furthermore, performance of the TFTs is focused in this thesis considering the effect of geometrical direction of carrier movement in the channel with respect to the GB direction. All in all, the final goal is to eliminate the TFT non-uniformity issue.

In Chapter 2, a preliminary study on the laser crystallization was done; first by considering the effect of C/L and it was confirmed that the incorporation of appropriate C/L thickness can help in modulating the laser power threshold for crystallization besides helps in enhancing the lateral growth by promoting heat storing in the system. Other preliminary study on laser crystallization was the confirmation of the induced thermal stress in the crystallized poly-Si film as a result of the difference in thermal expansion coefficient between silicon film and the underlying quartz substrate. Additionally, the evolution of poly-Si growth was analyzed

starting from nc-Si at low laser power to lateral growth in the optimum condition to the observation of surface amorphization at high laser power. Finally, the formation of lateral GBs in the crystallized film also studied as a result of solid/liquid interface frontal shape change.

In Chapter 3, laser beam modification was proposed to by transforming the sensitive Gaussian line beam into a flat-top rectangular beam with Gaussian profile in short axis. The transformation was made possible by simple adjustment of optical components in the laser system. The approach is effective in promoting a stable elongated growth of silicon domains without the inclusion of GBs. The formation of well textured horizontal lines on the surface upon CLC suggests that a solid/liquid frontal instability governs the solidification process. HRTEM observation reveals that the growth direction of such horizontal columnar structures is highly oriented to the {100} plane. Formation of a cluster of parallel columnar structures represent a single domain thus an interception points of the two columnar clusters represent the formation of grain boundary. Such interpretations enabled an instant judgement of the grown film thus ease the optimization process during CLC which led to the formation of a highly {100}-oriented 12 mm long quasi-single crystal.

In Chapter 4, the quality of the GB-free silicon film crystallized by rectangular beam was justified by analyzing the TFT performance on such film. TFTs were also fabricated on silicon film crystallized by Gaussian line beam to compare the TFT performances. The dependency of carrier mobility on TFT channel geometry was successfully minimized by utilizing the rectangular beam where only 5.33% difference was observed for the carrier moving in the direction of laser scan and in the perpendicular direction. This low variation confirms the claim that the crystallized film by such rectangular beam does hinder the formation of GB. The TFTs fabricated on typical CLC poly-Si show a 22.6% reduction in term of carrier mobility as resulted by carrier scattering at the high-density GBs. The preliminary

studies are the most crucial part in order to see how the growth of the silicon took part and also how the deviation from the optimum condition stuttered the preferred growth.

5.2 Challenges and future plans

The growth of the highly {100}-oriented, GB-free, stable long growth of silicon domain extending to more than 12 mm are expected to follow the mechanism of the solidification instability which was proposed by Mullins and Sekerka around 60 years back [1]. This is due to the observed periodic structure on the surface of the film which expected to be resulted by the sinusoidal solid/liquid frontal during solidification process as a criterion of solidification which involves a layer of constitutionally supercooled liquid. However, no reports have been published to refer such growth mechanism by laser crystallization. Thus, a theoretical approach is required to confirm the claim using the well-established mathematical equations used by Mullins-Sekerka as well as other scholars in the era [2,3].

Additionally, the use of rectangular beam for the crystallization on glass substrates are still not optimized; this is mainly due to lower thermal durability of glass compared to the quartz substrate used in this experiment. Higher thermal budget is imposed on the sample by using this rectangular beam as opposed to the regular line beam which was successfully used to crystallized a-Si on polyimide (PI) substrate. The crystallization on PI made possible by incorporating additional layer of sacrificial a-Si layer to act as a heat sink to prevent thermal damage on the PI structure. This approach has been published elsewhere [4].

Apart from that, the analysis on TFT properties fabricated on the so-called GB-free film need to be intensively characterized as the grown film might be the best candidate to remove performance disparity on TFTs thus eliminate the performance uniformity issue. This simple process which yielded high quality results needs more attention to be regarded as a standard process in the mass production line.

5.3 References

1. W. W. Mullins and R. F. Sekerka, J. Appl. Phys. **35**, 444 (1964).

2. R. Trivedi and W. Kurz, Acta Metall. **34**, 1663 (1986).

3. P. K. Galenko and D. A. Danilov, Phys. Rev. E - Stat. Physics, Plasmas, Fluids, Relat. Interdiscip. Top. **69**, 14 (2004).

4. N. Sasaki, M. Arif, Y. Uraoka, J. Gotoh, and S. Sugimoto, J. Electron. Mater. (2021).

Acknowledgements

First and foremost, I would like to express my deepest gratitude to Prof. Yukiharu Uraoka for giving me the chance to further my study and do research in Nara Institute of Science and Technology (NAIST) as well as write this thesis under his supervision throughout my doctoral program. I would like to thank Prof. Jun Ohta and Prof. Hisao Yanagi for the supervision, fruitful discussions and meaningful suggestions for me to keep on filling the void in my research. I would like to express my appreciation to Assoc. Prof. Mutsunori Uenuma for his guidance and help throughout the years to make my research run as smooth as it would. I owe my deepest gratitude to Dr. Nobuo Sasaki for his help and guidance as well as lots of insightful ideas from lots of discussions to ensure progress in this research. I also would like to thank him for solving any difficulties in performing this research for years long. I am particularly grateful for the assistance given by him to make my first journal publication a smooth process. I would like to thank again all my academic supervisors Prof. Yukiharu Uraoka, Prof. Jun Ohta, Prof. Hisao Yanagi, Assoc. Prof. Mutsunori Uenuma and Dr. Nobuo Sasaki for reviewing my thesis and helping me to improve this thesis and finally to complete my doctoral program.

I would like to offer my special thanks to Assistant Prof. Juan Paolo Soria Bermundo for his ideas and critical questions to help me find best ways to solve the problems related to my research. I also want to express my deepest appreciation to Assistant Prof. Michael Paul Jallorina for his supports and positive vibes to help me keep my head up whenever difficulties came. I would like to offer my special thanks to Materials Science’s technical staffs who taught and help me in handling equipments for my research to proceed; specially to Mr. Noritaka Koike, Mr. Kazuhiro Miyake, Mr. Yasuo Okajima, Mr. Shohei Katao, Mr. Fumio Asanoma, Mr. Shunsuke Kawabata and Ms. Sakiko Fujita.

I am deeply grateful to Mrs. Yukiko Morita for her wonderful support and kindness to me; be it related to my research or even my life in NAIST. I also want to use this opportunity to thank Information Device Science laboratory staff, Mrs. Ryoko Miyanaga and Mrs. Sachiyo Aoyagi who are willing to help and advise me anytime whenever I need their support; as well as other members who unconditionally helped and supported me a lot, days and nights; especially TFT group members Dianne Corsino, Aimi Syairah, Diki Purnawati, Tsutsui Tomohito, Umu Hanifah, Pongsakorn Sihapitak and Mr. Satoshi Takayama. Not to forget all my friends and acquaintances who might not physically be here but their moral and mental supports are always will be appreciated.

Last but not least, I would like to express my appreciation to the closest people to me whom I am deeply grateful to; my lovely wife Nurul Athirah and my son Muhammad Athif for always being with me physically or mentally, to show their love, giving me endless support and expressing joys to keep my days bright. Above all, I would like to express my deepest appreciation to my dad, Mr. Razali Yaacob and my late mom, Mrs. Wan Mariah Ahmad for their unconditional love and endless support to see me succeed.

~Alhamdulillah~

Muhammad Arif Bin Razali
2021/07/09

List of Publications

A. Papers (First author)

1. "Extension of the {100}-Oriented Grain-Boundary Free Si Thin Film Grown by a Continuous-Wave Laser Lateral Crystallization",
   Muhammad Arif, Nobuo Sasaki, Yasuaki Ishikawa and Yukiharu Uraoka,
   Thin Solid Films, **708**, 138127 (2020).

B. Papers (Co-author)

1. "Transition Mechanism of the Thin Si-Films Obtained by the CW Laser Lateral Crystallization from the Grain-Boundary Free Highly {100} Oriented Crystal to the Twinned {211} Crystal Depending on the Laser Power",
   Nobuo Sasaki, Muhammad Arif and Yukiharu Uraoka,
   Japanese Journal of Applied Physics, **58,** SBBJ02 (2019).

2. "Effect of Surface Tension on Crystal Growth of Si Thin Films by a Continuous-Wave Laser Lateral Crystallization",
   Nobuo Sasaki, Muhammad Arif and Yukiharu Uraoka,
   Applied Physics Express, **12**, 3-8 (2019).

3. "Unseeded Crystal Growth of (100)-Oriented Grain-Boundary-Free Si Thin-Film by a Single Scan of the CW-Laser Lateral Crystallization of a-Si on Insulator",
   Nobuo Sasaki, Muhammad Arif, Yukiharu Uraoka, Jun Gotoh and Shigeto Sugimoto,
   Crystals, **10**, 405 (2020).

4. "Continuous-Wave Laser Lateral Crystallization of a-Si Thin Films on Polyimide Using a Heatsink Layer Embedded in the Buffer SiO_2",
Nobuo Sasaki, Muhammad Arif, Yukiharu Uraoka, Jun Gotoh and Shigeto Sugimoto,
Journal of Electronic Materials, **50**, 2974 (2021).

C. International Conference (First author)

1. "Extension of a 10 mm long {100}-Oriented Grain Boundary Free Silicon Domain Crystallized by Continuous Wave Green Laser",
Muhammad Arif, Nobuo Sasaki, Satoshi Takayama, and Yukiharu Uraoka,
21st iMiD 2021, 05_2064, P5-42, Seoul, Korea (Hybrid), August 2021.

D. International Conference (Co-author)

1. "Folded-Pixel-Circuit Design in Grain-Boundary-Free (100) Oriented LTPS Stripes Fabricated by Selective CW-Laser Lateral Crystallization",
Nobuo Sasaki, Muhammad Arif and Yukiharu Uroaka,
SID 2018 Display Week International Symposium, 57-3, California, USA, May 2018.

2. "Effect of Laser Power on the Surface Texture Transition of the Thin Si-Films from Grain-Boundary Free (100) to Twinned (211) in CW Laser Lateral Crystallization",
Nobuo Sasaki, Muhammad Arif and Yukiharu Uraoka,
SSDM International Meeting 2018, N-2-02, Tokyo, Japan, September 2018.

3. "Characterization of the Grain-Boundary Free (100) Si Thin-Films Obtained by CW-Laser-Lateral Crystallization at Room Temperature in Air",

Nobuo Sasaki, Muhammad Arif and Yukiharu Uraoka,

EDTM Conference, Singapore, March 2019.

4. “Isotropic TFT Mobility in the (100)-Oriented Grain-Boundary-Free Huge Si Thin Film Grown by the Continuous-Wave-Laser Lateral Crystallization”,

   Nobuo Sasaki, Muhammad Arif, Satoshi Takayama, Jun Gotoh, Shigeto Sugimoto and Yukiharu Uraoka,

   SSDM International Meeting 2021, J-4-04, Virtual Conference, September 2021.

E. Domestic Conference (First author)

1. “Effect of Overlapped Scan on CLC (100) Crystal Growth”,

   Muhammad Arif Razali, Nobuo Sasaki and Yukiharu Uraoka,

   JSAP Spring Meeting 2018, 17a-C101-8, Waseda, March 2018.

2. “Change of Raman Scattering as a Function of Laser Power in Si-Films Crystallized by CLC”,

   Muhammad Arif Razali, Nobuo Sasaki, Yasuaki Ishikawa and Yukiharu Uraoka,

   JSAP Autumn Meeting 2018, 20a-233-3, Nagoya, September 2018.

F. Domestic Conference (Co-author)

1. “界面エネルギーの(100)配向 CLC 結晶成長への影響”,

   佐々木 伸夫 , Muhammad Arif , 浦岡 行治,

   JSAP Spring Meeting 2017, 14a-304-1, Yokohama, March 2017.

2. “ (100) 配向 CLC 結晶成長への双晶発生の影響”,

佐々木 伸夫 , Muhammad Arif , 浦岡 行治,

JSAP Spring Meeting 2018, 17a-C101-7, Waseda, March 2018.

3. "CW レーザーSi 薄膜結晶成長における（100）配向性のパ ワー依存性",

   佐々木 伸夫 , Muhammad Arif , 浦岡 行治,

   JSAP Autumn Meeting 2018, 20a-233-6, Nagoya, September 2018.

4. "高移動度薄膜トランジスタ作製に向けた CW レーザーア ニール法による非晶質基板上 Si 薄膜の(100)面配向結晶 化",

   高山 智之 , 佐々木 伸夫 , Muhamad Arif , 浦岡 行治,

   JSAP Autumn Meeting 2021, 10p-N302-1, Nagoya, September 2021.

5. "(100)配向 Grain-Boundary-Free Si 薄膜のレーザ結晶化機 構",

   佐々木 伸夫 , Muhammad Arif , 高山 智之 , 浦岡 行治,

   JSAP Autumn Meeting 2021, 10p-N302-2, Nagoya, September 2021.